3D LIDAR AIDED GNSS-RTK POSITIONING WITH NLOS CORRECTION AND CONSISTENT FUSION FOR AUTONOMOUS SYSTEMS IN URBAN CANYONS

XIKUN LIU

PhD

The Hong Kong Polytechnic University

2026

The Hong Kong Polytechnic University
Department of Aeronautical and Aviation Engineering

3D LiDAR aided GNSS-RTK positioning with NLOS correction and consistent fusion for autonomous systems in urban canyons

Xikun Liu

A thesis submitted in partial fulfilment of the requirements
for the degree of Doctor of Philosophy

July 2025

Certificate of Originality

I hereby declare that this thesis is my own work and that, to the best of my knowledge and belief, it reproduces no material previously published or written, nor material that has been accepted for the award of any other degree or diploma, except where due acknowledgement has been made in the text.

_____(Signature)

___Xikun Liu___(Name of student)

Abstract

Global Navigation Satellite System (GNSS) is widely used in intelligent navigation systems. GNSS real-time kinematic (RTK) has shown centimeter-level absolute positioning results in open-sky areas. However, in areas with complex urban canyons such as Hong Kong, the accuracy of GNSS is severely diminished due to signal blockage and reflection. Polluted GNSS measurements as well as poor satellite geometry are two main reasons for deteriorating urban GNSS-RTK positioning performance. Such a problem significantly affects the application of intelligent navigation systems in urban environments.

To address this problem, the complementary roles of the Light Detection and Ranging (LiDAR) sensor and GNSS are explored in existing works. LiDAR, as an active ranging sensor, not only enables precise relative positioning but also allows digital modeling of the surrounding environment. Recently proposed 3D LiDAR-aided (3DLA) GNSS methods employ the point cloud map to identify the non-line-of-sight (NLOS) reception of GNSS signals for further exclusion and remodeling. This facilitates the GNSS receiver to obtain improved urban positioning. However, due to the remained multipath receptions and poor geometry, the positioning error can still reach several meters. On the other side, GNSS and LiDAR odometry are well combined as they provide absolute and relative positioning, respectively. Their integration in a loosely-coupled manner is straightforward but is still challenged due to the GNSS signal pollution and poor geometry. Therefore, utilizing tightly-coupled

GNSS/LiDAR integration for improving GNSS geometry needs to be studied.

In this thesis, we explored the 3D LiDAR aided GNSS-RTK positioning method in terms of 3D LiDAR aided GNSS outlier mitigation and tightly-coupled GNSS/LiDAR integration for geometry improvement. We first focused on further improving the reliability of 3D LiDAR-aided NLOS mitigation and improving the efficiency of tightly-coupled LiDAR/GNSS integration. Further, we proposed GLIO, a GNSS/LiDAR/IMU integrated estimator that tightly fuses all raw measurements using two stages of factor graph optimization (FGO) to achieve globally consistent and continuous pose estimation. Specifically, we designed an iterated coarse-to-fine batch integration between GNSS and LiDAR for global NLOS exclusion. Moreover, we proposed an accurate NLOS correction method by Doppler-aided direction-of-arrival (DOA) estimation and 3D LiDAR-aided reflection restoration. Different from the conventional model, or LiDAR-based NLOS correction methods, the proposed method does not rely on the shortest path assumption and therefore is able to correct NLOS receptions with errors exceeding 100 meters.

The effectiveness of the proposed methods in this thesis are extensively evaluated and verified through the challenging dataset involving highly urbanized areas. The proposed system achieves great improvement in positioning accuracy compared with the traditional GNSS positioning method and representative integration with the LiDAR/IMU system. The results also show that the proposed system can achieve real-time positioning capability with higher robustness in a highly urbanized area using commercial-level GNSS receivers and LiDAR/IMU sensor kit.

Acknowledgements

First and foremost, I would like to express my heartfelt gratitude to my supervisor, Dr. Weisong Wen, for his exceptional mentorship, intellectual guidance, and unwavering support throughout my PhD journey. Many of the key ideas in this dissertation were born out of our deep and insightful discussions. Dr. Wen not only shaped the direction of my research with his clarity and vision but also cared about my well-being and personal growth along the way. His encouragement, patience, and trust have been instrumental in helping me persevere through the challenges of doctoral life. I am equally grateful to my co-supervisor, Dr. Li-Ta Hsu, whose wisdom and generosity left a lasting impact on me—not only as a researcher, but also as a person. Beyond technical advice and academic feedback, Dr. Hsu has shared with me invaluable life lessons that I will carry forward in my future endeavors.

I would like to extend my sincere appreciation to my thesis examiners, Prof. Hui Kong from the University of Macau and Prof. Honglei Qin from Beihang University, for their time, thoughtful reviews, and insightful suggestions that helped improve the quality of this dissertation.

Special thanks go to all my colleagues at the TASLAB and IPNL. Thank you for the inspiring discussions, collaborative experiments, and joyful moments we shared—whether in the lab, on data collection trips, or during group outings. Your support and companionship made my doctoral journey truly meaningful and unforgettable.

Last but not least, I am deeply thankful to my family for their unconditional love and encouragement throughout this journey.

List of Publications

Journal

[1] X. Liu, W. Wen, and L.-T. Hsu, "GLIO: Tightly-coupled GNSS/LiDAR/IMU integration for continuous and drift-free state estimation of intelligent vehicles in urban areas," *IEEE Transactions on Intelligent Vehicles*, vol. 9, no. 1, pp. 1412–1422, 2023 (Project)

[2] X. Liu, W. Wen, L. Zhang, and LT. Hsu, 3D LiDAR Aided GNSS NLOS Correction by Direction-of-Arrival Estimation Using Doppler Measurements in Urban Canyons, *IEEE Transactions on Intelligent Transportation Systems*

[3] X. Liu, W. Wen, F. Huang, H. Gao, Y. Wang, and LT. Hsu, 3D LiDAR aided GNSS NLOS mitigation for reliable GNSS-RTK positioning in urban canyons, *IEEE Transactions on Instrumentation and Measurement*

[4] J. Zhang, X. Liu, W. Wen, and L.-T. Hsu, "Safety-Quantifiable Planar-Feature-based LiDAR Localization with a Prior Map for Intelligent Vehicles in Urban Scenarios," *IEEE Transactions on Intelligent Vehicles*, 2024

Conference

[1] X. Liu, W. Wen, and L.-T. Hsu, "3d LiDAR aided GNSS real-time kinematic positioning via coarse-to-fine batch optimization for high accuracy mapping in dense urban canyons," in *Proceedings of the 35th International Technical Meeting of the Satellite Division of The Institute of Navigation (ION GNSS+ 2022)*, 2022, pp. 1954–1965

[2] Liu, Xikun and Wen, Weisong and Hsu, Li-Ta, "3d LiDAR Aided GNSS NLOS Correction with Direction of Arrival Estimation Using Doppler Measurements," in *Proceedings of the 36th International Technical Meeting of the Satellite Division of The Institute of Navigation (ION GNSS+ 2023)*, 2023, pp. 2206–2216

Table of Contents

List of Figures

List of Tables

Chapter 1

Introduction

1.1 Background

Remarkable progress has been achieved in the development and deployment of unmanned autonomous systems, including unmanned aerial vehicles (UAVs) [5], autonomous ground vehicles, and mobile robots [6]. Specifically, in urban areas, these systems are being applied in a wide range of domains such as transportation, logistics, infrastructure inspection, and emergency response [7]. To operate autonomously in dynamic and complex environments, accurate and robust localization is foundational [8; 9]. Onboard sensor-based approaches, such as visual-inertial odometry [10] and Light Detection and Ranging (LiDAR) simultaneous localization and mapping (SLAM) [11], enable relative positioning by continuously estimating motion with respect to the surrounding environment. These methods are effective in structured or feature-rich scenes but often suffer from cumulative drift and fail under poor visibility or significant occlusion [12]. In contrast, absolute positioning techniques leverage external signals, such as radio beacons [13] or satellite-based navigation [14], to determine location within a global reference frame. Among them, Global Navigation Satellite System (GNSS) stands out as the only globally accessible, standardized, and infrastructure-independent solution for providing accurate and absolute position estimates.

With the help of the corrections from reference stations in open-sky areas, the GNSS real-time kinematic (RTK) [15] provides centimeter-level positioning accuracy. To achieve this, we firstly estimate the float solution based on double-differenced (DD) [16] GNSS raw measurements (pseudorange and carrier phase) and then perform the integer least-squares algorithm (e.g LAMBDA and its variants [17; 18]) based on the estimated float solution to resolve the integer ambiguity. However, the positioning accuracy can be significantly degraded in the urban canyon due to signal blockage and reflection by the surrounding environment. There are two main factors leading to the impact. First (challenge 1), a considerable part of received GNSS raw measurements in highly urbanized areas is so-called non-line-of-sight (NLOS) [19], where the reflected satellite signal is received as the satellite is blocked by buildings [20] or dynamic objects (e.g., double-decker buses) [21]. Such polluted measurements can significantly degrade the accuracy of the float solution. Second (challenge 2), the buildings and dynamic objects in the urban canyon block a huge number of signals from satellites, resulting in a limited number of received satellites. In other words, only satellites with high elevation angles are received. Such a case is called the poor geometry distribution [22], which limits the success rate of integer ambiguity resolution (AR) and positioning accuracy as well.

With more onboard sensors being available on autonomous systems, the integration of multiple sensors has been extensively explored over the past several decades. In recent years, research on inertial measurement systems (INS), visual sensors, and LiDAR sensor as well as their integration for positioning systems has demonstrated impressive local positioning and environmental perception capabilities. It is a promising way to integrate the onboard sensors with GNSS to mitigate the above two challenges and ultimately improve positioning accuracy in challenging areas, especially in urban canyons. Specifically, LiDAR sensors offer accurate and wide-range environmental perception capabilities that are not significantly affected by ambient lighting

(a) (b)

Figure 1.1: Illustration of GNSS NLOS reception and multi-path reception in urban canyons. (a) For NLOS reception, only one reflected signal is received. (b) For multi-path reception, it is a superposition of multiple signal components.

conditions, unlike cameras. More importantly, LiDAR provides precise relative localization constraints and enables high-precision reconstruction of the surrounding environment. These properties make LiDAR an ideal complement to GNSS, particularly in dense urban areas where satellite signals are often degraded or blocked. Therefore, the integration of LiDAR and GNSS is a natural and effective strategy to enhance positioning robustness and accuracy in complex real-world scenarios.

1.2 Problem Statements and Research Objectives

The objective of this research is to utilize 3D LiDAR perceived environmental information to perform 3D LiDAR aided (3DLA) GNSS-RTK positioning in urban canyons by tackling the above listed two major challenges. Existing 3DLA GNSS-RTK methods have shown promising results by NLOS mitigation and integrated positioning using filter or optimization. However, the performance is constantly limited by several unsolved problems. We summarize the existing problems and list key

objectives of this research below.

1.2.1 Improving Reliability of 3DLA NLOS Detection and Efficiency of GNSS/LiDAR Tight Integration

Over the past few years, a series of methods for 3DLA GNSS methods have been continuously proposed, whereby 3D LiDAR is utilized to reconstruct the environment based on a point cloud map (PCM) to mitigate the GNSS NLOS receptions [23; 24; 21; 20; 25]. However, these methods detect NLOS receptions based on either a single frame point cloud, which is limited by the narrow field of view (FOV) of LiDAR, or accumulated multiple frames point cloud by LiDAR/inertial odometry (LIO) methods, which are subject to drift over time. How to reliably and complementarily integrate GNSS and LiDAR for GNSS NLOS mitigation remains to be explored.

In terms of improving GNSS geometry distribution, tightly integrating GNSS with LiDAR has a great potential for enhancing the state observability in the presence of poor satellite geometries and maintaining estimation accuracy during short-term GNSS outages or GNSS pollution. However, current works on tightly-coupled GNSS/LiDAR/INS integration mostly tend to use huge amounts of LiDAR observations, which requires significant time consumption for data processing and optimization, especially for the current mainstream scan-to-map sliding-window-based factor graph optimization (FGO) methods. Given the significant redundancy of LiDAR observations, it is necessary to analyze the contribution of LiDAR observations to the state observability in real scenarios. Therefore, we can figure out how can the integration system use fewer LiDAR observations to ensure the state observability at the same level. This can effectively reduce the complexity of the system and finally achieve improvement on processing efficiency while maintaining accuracy.

With a focus on the above problems, this research extends the existing 3DLA

GNSS-RTK positioning method by: (1) performing NLOS detection and exclusion based on the drift-free 3D point cloud map (PCM) to eliminate the impact of unhealthy GNSS measurements, (2) improving the satellite geometry distribution with great efficiency through the selected low-lying virtual satellites provided by LiDAR landmarks. The work is presented in:

- X. Liu, W. Wen, F. Huang, H. Gao, Y. Wang, and L. -T. Hsu, "3D LiDAR aided GNSS NLOS mitigation for Reliable GNSS-RTK Positioning in Urban Canyons." in *IEEE Transactions on Instrumentation and Measurement*

1.2.2 Optimization Consistency between LiDAR and GNSS for Tight Integration

Tightly coupled GNSS/LiDAR integration [26; 1; 27] offers two major advantages: First, tightly coupled integration allows for independent detection and mitigation of GNSS outlier observations. Second, Tightly coupled integration means that any number of GNSS observations can contribute to localization, even if fewer than 4. In terms of LiDAR constraints, the mainstream approach in LiDAR SLAM incorporates observational constraints through a scan-to-map matching strategy [28; 29; 30], which has been widely recognized as an effective method for mitigating trajectory drift. An alternative approach is scan-to-scan matching. However, it tends to accumulate drift rapidly and is therefore less commonly adopted. Following this principle, most tightly coupled GNSS/LiDAR integration systems incorporate scan-to-map LiDAR constraints together with GNSS constraints [26; 31; 32; 33]. However, this approach has inherent limitations. Since the map used for matching is fixed within the coordinate frame, scan-to-map LiDAR constraints essentially provide absolute constraints. When the map remains accurate, LiDAR observations effectively constrain the system state. However, after long term operation, inevitable map drift occurs, especially in complex environments. In such cases, scan-to-map LiDAR ob-

servations incorrectly constrain the state and may introduce inconsistencies with GNSS observations. This issue also raises a long-standing, unresolved challenge: how to balance the weighting of GNSS and LiDAR observations. When map drift occurs, the quality of LiDAR observations cannot be properly evaluated, making it difficult to develop an effective weighting strategy.

To tackle this problem, this research presents a novel GNSS/LiDAR/IMU tightly-coupled odometry that: (1) tightly fuses the GNSS, LiDAR, and IMU all at raw measurement level through FGO, and (2) employs two stages of optimization including sliding-window-based optimization and batch-based fusion to achieve efficient, consistent and robust positioning solutions. Within the proposed two stages of optimization, different LiDAR factors such as the scan-to-map scheme in the first stage and the scan-to-multiscan scheme in the second stage are employed. Moreover, the consistent optimization provides great robustness against the GNSS observation error, enabling reliable outlier detection and mitigation. The work is published in:

- X. Liu, W. Wen, L. -T. Hsu, "3D LiDAR aided GNSS real-time kinematic positioning via coarse-to-fine batch optimization for high accuracy mapping in dense urban canyons," in *Proceedings of the 35th International Technical Meeting of the Satellite Division of The Institute of Navigation (ION GNSS+ 2022)*, 2022.

- X. Liu, W. Wen, L. -T. Hsu, "GLIO: Tightly-coupled GNSS/LiDAR/IMU integration for continuous and drift-free state estimation of intelligent vehicles in urban areas," in *IEEE Transactions on Intelligent Vehicles*, vol. 9, no. 1, pp. 1412–1422, 2023.

1.2.3 Enhancing 3D LiDAR aided NLOS Correction with GNSS Doppler Observations

Recent research revealed that the direct GNSS NLOS exclusion would lead to severe geometry degradation which cannot guarantee positioning accuracy. Correcting or remodeling the NLOS measurements rather than excluding them is critical due to the potential poor satellite geometry. The conventional 3D model-aided (3DMA) GNSS positioning method utilizes ray-tracing technology to predict signal transmission paths in a prior 3D city model. The recently proposed 3D LiDAR-aided (3DLA) GNSS restores the reflection paths by traversing 360-degree azimuth with fixed elevation in a real-time reconstructed point cloud map (PCM)[22]. Nevertheless, existing 3DMA and 3DLA GNSS NLOS correction methods predominantly rely on the shortest path assumption to identify the reflection path. This approach is premised on the rationale that the signal traveling the shortest distance typically experiences the least attenuation and, therefore, exhibits the highest signal power. However, the validity of this assumption is frequently compromised in dense urban environments. Modern architectural features, particularly glass curtain walls, create highly reflective surfaces that facilitate efficient specular reflections. Consequently, signals propagating along longer paths may unexpectedly retain higher energy and dominate the signal reception, leading to erroneous path identification. Beyond ranging observables such as pseudorange and carrier phase, there are Doppler measurements, which can be used for reliable velocity estimation [34; 35]. The Doppler effect reflects frequency shifts due to relative motion between the receiver and the signal source. For the LOS case, the measured Doppler frequency directly corresponds to the relative motion between the satellite and the receiver. However, for the NLOS case, the satellite-emitted signal first reaches the reflection point before being received. In such cases, the Doppler frequency reflects the relative motion between the reflection

point and the receiver [25]. This relationship reveals that the Doppler measurement in NLOS reception inherently encodes the Direction-of-Arrival (DOA) of the reflected signal from the reflection point to the receiver. By incorporating Doppler-inferred DOA into existing 3DLA GNSS NLOS correction methods, it is possible to actively identify true reflection paths, eliminating the need for the shortest path assumption.

This research proposed a reliable NLOS DOA estimation and correction method based on Doppler measurements. In detail, we first propose an optimization-based DOA estimation method. Secondly, we propose the DOA-PCM-based NLOS correction method, which includes reflection point searching, correction formulation, and validation. Different from the conventional methods, the proposed method does not rely on the shortest path assumption and therefore is able to correct NLOS receptions with enormous errors. The work is published in:

- X. Liu, W. Wen, and L. -T. Hsu, "3D LiDAR Aided GNSS NLOS Correction with Direction of Arrival Estimation Using Doppler Measurements," in *Proceedings of the 36th International Technical Meeting of the Satellite Division of The Institute of Navigation (ION GNSS+ 2023)*, 2023.

- X. Liu, W. Wen, L. Zhang, and L. -T. Hsu, "3D LiDAR Aided GNSS NLOS Correction by Direction-of-Arrival Estimation Using Doppler Measurements in Urban Canyons", in *IEEE Transactions on Intelligent Transportation Systems*

1.3 Thesis Outline

The outline of this thesis is as follows:

Chapter 2 provides an overview of recent advancements in GNSS positioning enhancement for urban environments, focusing on two primary research directions: GNSS outlier mitigation and multi-sensor fusion. The first direction aims to mitigate multipath and NLOS errors through techniques such as fault detection and exclusion

(FDE), 3D model-aided GNSS, and LiDAR-based corrections. The second direction explores the integration of GNSS with other sensor modalities—including LiDAR and IMUs—through loosely and tightly coupled architectures. Optimization-based frameworks, such as factor graph optimization, are highlighted for their ability to exploit raw measurements and temporal correlations.

Chapter 3 provides a tightly-coupled GNSS-RTK/LiDAR/INS integration system with 3D LiDAR aided NLOS mitigation for reliable positioning in urban areas, where it focuses on further improving the reliability of 3D LiDAR aided NLOS mitigation and achieving a more efficient tightly-coupled integration system. The effectiveness of the proposed method has been validated by the evaluation conducted on the open-sourced challenging dataset, UrbanNav.

Chapter 4 develops a GNSS/LiDAR/IMU integrated estimator that tightly fuses GNSS pseudorange, Doppler, LiDAR, and IMU measurements using FGO. To fully exploit the complementarity of the LiDAR and GNSS measurements, two stages of the optimization scheme are utilized to achieve globally consistent and continuous pose estimation. In the first stage of optimization, the sliding-window-based FGO is employed to integrate the GNSS-related factors, IMU pre-integration factor, and scan-to-map-based LiDAR factor for efficient odometry estimation. In the second stage of optimization, the LiDAR factor is employed as a scan-to-multiscan scheme to maintain global consistency and improve the robustness to the GNSS outlier by large-scale batch optimization. Its performance is evaluated through the challenging datasets UrbanNav.

Chapter 5 proposes a novel 3D LiDAR-aided GNSS NLOS correction method by utilizing the Doppler measurement to infer the signal reflection routes, and importantly, without relying on the shortest path assumption. The evaluation of datasets collected in urban canyons demonstrates the effectiveness of the proposed method.

Chapter 6 includes the conclusion and future work.

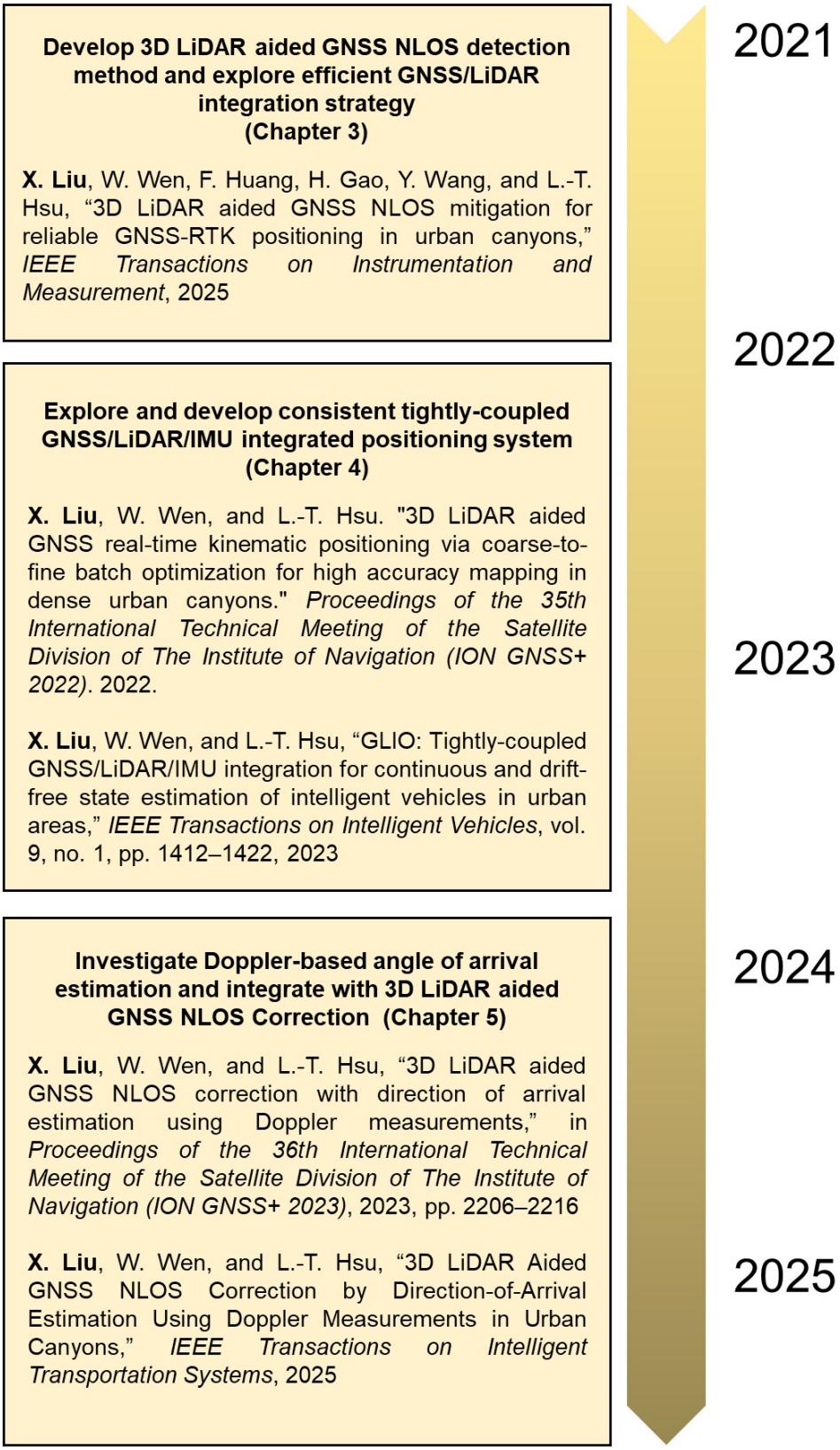

Figure 1.2: Overall flowchart and the corresponding publications of this thesis.

Chapter 2

Literature Review

Numerous studies have focused on improving GNSS positioning performance in dense urban environments, where signal blockage, multipath propagation, and NLOS effects significantly degrade localization accuracy. Existing efforts can be broadly divided into two main research directions. The first aims to process and correct GNSS signals to mitigate multipath and NLOS errors. This includes traditional FDE techniques, as well as more advanced perception-based approaches. For the latter one, 3D model-aided GNSS methods utilize detailed building models to simulate satellite visibility and reflection paths, enabling signal classification and correction. More recently, 3D LiDAR-aided techniques have emerged, leveraging real-time point cloud data to detect environmental obstructions and estimate reflection surfaces for GNSS outlier exclusion and correction, which effectively improves positioning robustness.

The second research direction focuses on integrated estimators for enhancing localization accuracy through multi-sensor fusion. These approaches integrate GNSS measurements with complementary sensor modalities such as LiDAR, cameras, and inertial measurement units (IMUs). Depending on the integration architecture, systems are typically categorized as loosely coupled—where GNSS positions are fused post-estimation—or tightly coupled—where raw observations from all sensors are jointly optimized. In terms of modeling frameworks, both filter-based methods (e.g.,

extended Kalman filters) and optimization-based approaches (e.g., factor graph optimization) have been widely adopted. These multi-sensor fusion techniques enable more robust and drift-free state estimation in urban environments, particularly when GNSS signals are intermittent or unreliable.

2.1 GNSS NLOS/Multipath Mitigation

2.1.1 Observation-based method

A foundational class of GNSS fault detection and exclusion (FDE) [36; 37] techniques is observation-based methods. These methods operate directly on pseudorange, carrier-phase, or Doppler observations, and are widely used due to their minimal reliance on external data or prior maps. The core idea is to detect inconsistencies among redundant satellite measurements or between predicted and actual observations. Classical approaches such as Receiver Autonomous Integrity Monitoring (RAIM) [38] implement statistical consistency checks to identify and exclude outlier satellites. In multi-sensor systems, innovation-based filtering evaluates measurement residuals within Kalman filters to flag abnormal deviations [39]. Their effectiveness has been significantly enhanced by the advent of multi-constellation GNSS, tighter GNSS/IMU integration, and adaptive statistical models developed for urban environments.

Redundancy-Based Consistency Checks and RAIM

One of the foundational approaches to FDE in GNSS is the use of redundant measurements to perform consistency checks. If more satellites are tracked than the minimum needed for a position fix, the extra measurements can be checked against each other. RAIM is the classical framework that implements this idea [38; 40; 41; 42]. RAIM uses statistical consistency tests on pseudorange residuals or on position solutions to detect outliers. In essence, the receiver computes its position using dif-

ferent subsets of satellites and checks if all solutions agree within expected error bounds. Any large disagreement suggests a faulty measurement. This method has long been used in aviation to detect satellite faults [43; 44; 45], and it remains a common approach to handle multipath and NLOS-induced blunders in urban positioning [46; 47; 48; 49; 50].

Traditional RAIM algorithms assumed at most one fault at a time, but in city environments multiple measurements can be compromised simultaneously [51; 52; 53]. Researchers have recognized that conventional RAIM may fail to detect errors when several satellites are affected by large multipath biases at once [37]. To address this, modern RAIM schemes incorporate multi-constellation GNSS and multi-fault hypotheses [54]. The availability of GPS, GLONASS, Galileo, BeiDou, etc. on many receivers since 2015 provides increased redundancy. Advanced RAIM (ARAIM) algorithms [55; 56; 57] leverage this to consider multiple potential fault combinations in a multiple-hypothesis solution separation approach. Beyond solution separation, other statistical enhancements to RAIM have emerged. One notable development is Bayesian RAIM [58; 59; 60; 61], which introduces a probabilistic treatment of each measurement's fault status. Instead of binary "good" or "bad" assumptions, a Bayesian approach assigns a prior probability to each satellite being faulty and updates these probabilities based on the observed data consistency. Another adaptation in consistency checking is the use of position-domain integrity measures rather than raw residual tests [52; 62; 63; 64]. Instead of checking the residual of each range, some RAIM algorithms (especially in multi-constellation ARAIM) compute protection levels or error bounds on the position solution. If the bound exceeds a threshold or if excluding a satellite significantly shrinks the bound, that satellite may be excluded.

Innovation-Based Fault Detection in Filtering

While RAIM performs snapshot consistency checks (each epoch independently), innovation-based detection refers to monitoring the residuals (innovations) of a sequential filter (typically a Kalman filter) for GNSS outliers [39; 65; 66]. When fusing GNSS measurements with other sensors in a Kalman filter [67], the innovation is the difference between the observed measurement and the predicted measurement (based on the prior state estimate). These innovations provide a real-time assessment of measurement consistency with the navigation solution. Large or systematically biased innovations indicate measurement faults or unmodeled errors. Innovation-based FDE essentially extends the RAIM concept into the time domain, using the filter's redundancy over time and sensor inputs. A common approach is to perform a chi-square test on the innovation vector at each epoch [68]. If the combined innovation norm is above a threshold, it signals that the incoming measurements do not agree with the predicted state, hence likely containing a fault [65; 69; 70]. The general finding is that coupling an extra sensor with GNSS allows one to cross-verify the two sources: the extra sensor can propagate position when GNSS is unreliable, and conversely, GNSS innovations can be checked against current estimates. If GNSS suddenly deviates from other sensors by more than the expected noise, a fault is detected and those measurements can be rejected. This consistency check between sensors significantly boosts reliability in urban settings, as evidenced by numerous studies on vehicle navigation. For instance, recent high-accuracy urban positioning experiments [71; 65; 39; 72; 73] tightly coupled single-frequency multi-GNSS RTK with a MEMS IMU and implemented an innovation-based outlier rejection strategy. Yet, just like RAIM, if most satellites are compromised (e.g., downtown skyscraper scenario), the filter might simply see a large position error but struggle to attribute it to specific measurements.

In summary, traditional FDE methods rely on statistical consistency checks, such as parity vector-based methods, innovation testing in Kalman filters, or residual analysis, to isolate inconsistent observations within the measurement set. These techniques have been shown to improve solution robustness in open-sky environments but tend to degrade in urban areas where signal distortions are more prevalent and harder to model accurately. On the other side, the high-rise buildings in urban areas bring significant signal blockage, leaving only a limited number of satellites visible in a narrow sky view. This so-called poor satellite geometry can lead to large positioning errors and high estimation uncertainty. Excluding NLOS receptions, while improving observation quality, further deteriorates the already limited satellite geometry. Therefore, NLOS correction instead of exclusion is more critical for urban GNSS positioning.

2.1.2 Enviromental Perception-based method

The harsh signal conditions of urban environments have both challenged existing FDE methods and spurred new adaptations. One fundamental issue is that multipath and NLOS errors do not behave like random noise – they can introduce systematic biases and correlations that violate the assumptions of many statistical tests. Classical RAIM and outlier tests assume measurement errors are independent and normally distributed; in urban settings, errors from satellites at similar geometries (e.g., all low-elevation satellites in the direction of a tall building) may all be biased high or low together. This means the "redundancy" in measurements is somewhat illusory, as they share error sources. To address these limitations, recent research has increasingly explored perception-aided approaches that leverage complementary sensor information—such as 3D building models, LiDAR, or camera data—to detect and mitigate NLOS effects in GNSS measurements. Unlike traditional FDE methods that rely solely on internal statistical consistency checks, these approaches

incorporate external environmental cues to identify potential error sources. By reconstructing a 3D understanding of the surrounding environment, a perception-based system can infer satellite visibility, detect obstructions, and even predict the potential reflection pattern of GNSS signal. This enables more proactive and accurate error detection and correction, especially in complex urban canyons where multipath signals are prevalent and signal visibility is highly variable.

3D Model aided GNSS NLOS Mitigation

With the development and availability of urban building model resources, researchers have developed 3D model-aided (3DMA) GNSS for NLOS detection and even correction utilizing ray-tracing technology [74; 75; 76; 77; 49; 78; 79; 80]. The 3DMA ray-tracing GNSS performs positioning through the following steps: (1) Given an initial position of the receiver, the positions of the satellites (calculated through ephemeris), and a 3D model of the surrounding buildings (which can be a pre-downloaded city map), (2) The algorithm emits simulated light rays from the satellite or reversely emits light rays from the receiver to calculate the interaction between the signal and the building. For non-direct signals, the algorithm calculates the possible propagation paths of the signal based on the law of reflection (incident angle equals to reflection angle), (3) Position calculation and correction. One method is to identify NLOS signals and directly reduce the weight of the satellite during calculation, or simply eliminate it. Alternatively, the distance difference calculated using ray tracing can be used to directly subtract the length of the reflection path from the observed pseudo-range, restoring an approximate straight-line distance. Noteably, the shortest path assumption is used to determine the actual reflection path when there are multiple reflection candidates for a single satellite. This is due to the lack of knowledge about building surface electrical properties. This approach assumes that the signal traveling along the shortest path tends to retain the highest signal

power, maximizing reception probability [77]. Using the predicted signal path, NLOS reception can be corrected by subtracting the additional transmission length from the NLOS trajectory compared to the Line-of-Sight (LOS) trajectory. However, the 3DMA GNSS NLOS correction is subject to certain limitations. First, it requires comprehensive, city-scale 3D building models, rendering it ineffective for dynamic objects or unmodeled road infrastructure. Second, its performance is limited by large initial position errors, which are common in urban environments. Third, it cannot handle NLOS receptions with long reflection distances due to the reliance on the shortest path assumption. These limitations constrain the reliability and practical applicability of 3DMA GNSS methods in urban environments.

3D LiDAR aided GNSS NLOS Mitigation

To further address the challenges of urban GNSS positioning, the 3D LiDAR-aided (3DLA) GNSS positioning methods have been proposed. Unlike the 3D building models, LiDAR offers real-time 3D point cloud observation with detailed descriptions of surrounding buildings and various dynamic objects. Moreover, the point cloud map (PCM) is reconstructed in a sensor-centric manner, eliminating the initialization challenges associated with 3DMA GNSS methods. Recent advancements have integrated single-frame LiDAR point clouds with building height lists from public data sources to detect and correct NLOS signals [81; 20]. Building surfaces are recovered through point cloud segmentation, supplemented by boundary extensions derived from building height data. NLOS signals are then modeled based on azimuth angle, elevation angle, and distance to the building surface. However, segmentation performance is significantly affected by irregular surfaces. To improve the field of view (FOV) of LiDAR and eliminate the reliance on building height lists, a combination with the sky-pointing camera for NLOS detection and correction is proposed [82]. To essentially tackle the FOV limitation and reliably determine the reflection

point for buildings with complex facades, LiDAR Simultaneous Localization And Mapping (SLAM) is introduced in 3DLA methods with PCM-based reflection point searching [22]. To be more specific, the point clouds from adjacent frames are accumulated to reconstruct a PCM. Occlusion detection is performed using the PCM, the receiver position, and the LOS vector for NLOS reception prediction. Afterward, exhaustive azimuth angle searches at a given elevation angle are performed to identify reflection point candidates. The final reflection point as well as the reflection path is determined under the shortest path assumption, similar to the above-mentioned 3DMA GNSS methods. Likewise, such an assumption oversimplifies signal behavior and limits the 3DLA NLOS correction performance.

Despite the growing adoption of 3DMA and 3DLA techniques for urban GNSS positioning, a critical limitation persists in their reliance on the shortest-path assumption when selecting among multiple potential reflection candidates. These methods typically identify the signal path with the minimal geometric distance as the most likely reflection route. However, as we discussed above, in real-world urban environments, signal propagation is not solely determined by path length, but also by the physical characteristics of the reflecting surfaces. As a result, the actual dominant reflected signal received by the GNSS antenna may not correspond to the shortest path, undermining the accuracy of NLOS detection and correction. Addressing this mismatch requires moving beyond simplistic geometric assumptions toward models that incorporate information from other observations (e.g., Doppler, signal strength, etc.) or reflection surface property. How to fundamentally resolve this issue remains an open challenge, and continued exploration is essential for achieving robust GNSS correction in dense urban.

2.2 GNSS-based Sensor Integration

In addition to GNSS NLOS correction, a substantial body of research has focused on multi-sensor fusion, where GNSS observations are integrated with additional modalities such as IMU, LiDAR, and cameras. This integration enhances positioning robustness by supplementing more observations when GNSS signal degrades. Existing fusion frameworks can be broadly characterized along two key dimensions. The first concerns the degree of coupling between GNSS and auxiliary sensors: ranging from loosely coupled architectures, where each sensor provides independent state estimates, to tightly coupled systems, in which raw GNSS observations (e.g., pseudorange, carrier phase) are directly fused with inertial or perceptual data for improved consistency and redundancy. The second dimension involves the design of the estimator itself—from filter-based approaches (e.g., Kalman filters and extended Kalman filters) to optimization-based methods, such as factor graph optimization, which provide greater flexibility in handling asynchronous measurements and performing estimation based on batch data. The following sections review key advances along both dimensions.

2.2.1 Loosely-Coupled and Tightly-Coupled Integration

Depending on the level of fused information, these studies are divided into a loosely-coupled manner based on the position-level information and a tightly-coupled manner based on the raw measurements from sensors. The loosely-coupled methods process the observations from GNSS and LiDAR/inertial systems separately and then fuse the estimated poses from the different systems according to their weights and uncertainties [28; 83; 84; 85; 86; 87; 88; 89]. However, the direct fusion of noisy GNSS positioning results may introduce errors in the system. [85] proposed a scene optimizer to assess the solutions from GNSS and the loosely-coupled fusion odometry.

The better solution is selected as the current state for further smoothing with IMU data through the Extended Kalman Filter. However, when a reliable GNSS solution is not available, the system will degrade to a loosely coupled GNSS/LIO system. Moreover, [86] performed GNSS degradation checks (e.g. Zero-Velocity update, satellites number monitor, dilution of the precision monitor) to drop unhealthy GNSS solutions to improve the overall positioning performance. Similarly, [87] proposed to apply GNSS solution selection by comparing them with the predicted position. Nevertheless, a prior map is needed [87] and the prediction is not always reliable without map information. Furthermore, simply discarding the GNSS solutions prevents the system from taking advantage of healthy GNSS observations, especially in urban environments, where there are frequently insufficient satellites number. Different from loosely-coupled methods, the tightly-coupled methods estimate the state directly based on raw measurements from all sensors, which enables separate mitigation of unhealthy GNSS measurements while maintaining healthy GNSS constraints [32; 90; 91]. The tightly-coupled system can benefit from the absolute constraints of GNSS even in highly urbanized areas with limited received satellite number. More importantly, the tightly-coupled integration scheme can effectively exploit the complementariness of GNSS and LiDAR measurements. The existing state-of-the-art methods rely on accurate outlier exclusion by performing residual check [30] or traditional statistical methods [90; 91], which requests a good initial guess and more healthy GNSS observations in a single epoch. Nevertheless, GNSS measurement error from environmental reflection can dominate the observation and is not detectable by traditional statistical methods. In other words, tightly-coupled methods outperform loosely-coupled methods in terms of both data utilization and the potential to improve positioning accuracy. Still, it remains to be explored how to further utilize the information from different sensors while improving robustness to GNSS unhealthy observations in a tightly-coupled GNSS/LiDAR/IMU framework.

2.2.2 Filter-based and Optimization-based Integration

The study of GNSS/LiDAR/IMU integration systems can also be classified in terms of fusion methods, mainly filter-based methods and optimization-based methods. As mentioned above, the work [86; 32; 90; 91] performed efficient state estimation using the Kalman filter (KF) and its variants. However, the KF-based methods mainly utilize information from the two consecutive epochs for estimation and fail to revisit or optimize the past states. On the contrary, optimization-based methods use batch data, which better exploits the temporal and special correlations. Specifically, [92; 93] sufficiently demonstrate the ability of factor graph [35] to exploit information redundancy at the raw measurement level for resisting local minimal using GNSS or GNSS/IMU measurements. Research in [83; 84; 87; 94] subsequently shows the improved performance and global consistency of optimization-based GNSS/LiDAR/IMU integration. Nevertheless, the above-mentioned methods use a loosely-coupled scheme for GNSS factors, which limits the potential of sensor fusion. Recently, [95] proposed to tightly fuse GNSS raw measurements with the LIO system through factor graph optimization. In this work, the factor graph consists of pseudorange factors to provide absolute positioning constraints, inter-epoch double-difference carrier-phase factors to provide relative positioning constraints, and relative pose constraints provided by IMU and LiDAR. However, in urban area, the carrier phase factors are hard to guarantee due to frequent cycle slip. Besides, the Doppler measurements are not utilized. Moreover, the LiDAR measurement is used in a loosely coupled manner in [95] which is based on relative pose rather than raw measurements.

In summary, the optimization-based tightly-coupled GNSS/LiDAR/IMU integration has the opportunity to make full use of the raw measurements while taking full account of the temporal and spatial correlations between the data, to obtain opti-

mal state estimates. However, the tightly-coupled full suit integration of the GNSS measurements (both the Doppler and the pseudorange measurements) and LIO using the state-of-the-art FGO is not available. Moreover, the most state-of-the-art GNSS/LiDAR/IMU integrated solutions use a scan-to-map [28] scheme for LiDAR registration. It should be noted that such LiDAR constraints scheme plays a role as an absolute constraint. In the case that the trajectory has a large drift, the LiDAR factor is natural with drift error. This approach does not provide a consistent estimate for each sensor, rather leads to inconsistency between LiDAR and GNSS measurements. The challenge of how to design a tightly-coupled GNSS/LIDAR integration system based on globally consistent optimization is still to be explored.

Chapter 3

3D LiDAR Aided GNSS NLOS Mitigation for Reliable GNSS-RTK Positioning in Urban Canyons

3.1 Introduction

In this chapter, we propose a 3DLA GNSS-RTK/LiDAR/INS integrated positioning method that achieves reliable 3DLA NLOS exclusion and efficient GNSS/LiDAR tight integration. Specifically, GNSS NLOS reception is detected and excluded through the incrementally generated and drift-free 3D sliding window PCM. Then, the sparsely selected LiDAR landmarks are used to create a so-called virtual satellite (VS) that improves the geometry distribution of the received standalone GNSS signals by tightly integrating the raw measurements from GNSS, VS, and an inertial measurement unit (IMU). After solving the above optimization problem, AR is performed based on the float solution and covariance information improved by the VS. Meanwhile, the improved float solutions and the fixed solutions are further employed to correct the drift of the 3D sliding window PCM for reliable NLOS detection. The main contributions of the proposed work are listed as follows:

(1) We propose a drift-free 3D sliding window PCM-based GNSS NLOS mitigation

method to improve the quality of the raw GNSS measurements. The drift of the 3D sliding window PCM is corrected with the help of the proposed integrated positioning system.

(2) We tightly fuse the scan-to-map LiDAR constraints and IMU constraints with GNSS observations to improve the geometry distribution in urban canyons. In particular, we focus on using fewer LiDAR observations to achieve the equivalent level of geometry distribution improvement for the integration system.

(3) Experiments have been conducted on three challenging urbanized sequences collected in Hong Kong and comprehensive comparisons are carefully conducted to show the effectiveness of the proposed method.

3.2 Method

3.2.1 System Overview

The pipeline of the proposed system is depicted in Fig. 3.1. The system consists of two major parts, namely 3D LiDAR-aided NLOS exclusion, and integrated positioning with VS-aided geometry improvement. The inputs of the system comprise raw GNSS measurements (pseudorange measurements, carrier phase measurements, and Doppler measurements), LiDAR measurements, and IMU measurements. All the measurements are processed under a common keyframe mode [10] to keep the balance between computational load and information redundancy. Firstly, the pre-integration [96] technique is used to preprocess the raw IMU measurements. Meanwhile, the initial pose of each new keyframe in the sliding window is propagated through the IMU measurements. Then the poses of the keyframes and the correspondingly generated local 3D PCM are utilized to detect the NLOS and cycle slip [97] receptions. Meanwhile, the VS constraints are created from the extracted features and PCM [11]. After preprocessing, the states in the sliding window are jointly optimized through

FGO based on the constraints from the VS, GNSS, and IMU to obtain the improved float solution, which includes the positioning result and the covariance information. Afterward, the optimized position and the covariance matrices are further applied for AR to find a fixed solution. Finally, the global pose graph optimization is performed based on the fixed and float solutions to get the final pose result. The updated global poses, as well as the corresponding PCM, will further contribute to the next iteration of GNSS NLOS detection. The marginalization strategy [10] is additionally employed to ensure real-time performance by marginalizing the measurements outside the sliding window. The detail of the methodology is introduced in the following sections.

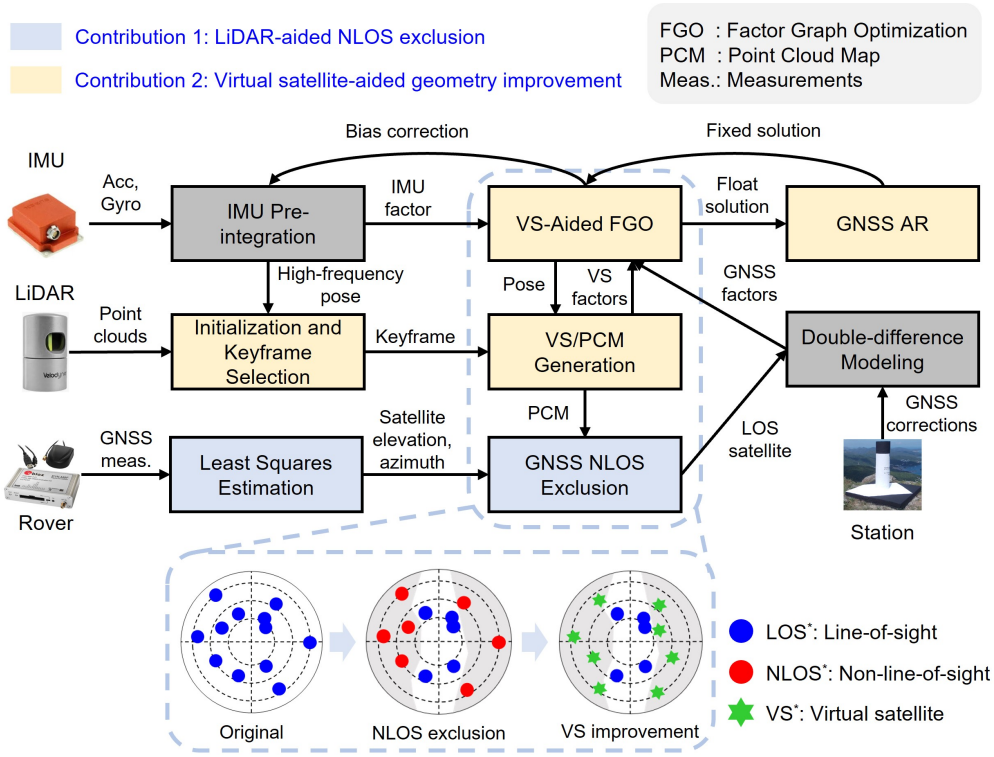

Figure 3.1: Pipeline overview of the proposed system.

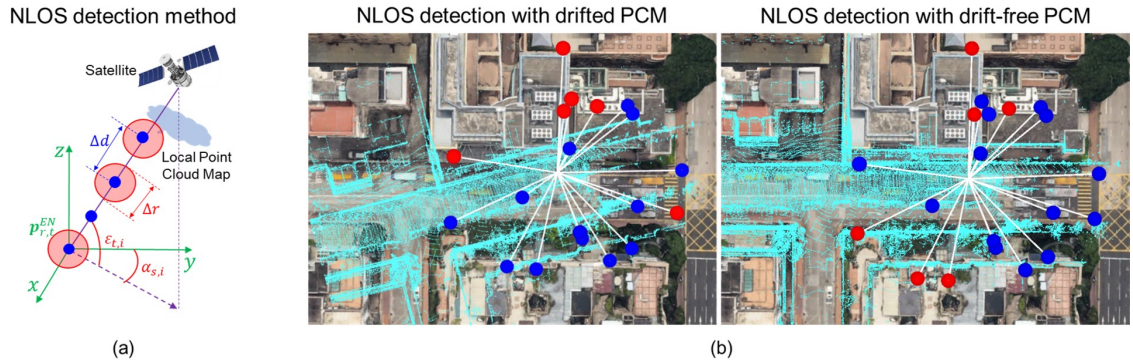

Figure 3.2: Illustration of the proposed 3D LiDAR-aided NLOS detection based on drift-free PCM. (a) shows the details of the detection method. (b) shows the comparison of satellites' occlusion in the same epoch by drifted- and drifted-free-PCM. The red dots are detected NLOS satellites, while the blue dots represent the LOS satellites. The detection result and the PCM are projected on Google Earth.

3.2.2 3D LiDAR-Aided GNSS NLOS Mitigation

For the newcoming GNSS measurements, NLOS detection and exclusion are first performed. We employ a similar fast-searching method developed in our previous work [22] to classify the satellite visibilities based on the local 3D PCM. The 3D PCM is accumulated based on the point clouds of recent keyframes. Compared with our previous method, the proposed method alleviates the attitude drift of the 3D PCM by utilizing corrections from the GNSS-RTK. Although the satellite visibility classification based on the 3D PCM is not new, we still briefly outlines the key steps for completeness. Our method contains three major steps: First, a sliding window-based local PCM, which is accumulated by the last n_{NL} keyframes, is simultaneously maintained. n_{NL} is determined for PCM distances reaching up to approximately 250m, as GNSS NLOS is primarily caused by objects within a certain distance. Second, as shown in Fig. 3.2(a), an orientation-based fixed-step search is applied on the local PCM to classify the visibility of the satellite. To be more specific, we calculate the line-of-sight (LOS) vector based on the current positions of the receiver and satellite. Then, we set the search point to the receiver's current position $\mathbf{p}_{r,t}^{EN}$ and move it in steps of Δd along the LOS vector and check the number of the

neighboring map points within the search range Δr. If the neighboring number is larger than the threshold, then the satellite will be classified as invisible, and the relevant measurement is excluded as NLOS receptions. However, when the drift is accumulated during vehicle driving, the attitude error subsequently brings great bias to the local map direction, which leads to inaccurate NLOS classification. In other words, the 3D PCM-aided NLOS detection relies heavily on accurate attitude estimation, which is easily affected by the drift. Fig. 3.2(b) illustrates how the drifted PCM will affect the detection result. Therefore, we further apply the global pose graph optimization to update the local PCM simultaneously against the potential drift error, which enables better NLOS detection by making it free from attitude bias. The global optimization is based on the improved GNSS-RTK positioning results introduced in the following sections. Fig. 3.2(b) also shows the illustration of the proposed drift-free PCM-based NLOS exclusion. It is observed that, before LiDAR-aided NLOS exclusion, nearly one-third of the satellites blocked by buildings and trees were originally used as LOS satellites, which causes large positioning errors. On the other hand, the drift-free PCM provides the correct environmental information, which leads to accurate NLOS detection.

3.2.3 VS-aided GNSS-RTK/IMU Factor Graph Optimization and Ambiguity Resolution

In this section, the method of tightly-coupled VS-aided GNSS-RTK/IMU FGO and AR is introduced. The system states are initialized in the ENU frame based on extrinsic parameters between different sensors [98]. Notably, the body frame is aligned with the center of the IMU. All the involved system states are listed as:

1. The position $\mathbf{p}_{b,k}^{\mathrm{EN}}$ and orientation $\mathbf{q}_{b,k}^{\mathrm{EN}}$ of the IMU in ENU coordinates. k represents the k^{th} keyframe in the sliding window.

2. The velocity $\mathbf{v}_{b,k}^{\mathrm{EN}}$ of the IMU in ENU coordinate. $\mathbf{b}_{a,k}$ and $\mathbf{b}_{w,k}$ represent the bias of the gyroscope and accelerometer, respectively.

3. The DD integer ambiguities $N_{\mathrm{DD},r,t}^{S}$ of all received satellites $s \in S$ to receiver r at time epoch t.

4. The clock drift $\dot{\delta}_{r,t}$ of receiver r at time epoch t.

The system states within the sliding window can be further expressed as:

$$\begin{aligned} \boldsymbol{\chi} &= \left[\boldsymbol{x}_0, \cdots, \boldsymbol{x}_{K-1}, N_{DD,r,t_0}^{S}, \cdots, N_{DD,r,t_{n-1}}^{S}, \dot{\delta}_{r,t_0}, \cdots, \dot{\delta}_{r,t_{n-1}}\right] \\ \boldsymbol{x}_k &= \left[\mathbf{p}_{b,k}^{EN}, \mathbf{q}_{b,k}^{EN}, \mathbf{v}_{b,k}^{EN}, \mathbf{b}_{a,k}, \mathbf{b}_{w,k}\right] \\ N_{DD,r,t}^{S} &= \left[N_{DD,r,t}^{S_0}, \cdots, N_{DD,r,t}^{S_{m-1}}\right] \end{aligned} \tag{3.1}$$

where $k \in [0, \cdots, K-1]$, K represents the size of the sliding window, $t \in [t_0, \cdots, t_{n-1}]$ represents the received epoch of the GNSS signal, n represents the epoch number of the received GNSS measurements within the time interval of the sliding window, and m denotes the number of received satellites at time epoch .

To obtain the optimal state estimation based on the given measurements, the maximum posterior probability should be reached. The measurements are regarded as independent and with zero-mean Gaussian-distributed noise. The problem can be further simplified by solving the following objective function:

$$\begin{aligned} \boldsymbol{\chi}^{*} = \arg\min_{\boldsymbol{\chi}} \sum_{S,r,k,t} \Big(& \left\|\mathbf{r}_p - \mathbf{H}_p \boldsymbol{\chi}\right\| + \left\|\mathbf{r}_{L,k}\right\|_{\boldsymbol{\Sigma}_L}^{2} + \left\|\mathbf{r}_{B,k}\right\|_{\boldsymbol{\Sigma}_B}^{2} + \left\|\mathbf{r}_{DD,\rho,r,t}^{S}\right\|_{\sigma_\rho}^{2} \\ & + \left\|\mathbf{r}_{DD,\psi,r,t}^{S}\right\|_{\sigma_\psi}^{2} + \left\|\mathbf{r}_{DD,N,r,t}^{S}\right\|_{\sigma_N}^{2} + \left\|\mathbf{r}_{d,r,t}^{S}\right\|_{\sigma_d}^{2} \Big) \end{aligned} \tag{3.2}$$

where $\{\mathbf{r}_p, \mathbf{H}_p\}$ denotes the marginalized term as prior constraints. $\mathbf{r}_{\mathrm{B},k}$ represents the IMU factor, which is weighted by the relative covariance matrix Σ_B. Σ_B is es-

timated based on the inverse of the measurement noise covariance which is linearly propagated based on the given measurement white noise and the bias random walk within the integration interval [96]. $\mathbf{r}_{\mathrm{L},k}$ represents the VS factor from LiDAR measurements and is weighted by the covariance matrix Σ_L. The estimation of Σ_L will be introduced in the following section. $\mathbf{r}^S_{\mathrm{DD},\rho,r,t}$, $\mathbf{r}^S_{\mathrm{DD},\psi,r,t}$, and $\mathbf{r}^S_{d,r,t}$ denote the DD GNSS pseudorange, carrier phase, and Doppler factors, respectively. The uncertainties of different observations are given as $\sigma_\psi = \frac{\sigma_\rho}{100}$ and $\sigma_d = \sigma_\rho$, where the σ_ρ is initialized by SNR and elevation angle following the method in *goGPS* software [99]. The parameters are $A = 30$, $s_0 = 10$, $s_1 = 50$, $a = 30$. The parameters s_1, s_0, A, and a define the specific shape of the C/N0-dependent weighting curve, particularly for lower-quality signals. s_1 serves as a quality threshold; if the C/N0 exceeds this value, the measurement is considered "good" and the weight factor defaults to 1. The parameters s_0 and A act as an anchor point for the curve, where s_0 is the specific C/N0 value at which the function is "forced" to take on the weight specified by A. Finally, a controls the "bending" or curvature of the function, determining how steeply the weight drops as signal quality decreases. $\mathbf{r}^S_{\mathrm{DD},N,r,t}$ denotes the constant integer ambiguity factor weighted by $\sigma_N = \sigma_\psi$.

The factor graph structure of the proposed system is shown in Fig. 3.3. The VS factors and IMU factors directly constrain the system states $\mathbf{x}_k$. Notably, due to the difference in the data frequency, the GNSS factors (DD pseudorange, DD carrier phase, and Doppler factors) constrain the system states $\mathbf{x}_k$ and $\mathbf{x}_{k+1}$ through interpolated states $\mathbf{x}_t$ at time epoch t, with $\mathbf{x}_t \in (\mathbf{x}_k, \mathbf{x}_{k+1})$.

GNSS DD Pseudorange/Carrier Phase Factor

The pseudorange measurement $\rho^s_{r,t}$ of the GNSS receiver r at time t is expressed by:

$$\rho^s_{r,t} = r^s_{r,t} + c\left(\delta_{r,t} - \delta_{s,t}\right) + I^s_{r,t} + T^s_{r,t} + \varepsilon^s_{\rho,r,t} \tag{3.3}$$

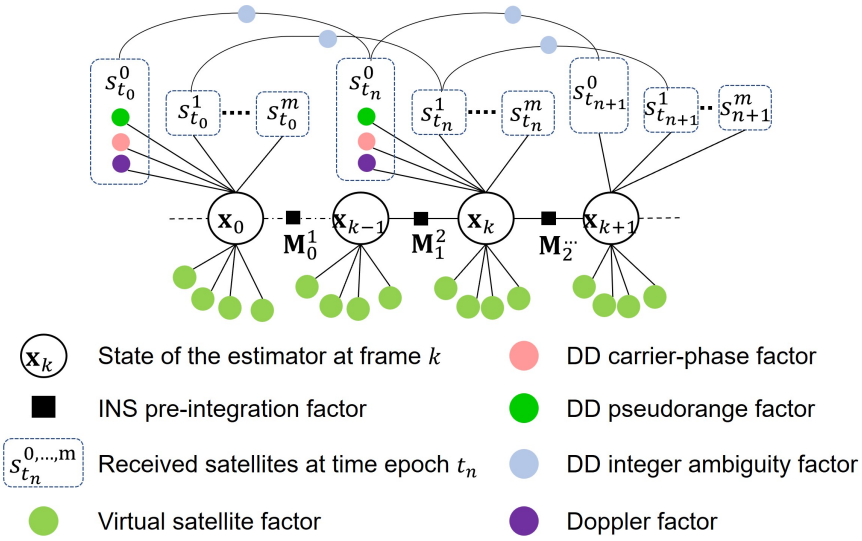

Figure 3.3: The factor graph of the proposed tightly-coupled integration system.

where $r^s_{r,t}$ denotes the geometric range between satellite s and receiver r at time epoch t. $I^s_{r,t}$ represents the ionospheric delay distance, $T^s_{r,t}$ represents the tropospheric delay distance. $\varepsilon^s_{\rho,r,t}$ denotes the other errors including multipath error, NLOS error, receiver noise error, and antenna phase-related noise error.

Similar to the pseudorange, the carrier phase measurements of the GNSS receiver r at time t can be expressed as:

$$\lambda\psi^s_{r,t} = r^s_{r,t} + c\left(\delta_{r,t} - \delta_{s,t}\right) - I^s_{r,t} + T^s_{r,t} + \lambda B^s_{r,t} + d\psi^s_{r,t} + \varepsilon^s_{\psi,r,t} \tag{3.4}$$

where $B^s_{r,t} = \psi_{r,t,0} - \psi^s_{0,r,t} + N^s_{r,t}$ represents the carrier phase bias. The variable $\psi_{r,t,0}$ denotes the initial phase of the receiver's local oscillator. $\psi^s_{0,r,t}$ is the initial phase of the transmitted navigation signal from the satellite. The variable $N^s_{r,t}$ is the carrier phase integer ambiguity which should be an integer value. λ denotes the carrier wavelength of the respective satellite system. $d\psi^s_{r,t}$ represents the carrier phase correction terms, which contain antenna phase offsets and variations, station displacement by earth tides, phase windup effects, and a relativity correction on the satellite clock. $\varepsilon^s_{\psi,r,t}$ represents errors caused by multipath effects, NLOS receptions,

receiver noise, and antenna delay.

Based on the measurement model, it is observed that the clock-based and atmosphere-based systematic errors have great influences on positioning accuracy. Therefore, the DD technique is introduced in the GNSS-RTK positioning method. The DD method first conducts a single-difference between the measurements from different receivers (receiver r and reference station e) from the same satellite and then performs a subtraction between the results of the single difference from two satellites. Particularly, the master satellite w is selected with the highest elevation angle among all received satellites, as satellites with higher elevation angles are inclined to suffer less from multipath and NLOS receptions. For certain time epochs and satellite systems, all the other satellites share the same master satellite. The formulation of the DD pseudorange and DD carrier phase can be concluded as:

$$\rho^s_{\mathrm{DD},r,t} = \left(\rho^s_{r,t} - \rho^s_{e,t}\right) - \left(\rho^w_{r,t} - \rho^w_{e,t}\right) \tag{3.5}$$

$$\psi^s_{\mathrm{DD},r,t} = \left(\psi^s_{r,t} - \psi^s_{e,t}\right) - \left(\psi^w_{r,t} - \psi^w_{e,t}\right) \tag{3.6}$$

Considering that the receiver r and reference station e are under similar atmospheric conditions, a single difference operation can eliminate the effect of atmospheric errors as well as the satellite clock bias, but the receiver clock bias term remains. The second difference operation further eliminates the receiver clock bias. Therefore, the DD pseudorange and DD carrier phase measurements model can be further expressed as:

$$\rho^s_{\mathrm{DD},r,t} = \left(r^s_{r,t} - r^s_{e,t}\right) - \left(r^w_{r,t} - r^w_{e,t}\right) + \varepsilon^s_{\mathrm{DD},\rho,r,t} \tag{3.7}$$

$$\lambda\psi^s_{\mathrm{DD},r,t} = \left(r^s_{r,t} - r^s_{e,t}\right) - \left(r^w_{r,t} - r^w_{e,t}\right) + N^s_{\mathrm{DD},r,t} + \varepsilon^s_{\mathrm{DD},\psi,r,t} \tag{3.8}$$

where $\varepsilon^s_{\mathrm{DD},\rho,r,t}$ and $\varepsilon^s_{\mathrm{DD},\psi,r,t}$ represent the noise of DD pseudorange measurements and carrier phase measurements. $N^s_{\mathrm{DD},r,t}$ is the DD integer ambiguity of satellite s,

which is one of the system states to be estimated. Given the DD measurement model above, the DD pseudorange residuals and DD carrier phase residuals are formed as:

$$r^s_{\mathrm{DD},\rho,r,t} = \rho^s_{\mathrm{DD},r,t} - (r^s_{r,t} - r^s_{e,t}) - (r^w_{r,t} - r^w_{e,t}) \tag{3.9}$$

$$r^s_{\mathrm{DD},\psi,r,t} = \lambda\psi^s_{\mathrm{DD},r,t} - (r^s_{r,t} - r^s_{e,t}) - (r^w_{r,t} - r^w_{e,t}) - N^s_{\mathrm{DD},r,t} \tag{3.10}$$

where the range distances $r^s_{r,t}$, $r^s_{e,t}$, $r^w_{r,t}$, and $r^w_{e,t}$ are calculated based on the positions of the GNSS receiver:

$$r^s_{r,t} = \left\|\mathbf{p}^{\mathrm{EC}}_{r,t} - \mathbf{p}^{\mathrm{EC}}_{s,t}\right\|, \quad r^s_{e,t} = \left\|\mathbf{p}^{\mathrm{EC}}_{e} - \mathbf{p}^{\mathrm{EC}}_{s,t}\right\| \tag{3.11}$$

$$r^w_{r,t} = \left\|\mathbf{p}^{\mathrm{EC}}_{r,t} - \mathbf{p}^{\mathrm{EC}}_{w,t}\right\|, \quad r^w_{e,t} = \left\|\mathbf{p}^{\mathrm{EC}}_{e} - \mathbf{p}^{\mathrm{EC}}_{w,t}\right\| \tag{3.12}$$

where $\|\cdot\|$ denotes the norm of the vector. $\mathbf{p}^{\mathrm{EC}}_{s,t}$ and $\mathbf{p}^{\mathrm{EC}}_{w,t}$ are satellite positions transformed in the ECEF frame, $\mathbf{p}^{\mathrm{EC}}_{e}$ is the position of the reference station in the ECEF frame. The estimated $\mathbf{p}^{\mathrm{EC}}_{r,t}$ is the position of the GNSS receiver r at time epoch t in the ECEF frame transformed from $\mathbf{p}^{\mathrm{EN}}_{r,t}$. Notably, the transformation from ENU to ECEF according to the origin point $\mathbf{p}^{\mathrm{EC}}_{o}$ is calculated as:

$$\mathbf{p}^{\mathrm{EC}}_{r,t} = \mathbf{R}^{\mathrm{EC}}_{\mathrm{EN}}\mathbf{p}^{\mathrm{EN}}_{r,t} + \mathbf{p}^{\mathrm{EC}}_{o} \tag{3.13}$$

$$\mathbf{R}^{\mathrm{EC}}_{\mathrm{EN}} = \begin{bmatrix} -\sin\lambda_o & -\sin\phi_o\cos\lambda_o & \cos\phi_o\cos\lambda_o \\ \cos\lambda_o & -\sin\phi_o\sin\lambda_o & \cos\phi_o\sin\lambda_o \\ 0 & \cos\phi_o & \sin\phi_o \end{bmatrix} \tag{3.14}$$

where λ_o and ϕ_o denote the geographic latitude and longitude of the known origin point $\mathbf{p}^{\mathrm{EC}}_{o}$.

Further, the receiver's position $\mathbf{p}^{\mathrm{EN}}_{r,t}$ is obtained from the estimated states $\mathbf{p}^{\mathrm{EN}}_{b,t}$ maintained in the body frame as:

$$\mathbf{p}^{\mathrm{EN}}_{r,t} = \mathbf{p}^{\mathrm{EN}}_{b,t} + \mathbf{R}^{b}_{r}\mathbf{p}^{b}_{r} \tag{3.15}$$

In addition, the maintained states are with LiDAR keyframe time t_K rather than GNSS epoch time t. Therefore, linear interpolation is adopted between the system states $\mathbf{p}_{b,k}^{\mathrm{EN}}$ and $\mathbf{p}_{b,k+1}^{\mathrm{EN}}$ in the adjacent epochs t_k and t_{k+1} with $t \in [t_k, t_{k+1}]$ to obtain the corresponding state $\mathbf{p}_{b,t}^{\mathrm{EN}}$, which is calculated based on the ratio of the time interval:

$$\mathbf{p}_{b,t}^{\mathrm{EN}} = \left\{ \frac{t - t_k}{t_{k+1} - t_k} \mathbf{p}_{b,k}^{\mathrm{EN}} + \frac{t_{k+1} - t}{t_{k+1} - t_k} \mathbf{p}_{b,k+1}^{\mathrm{EN}} \right\} \tag{3.16}$$

GNSS Constant Integer Ambiguity Factor

GNSS-RTK positioning accuracy suffers if cycle slips are not detected and properly handled. Cycle slip occurs when the receiver's phase lock on the signal is lost. In urban canyons, the most common reason for cycle slips is an obstruction (e.g., buildings, trees) which blocks the signal and therefore results in signal tracking failure. In this case, the previously resolved integer ambiguities become instantly unknown and need to be resolved again. When there is no cycle slip, the integer ambiguity of one satellite in adjacent epochs remains the same. The constant integer ambiguity residual can be formed as:

$$r_{\mathrm{DD},N,r,t}^{s} = N_{\mathrm{DD},r,t}^{s} - N_{\mathrm{DD},r,t-1}^{s} \tag{3.17}$$

where $N_{\mathrm{DD},r,t}^{s}$ and $N_{\mathrm{DD},r,t-1}^{s}$ represent the integer ambiguities of satellite s at time epoch t and epoch $t-1$, respectively.

To effectively eliminate the impact of cycle slips, we adopt a LiDAR-aided cycle slip detection method [97], which employs the consistency check of the triple difference, which is formed from two double differences over two different epochs. To perform TD estimation, we predict the states by LiDAR and IMU measurements. According to 3.8, the DD integer ambiguity for satellite s at time epoch t is estimated

as:

$$N^s_{\mathrm{DD},r,t} = \lambda \psi^s_{\mathrm{DD},r,t} - \left((r^s_{r,t} - r^s_{e,t}) - (r^w_{r,t} - r^w_{e,t}) \right) \tag{3.18}$$

then the TD integer ambiguity between time epoch t and $t-1$ can be calculated by:

$$N^s_{\mathrm{TD},r,t} = N^s_{\mathrm{DD},r,t} - N^s_{\mathrm{DD},r,t-1} \tag{3.19}$$

when $N^s_{\mathrm{TD},r,t}$ is larger than a certain threshold $N^{\mathrm{threshold}}_{\mathrm{TD}}$, the cycle slip occurs at time t. The threshold $N^{\mathrm{threshold}}_{\mathrm{TD}}$ is set as 3 cycles as described in [97]. According to 3.18, the TD uses range distance to estimate the DD integer ambiguity, which relies on the high quality of the initial guess of the position. Thanks to LiDAR and IMU, the system can provide a high-quality initial guess, which even enables the detection of small cycle slips.

GNSS Doppler Factor

Doppler measurement $d^s_{r,t}$ at receiver r from satellite s at time epoch t is denoted as:

$$\lambda d^s_{r,t} = \mathbf{e}^{s,\mathrm{LOS}}_{r,t} \cdot (\mathbf{v}^{\mathrm{EC}}_{s,t} - \mathbf{v}^{\mathrm{EC}}_{r,t}) + c(\dot{\delta}^i_{r,t} - \dot{\delta}_{s,t}) + \zeta^s_{r,t} \tag{3.20}$$

where $\zeta^s_{r,t}$ represents the noise of the received Doppler measurement, c denotes the speed of light, and λ denotes the carrier wavelength of the respective satellite constellation system. The velocity of the receiver in the ECEF frame is transformed from the ENU frame using $\mathbf{v}^{\mathrm{EC}}_{r,t} = \mathbf{R}^{\mathrm{EC}}_{\mathrm{EN}} \mathbf{v}^{\mathrm{EN}}_{r,t}$. $\mathbf{e}^{s,\mathrm{LOS}}_{r,t}$ is the LOS unit vector between the position of receiver r and the satellite s at time epoch t, which is calculated by:

$$\mathbf{e}^{s,\mathrm{LOS}}_{r,t} = \left(\frac{\mathbf{p}^{\mathrm{EC}}_{s,t} - \mathbf{p}^{\mathrm{EC}}_{r,t}}{\left\| \mathbf{p}^{\mathrm{EC}}_{s,t} - \mathbf{p}^{\mathrm{EC}}_{r,t} \right\|} \right)^T \tag{3.21}$$

Given the Doppler measurement model above, the residual is derived as:

$$r^s_{d,r,t} = d^s_{r,t} - \frac{1}{\lambda_i}\left(\mathbf{e}^{s,\mathrm{LOS}}_{r,t} \cdot (\mathbf{v}^{\mathrm{EC}}_{s,t} - \mathbf{v}^{\mathrm{EC}}_{r,t}) + c(\dot{\delta}^i_{r,t} - \dot{\delta}_{s,t})\right) \tag{3.22}$$

Inertial Factor

The IMU measurements comprise linear acceleration and angular velocity with the effect of corresponding bias and additive noises. Knowing that the frequency of the inertial measurements is practically much higher than other sensors (LiDAR, GNSS), the pre-integration method [10; 96] is further adopted in our optimization to integrate multiple raw inertial measurements into a single relative pose constraint between two consecutive keyframes k and $k+1$. We follow the work from [10] for the implementation. The readers can refer to [10; 96] for detailed formulation of the inertial factors.

LiDAR Landmark-Based VS Factor

The satellite geometry is often poor in urban areas and will be further deteriorated by NLOS exclusion. As shown in Fig. 3.4(a), only LOS satellites (the blue circles) with high elevation angles remain after the GNSS NLOS exclusion. In this scenario, the position estimation has a large uncertainty in the direction perpendicular to the street, and thus the float solutions that can be obtained are more likely to suffer from large errors due to small observation bias. On the contrary, as shown in Fig. 3.4(b), the green stars denote the VS, which mainly arise from low-lying environmental structures and are highly complementary with high-elevation angle LOS satellites. The state uncertainties arising from GNSS observations can be adequately bounded by VS.

The employment of VS measurements and constraints follows a similar manner to the popular feature-based LiDAR-SLAM methods [11]. We have evaluated edge-based and plane-based LiDAR odometry in urban areas. The results showed that

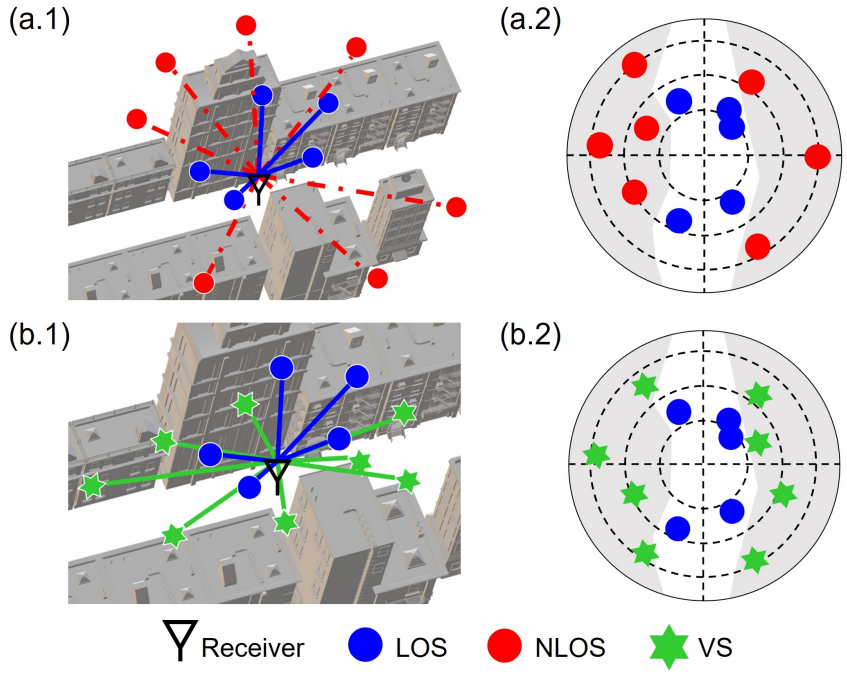

Figure 3.4: Illustration of VS-aided GNSS-RTK positioning.

planar features obtained better accuracy and higher robustness. Therefore, planar constraints are applied in a scan-to-map scheme, where the map denotes a local 3D point cloud feature map accumulated by recent keyframes. For each keyframe, feature points of planes are extracted by evaluating the local distribution of the neighboring patch. Then the plane correspondences are found by a nearest neighbor search between the keyframes and the local feature map and examined by eigenvalue analysis on the feature patches. Given the transformed planar point $\mathbf{p}_{p,k}^{\mathrm{EN}}$ in frame k and corresponding planar points $\mathbf{p}_{p,k,a}^{\mathrm{EN,M}}$, $\mathbf{p}_{p,k,b}^{\mathrm{EN,M}}$ and $\mathbf{p}_{p,k,c}^{\mathrm{EN,M}}$ representing the planar patch in the local feature map M in the ENU frame, the point-to-plane residual is calculated as [11]:

$$r_{l,s,k} = \left\| \frac{\left(\mathbf{p}_{p,k}^{\mathrm{EN}} - \mathbf{p}_{p,k,a}^{\mathrm{EN,M}}\right) \cdot \left[\left(\mathbf{p}_{p,k,a}^{\mathrm{EN,M}} - \mathbf{p}_{p,k,b}^{\mathrm{EN,M}}\right) \times \left(\mathbf{p}_{p,k,a}^{\mathrm{EN,M}} - \mathbf{p}_{p,k,c}^{\mathrm{EN,M}}\right)\right]}{\left\|\left(\mathbf{p}_{p,k,a}^{\mathrm{EN,M}} - \mathbf{p}_{p,k,b}^{\mathrm{EN,M}}\right) \times \left(\mathbf{p}_{p,k,a}^{\mathrm{EN,M}} - \mathbf{p}_{p,k,c}^{\mathrm{EN,M}}\right)\right\|} \right\| \tag{3.23}$$

$$\mathbf{p}_{p,k}^{\mathrm{EN}} = \mathbf{R}_{b,k}^{\mathrm{EN}} \left(\mathbf{R}_{l}^{b} \mathbf{p}_{p,k}^{l} + \mathbf{p}_{l}^{b} \right) + \mathbf{p}_{b,k}^{\mathrm{EN}} \tag{3.24}$$

where $\mathbf{p}_{p,k}^{l}$ represents the planar point in k^{th} LiDAR keyframe, $\mathbf{T}_{l}^{b} = \begin{bmatrix} \mathbf{R}_{l}^{b} & \mathbf{p}_{l}^{b} \end{bmatrix}$ denotes the transformation matrix from the LiDAR frame to the body frame, $\mathbf{T}_{b,k}^{\mathrm{EN}} = \begin{bmatrix} \mathbf{R}_{b,k}^{\mathrm{EN}} & \mathbf{p}_{b,k}^{\mathrm{EN}} \end{bmatrix}$ denotes the transformation matrix from the k^{th} local body frame to the ENU frame.

Compared with GNSS observations, which are usually fewer than 20 in urban areas due to limited satellite availability, LiDAR provides far more observations in a single frame (averaging more than 2000 per frame for a 32-line mechanical LiDAR in our experiment). Integrating a huge amount of LiDAR constraints with limited GNSS observations leads to two problems. First, it will increase the complexity of the optimization problem exponentially, requiring more computational resources and decreasing the system efficiency. Second, it would prevent a balanced contribution of satellite and LiDAR information to the optimization. The large number of LiDAR constraints will dominate the optimization problem when the weighting strategy only considers the observation error and not the number of observations.

Knowing that each LiDAR frame has a large information redundancy, using fewer LiDAR observations can significantly reduce system complexity and improve operational efficiency while ensuring sufficient state observability [100]. We want to analyze the effect of different numbers of LiDAR observations on the estimation uncertainty and provide its minimum interval in real environments that maintains the estimation accuracy of the integrated system. To evaluate the contribution of the number of LiDAR observations to state estimation, we construct the information matrix based on LiDAR observations and track its eigenvalues [101]. This method was originally used for investigating the degeneracy of LiDAR constraints in different environments, and we adopt it to assess the degeneracy of LiDAR constraints with different numbers

of observations. The information matrix is the inverse of the covariance matrix of the state, which indicates the certainty of the final estimates under the observations. The degeneracy of LiDAR constraints is defined as [101]:

$$Degeneracy\ Level = \lambda_{\min} + 1 \tag{3.25}$$

where $\lambda_{\min}$ represents the smallest eigenvalue of information matrix Λ_l. For the calculation of Λ_l, we have:

$$\Lambda_l = \mathbf{J}_p^{L^T} \mathbf{J}_p^L \tag{3.26}$$

where $\mathbf{J}_p^L$ denotes the Jacobian matrix of the residuals of LiDAR constraints with respect to the pose states.

The weighting strategy of the VS factor is jointly determined by three aspects, namely the LiDAR observation uncertainty, the position uncertainty of the local map, and the quantity ratio between LiDAR and GNSS observations. The LiDAR observation uncertainty is given by measuring the geometric and appearance consistencies of associated features between the scan and the map [30]. Noticing that the local map is consistently extended and updated by the latest estimates, therefore, in the absence of a reliable GNSS epoch for a certain period, the uncertainty of position estimation and the corresponding map gradually increase due to the lack of a global constraint [28]. As a result, the uncertainty of the VS factors increases along with the uncertainty of the map. Moreover, to balance the impact of the VS and the original satellites in the optimization, the constraints constructed from VS are further dynamically weighted based on the quantity ratio between the numbers of VS and real satellites instantly, which is calculated by:

$$w_t^l = \frac{n_{\text{virtual}}^l}{n_{\text{real}}^l} \tag{3.27}$$

where n^l_{virtual} represents the constraint's number of VS, n^l_{real} represents the constraint number of real satellites. This enables real satellites to be effective even in small numbers, which is common in urban cases.

Marginalization Factor

To release the computational load and meanwhile maintain the impacts of the constraints from the previous information, marginalization is adopted in the sliding window optimization. We gradually marginalize the constraints from the older keyframes sliding out the window through the Schur complement [102]. The corresponding new prior factor is further added in the updated window.

Given the factors above, the optimized states and their respective covariance matrix are obtained after the tightly-coupled optimization. Knowing that the double-differenced integer ambiguities should indeed be integer values, the estimated float values of integer ambiguities can be resolved as integer values and the position results can be corrected with higher accuracy, whereas a fixed solution is reached. To solve the integer ambiguity resolution problem, the modified LAMBDA algorithm [18] is adopted for its efficiency.

3.3 Experimental Results

The proposed system is implemented using C++ on Robot Operation System (ROS) [103]. We use Ceres Solver [104] and GTSAM [105] for the nonlinear optimization as well as the pose graph optimization. The experimental evaluation is conducted on three challenging sequences collected in Hong Kong, namely Urban Canyon 1, Urban Canyon 2, and Urban Canyon 3, which contain various levels of urbanized scenarios. Urban Canyon 1 and 2 are collected in Kowloon Tong with durations around 150s and 400s, respectively. Urban Canyon 3 (1500s) is from our open-sourced dataset, *UrbanNav* [106], which is collected in Whampoa. There are densely distributed static

buildings, tall trees, and dynamic objects (wagons, double-decker buses) that bring potential GNSS NLOS receptions.

3.3.1 Experiment Platform

The data collection is based on the experimental platform proposed in *UrbanNav*. A low-cost GNSS receiver, the u-blox M8T, is employed to collect raw single-frequency GPS/BeiDou signals at 10 Hz. The *Xsens* MTi-10 IMU is adopted to collect inertial measurements at a frequency of 100 Hz. A HDL-32E LiDAR collects 3D measurements at a frequency of 10 Hz. Moreover, the *NovAtel* SPAN-CPT, an integration system from multi-frequency and constellation GNSS-RTK and IMU with fiber-optic gyroscopes (FOG, 1 degree per hour for gyroscope bias, 0.067 degrees per hour as random walk), is employed to provide ground truth. In the implementation, data from different sources are synchronized via Pulse-Per-Second (PPS) hardware in the computer. The extrinsic parameters between different sensors are carefully calibrated before the experiments. The initial transformation from local coordinates to global coordinates is provided in advance by aligning the first position to the ground truth.

3.3.2 Evaluation of the impact of different numbers of LiDAR observations on the degeneracy factor of state estimation

We analyze the variation of the degeneracy factor with different numbers of LiDAR observations. The minimum number interval of observations will be set to maintain the degeneracy factor not decrease significantly. The variation of degeneracy factor with changing observation number is presented in Fig. 3.5. It is observed that the degeneracy factor consistently stays at low values utilizing 20 LiDAR observations per frame, which indicates that the constraints are insufficient and the final estimation results are subject to greater uncertainty.

Accordingly, larger LiDAR relative positioning errors are observed in the right panel of Fig. 3.5 for the case of using 20 observations, and these positioning errors will be introduced into the integration system, which will eventually affect the final positioning accuracy. As the number of LiDAR observations increases, the degradation factor has a clear upward trend and the relative positioning accuracy using LiDAR observation shows a downward trend.

This means that with more available observations, the state uncertainty will be significantly reduced due to stronger constraints. As shown in the right panel of Fig. 3.5, we use the degeneracy factor ratio (DFR) and the maximum relative positioning error (Max RPE) to illustrate the trending of positioning error with different observation number. The DFR is obtained by calculating the ratio of the degradation factor with a specific number of LiDAR observations and with a sufficient number of LiDAR observations (the sufficient number is set to 1200). To present the data more clearly, we directly use the minimum eigenvalue of the information matrix in the calculation of the DFR, which is slightly different from the definition of the above 3.25. The Max RPE is obtained by evaluating the relative positioning performance of the LIO system [30] with a specific number of LiDAR observations.

We consider that the interval where both the degradation factor and the relative positioning accuracy curve have reached an initial smooth state can be regarded as an effective interval to set the minimum number of LiDAR observations. We use 200 LiDAR observations per frame. The evaluation of final positioning accuracy and the system efficiency is provided in the following sections.

3.3.3 Evaluation of the performance of the 3D LiDAR aided NLOS mitigation

Different from traditional NLOS detection methods, the 3D LiDAR aided NLOS detection approach is independent of position estimation, and completely relies on

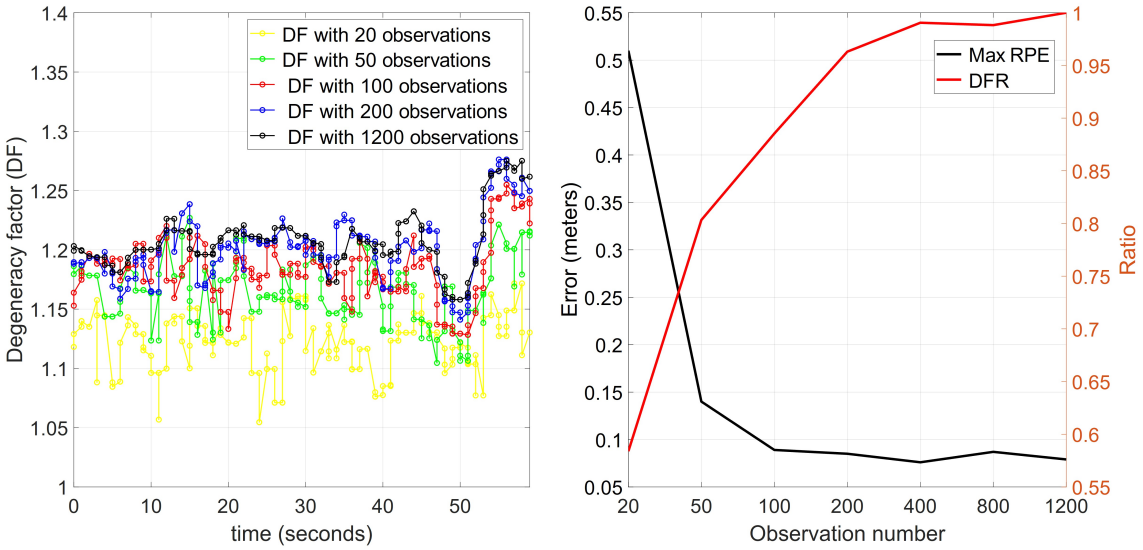

Figure 3.5: Illustration of degeneracy factor (DF) with different LiDAR observation numbers is given on the left panel, LiDAR observation numbers are compared from 20 observations to 1200 observations, represented by yellow, green, red, blue, and black curves with circle marks. The tendency curve of degeneracy factor ratio (DFR) and maximum relative positioning error (Max RPE) with different LiDAR observation numbers are given on the right panel, where the maximum relative positioning error is depicted by the black curve and the degeneracy factor ratio is depicted by the red curve.

the precision of attitude and the degree of reconstruction about the surroundings, especially in the vertical direction. Compared to the previous 3DLA method, in this system, we incorporate global pose graph optimization to update the 3D PCM used for NLOS detection. This improvement addresses the issue of false positives of NLOS detection caused by PCM drift in the previous method [22]. Fig. 3.6 illustrates how the drift error of attitude estimation will mislead the NLOS classification. The left figure shows the result of NLOS detection based on the global optimized drift-free PCM while the right figure represents the results on drifted PCM. The accumulated attitude drift significantly alters actual satellite occlusion, preventing correct detection of NLOS receptions. Furthermore, the positioning error of the above two cases is compared in Table. 3.1, the method with accumulated drift shows higher error, which is because some NLOS receptions are not detected, and healthy measurements

are mistakenly classified as NLOS and excluded.

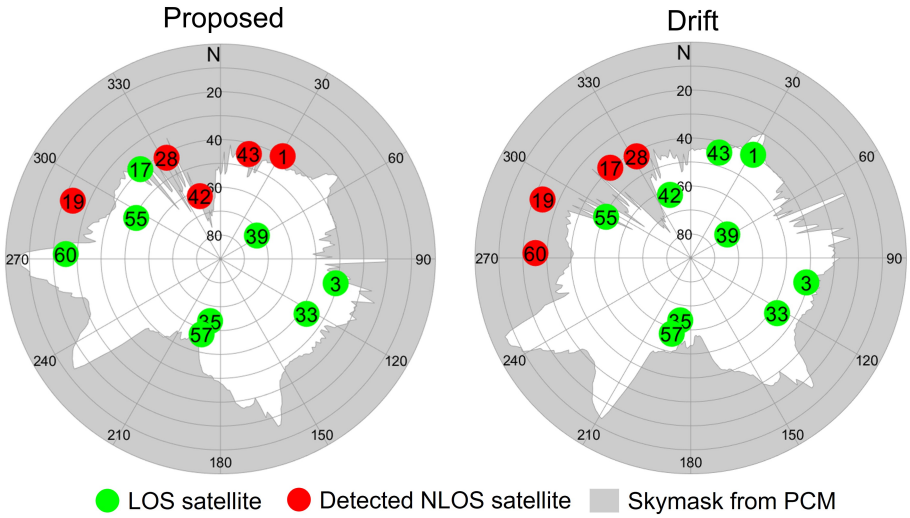

Figure 3.6: Comparison between the NLOS detection methods based on the globally optimized drift-free PCM (left) and the drifted PCM (right). The skymasks generated from different PCMs are shown in gray.

Table 3.1: Positioning Performance (meters) of the Evaluated Three Cases for the Selected Epoch in Urban Canyon 1.

	Drift PCM	Proposed (20 keyframes)	Proposed (60 keyframes)
3D Error (m)	1.96	1.17	**0.55**

We have also evaluated the proposed method with different sliding window lengths to demonstrate the ability of the PCM to reconstruct the environment and thus aid NLOS detection. Fig. 3.7 shows the comparison of NLOS detection through the PCM generated by the different sliding window sizes. As the window size in the left figure is 60 keyframes as default and in the right figure is 20 keyframes, it is apparent that the upper part of the building has been more thoroughly rebuilt in the left figure than in the right one. In other words, the larger sliding window size represents a more complete reconstruction of the environment, thus allowing a more accurate determination of the satellite occlusion. The evaluation results are shown in Table. 3.1.

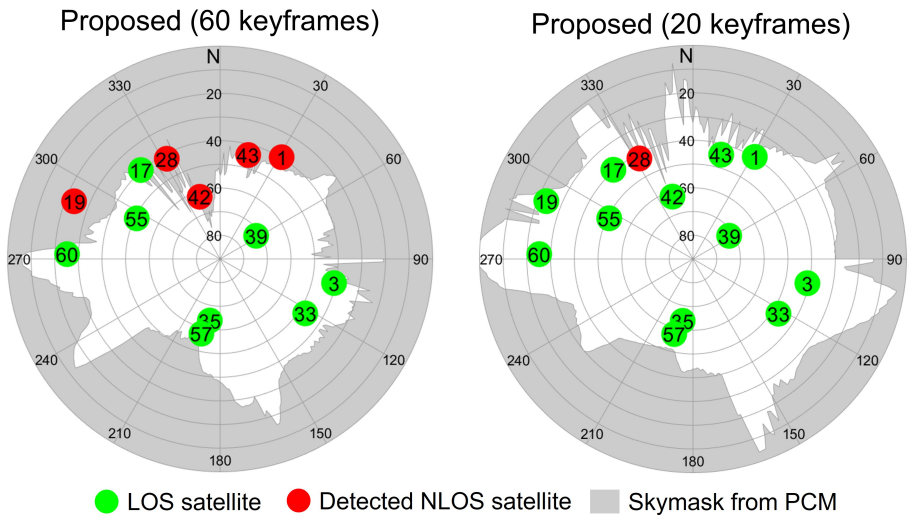

Figure 3.7: Comparison between the results of NLOS detection methods based on different sliding window sizes.

To demonstrate the long-term effectiveness of the proposed 3DLA NLOS mitigation method in real-world environments and compare it with representative existing methods, we further compared the proposed method with the 3DMA GNSS-RTK [107] in terms of NLOS detection results, as shown in Fig. 3.8. Both methods are evaluated in Urban Canyon 3.

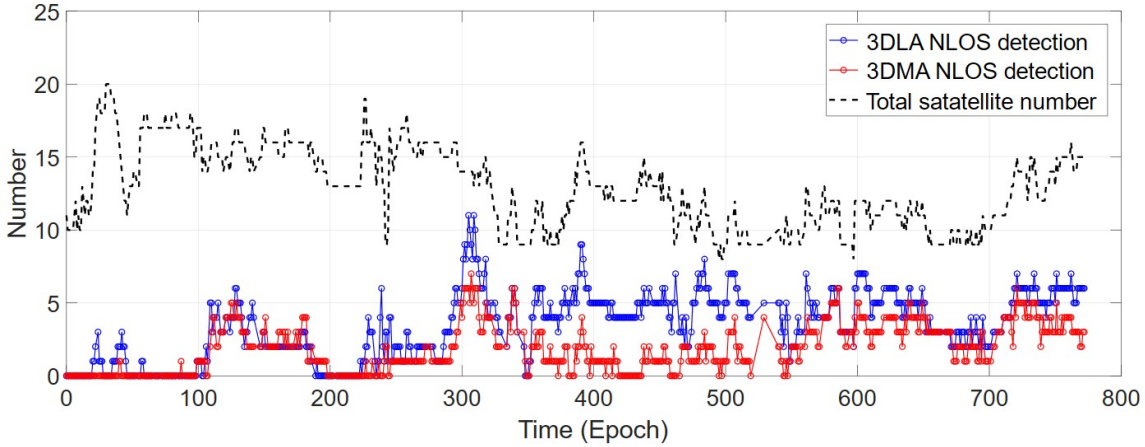

Figure 3.8: Comparison between the results of different NLOS detection methods. The black dashed line represents the number of the received satellites. The red line marked with circles denotes the number of detected NLOS satellites from the 3DMA GNSS-RTK method, and the blue line marked with circles denotes the number of detected NLOS satellites from the proposed method.

The data from the Hong Kong Common Spatial Data Infrastructure Portal is used to generate the 3D building model. Based on the result, it is observed that both methods exhibit similar overall trends, showing an increased number of NLOS detections when the available satellite number changes rapidly. Notably, the average number of NLOS detections in the proposed method is relatively higher compared to the 3DMA GNSS-RTK, which is because the proposed method utilizes 3D PCM constructed from real-time observation information, which can fully and accurately represent the occlusion of signals by surrounding environmental factors such as buildings, large vehicles, vegetation, road infrastructure, and so on. In contrast, the 3DMA GNSS-RTK method is limited by the accuracy and resolution of the 3D model, unable to consider the effects of various dynamic and static objects in the real environment other than buildings. On the other hand, this suggests that the proposed method is more sensitive to dynamic environments, and excessive exclusion of NLOS measurements can significantly impact satellite geometry distribution. Therefore, in loosely-coupled systems, the proposed method can be combined with traditional residual-based outlier detection methods when the system is initialized.

3.3.4 Evaluation of the positioning performance of the proposed tightly-coupled GNSS/LiDAR/INS integration with 3D LiDAR aided NLOS mitigation

To evaluate the positioning performance of the proposed method, the following methods are evaluated and compared qualitatively and quantitatively in multiple aspects. First, mean error, maximum error, and standard deviation in both 2D and 3D cases will demonstrate the positioning accuracy of different methods. Second, we utilize the ambiguity fixing rate to indicate the effectiveness of geometry improvement by the proposed method. The ambiguity fixing rate indicates the percentage of fixed solutions to the total number of solutions. The successfully fixed solution is deter-

mined when the 3D positioning error is less than 20cm and the ratio test is passed with threshold 3. Moreover, the availability is evaluated to compare the positioning ability, which is the percentage of the number of solutions to the total number of epochs. The evaluated methods are listed as follows:

1. **GNSS-RTK:** RTKLIB [108] is evaluated to represent the performance of conventional GNSS-RTK. Forward filtering is adopted under the fix-and-hold condition.

2. **LIO:** LiDAR/Inertial integration method [30] is evaluated to demonstrate the performance of pure LiDAR/inertial odometry.

3. **LC GNSS-RTK-LIO:** Loosely-coupled (LC) integration between GNSS-RTK and LIO system [28]. This is performed to show the improvement of positioning by loosely integrating the GNSS-RTK with the LIO system compared with standalone systems.

4. **3DLA GNSS-RTK:** The proposed tightly-coupled VS-aided GNSS-RTK/IMU integrated system. This is to show the effectiveness of geometry improvement by VS.

5. **3DLA GNSS-RTK-NE:** The proposed tightly-coupled VS-aided GNSS-RTK/IMU integrated system with drift-free NLOS exclusion. This is to demonstrate the final performance of the proposed method.

Evaluation of Urban Canyon 1

Table. 3.2 shows the evaluation results of each method. The trajectory and the 3D positioning error are illustrated in Fig. 3.9 and Fig. 3.10 GNSS-RTK obtains 1.55 meters as the 2D mean error and 3.54 meters as 3D mean errors, and its maximum error reaches 15.88 meters in 2D and 29.23 meters in 3D. By analyzing the locations

where large errors occur (the orange box in Fig. 3.9 corresponds to time intervals around the 70s and 120s in Fig. 3.10), it is found that these spots all suffer from dense buildings and trees, which caused severe NLOS receptions with greatly deteriorated accuracy. As a result, the conventional GNSS-RTK method only achieves an ambiguity fixing rate of 1.61%. and LiDAR/IMU.

On the other hand, the LIO method achieved a mean error of 0.32 meters in 2D and 1.30 meters in 3D. Notably, we provide accurate initialization for LIO. We can observe that the LIO can maintain a high relative positioning accuracy within a short trajectory. However, it suffers from drift with increasing driving distance and ends with a maximum 3D error of 2.79 meters. We further refer to the result of the loosely-coupled method LC GNSS-RTK-LIO and notice the deteriorated positioning accuracy, which is between GNSS-RTK and LIO, as LIO can only help GNSS-RTK with relative pose constraints to provide a smoother positioning result, but the global positioning accuracy is dominated by GNSS-RTK solutions. The positioning accuracy of LC GNSS-RTK-LIO is 1.42 meters in 2D and 3.00 meters in 3D with better smoothness compared with the result of GNSS-RTK. In other words, the loosely-coupled method can cope with the drift problem in long-term operation but the local positioning accuracy is greatly affected by the GNSS-RTK result. Therefore, the improvement is still limited by unhealthy GNSS measurements and underutilized complementary characteristics of GNSS **3DLA GNSS-RTK** as a tightly-coupled system integrating the raw measurements from GNSS DD pseudorange, DD carrier phase, and Doppler with VS and IMU measurements, shows significant improvement compared with the conventional GNSS-RTK method and its loosely-coupled integration method with LIO: 2D error and 3D error decrease to 0.39 and 1.53 meters, whereas the standard deviation and maximum error are 1.78 and 5.29 meters respectively for the 3D case.

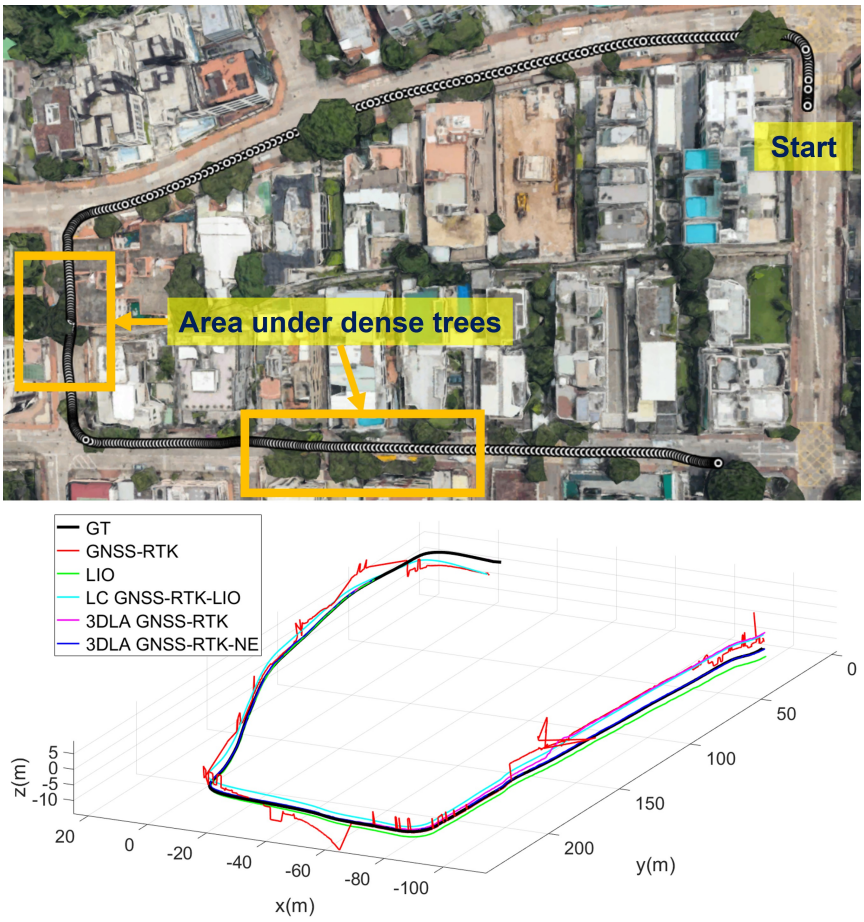

Figure 3.9: The trajectory in Urban Canyon 1. The upper panel shows the projected trajectories on Google Earth. The orange box denotes the area with challenging signal blockage by trees. The lower panel shows the 3D trajectories of different methods. The red, green, cyan, magenta and blue curves denote GNSS-RTK, LIO, LC GNSS-RTK-LIO, 3DLA GNSS-RTK, and 3DLA GNSS-RTK-NE, respectively. The black curve denotes the ground truth (GT) trajectory.

Firstly, compared with loosely-coupled integration through relative pose, the tightly-coupled integration fuses all the raw measurements and is able to separately mitigate the impact of outliers. Secondly but more importantly, the VS measurements make a great contribution to improving the original satellite geometry. The ambiguity fixing rate of 3DLA GNSS-RTK reaches 5.98%, yet the potential NLOS receptions are still not excluded. Therefore, 3DLA GNSS-RTK-NE is performed to further demonstrate the effectiveness of the proposed NLOS exclusion method.

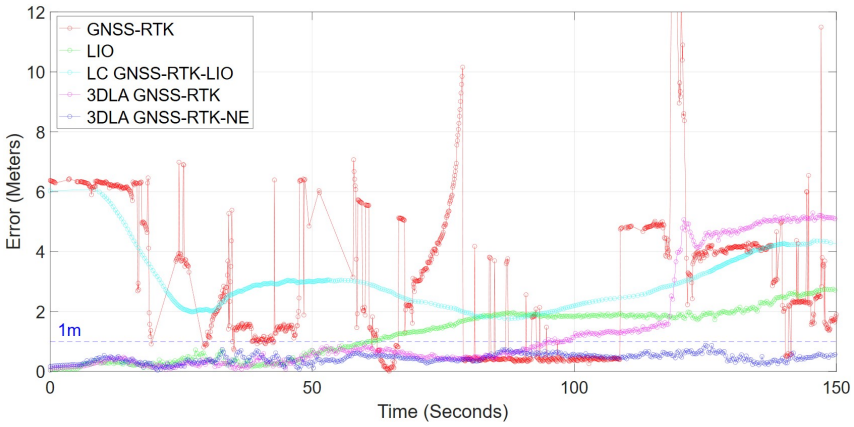

Figure 3.10: 3D positioning error in Urban Canyon 1. The red, green, cyan, magenta and blue curves denote GNSS-RTK, LIO, LC GNSS-RTK-LIO, 3DLA GNSS-RTK, and 3DLA GNSS-RTK-NE, respectively.

3DLA GNSS-RTK-NE eventually shows the best performance with 0.36 meters and 0.44 meters respective 2D and 3D errors, 0.15 meters and 0.87 meters respective 3D standard deviation and 3D maximum error. The ambiguity fixing rate of the whole trajectory by 3DLA GNSS-RTK-NE reaches 11.24%. These two observations demonstrate that the NLOS exclusion and the geometry improvement through the VS can make significant contributions to the final positioning result.

In conclusion, the proposed 3D LiDAR-aided GNSS-RTK/IMU integrated positioning method firstly filters out unhealthy GNSS measurements from potential NLOS receptions based on precisely modeled PCM, and secondly improves the satellite geometry by VS from LiDAR measurements, which leads to better positioning accuracy, higher ambiguity fixing rate, and improved robustness. One should note that the maximum remaining error still reaches 0.87 meters, which can be inferred as caused by multipath receptions, which cannot be detected directly through the PCM. How to infer the uncertainty of the multipath effects from the 3D PCM is also an interesting topic to be investigated which is one of our future directions.

Table 3.2: Positioning performance in Urban Canyon 1. MEAN represents horizontal (2D) and overall (3D) positioning errors in meters. Max represents the maximum positioning errors in meters. STD represents the standard deviation of positioning errors in meters. The improvement (IMPR.) is calculated concerning the MEAN of GNSS-RTK. "Avail." denotes the availability.

All Data	GNSS-RTK	LIO	LC GNSS-RTK-LIO	3DLA GNSS-RTK	3DLA GNSS-RTK-NE
2D MEAN	1.54	**0.32**	1.42	0.39	0.36
2D MAX	18.79	0.97	3.35	0.76	**0.83**
2D STD	1.37	0.23	0.63	0.16	**0.16**
2D IMPR.	-	**79.35%**	8.39%	74.84%	76.77%
3D MEAN	2.96	1.30	3.00	1.53	**0.44**
3D MAX	21.38	2.79	6.07	5.29	**0.87**
3D STD	2.41	0.81	0.88	1.78	**0.15**
3D IMPR.	-	63.28%	15.25%	56.78%	**87.57%**
Ambiguity Fixing Rate	1.43%	-	-	5.98%	**11.24%**
Avail.	88.35%	100%	100%	100%	**100%**

Evaluation of Urban Canyon 2

We further evaluate the proposed system in Urban Canyon 2 to show the effectiveness of the proposed method applied in a more urbanized area. Table. 3.3 demonstrates the results of the compared methods, and Fig. 3.11 and Fig. 3.12 illustrate the 3D trajectory and 3D positioning errors. Urban Canyon 2 is more challenging for positioning compared with Urban Canyon 1 due to more buildings and trees. GNSS-RTK achieves a 1.81 meter 2D mean error and a 3.65 meter 3D mean error. The maximum 3D error reaches 55.59 meters with 5.27 meters as the standard deviation. The overall ambiguity fixing rate is 2.86%. Moreover, compared with GNSS-RTK standalone method, LIO shows a better performance with 1.76 meters of 2D error and 1.97 meters of 3D error. The increasing trend of the LIO positioning error in Fig. 3.12 indicates the accumulated drift. Furthermore, the LC GNSS-RTK-LIO achieves 1.38 meters mean error in the 2D case and 2.77 meters in the 3D case. Although the quality of GNSS-RTK solutions in Urban Canyon 2 is still as low for Urban Canyon 1, LC GNSS-RTK-LIO outperforms LIO because the trajectory is longer and the drift error of LIO is larger. In conclusion, the loose integration between LIO and GNSS-RTK helps to obtain a better positioning result, but the impact of the NLOS

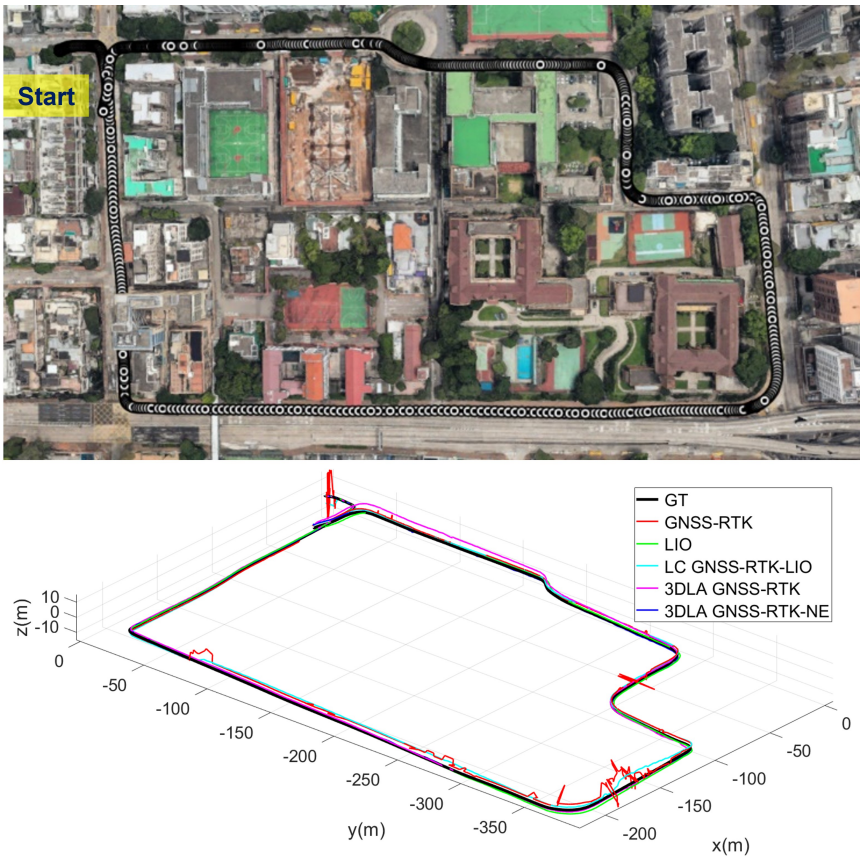

Figure 3.11: The trajectory in Urban Canyon 2. The upper panel shows the projected trajectories on Google Earth. The lower panel shows the 3D trajectories of different methods. The red, green, cyan, magenta and blue curves denote GNSS-RTK, LIO, LC GNSS-RTK-LIO, 3DLA GNSS-RTK, and 3DLA GNSS-RTK-NE, respectively. The black curve denotes the ground truth (GT) trajectory.

receptions and non-ideal geometry distribution are still not compensated.

The geometry problem can be properly tackled by the proposed tightly-coupled VS-aided GNSS-RTK. 3DLA GNSS-RTK shows an increase of 2D mean error as 0.61 meters and an ambiguity fixing rate of 5.64% compared with GNSS-RTK and LIO. However, the 3D mean error reaches 2.02 meters as the remaining NLOS receptions are not excluded. Therefore, 3DLA GNSS-RTK-NE with accurate NLOS exclusion is finally performed and achieves the best accuracy with 2D mean error and 3D mean error decreasing to 0.49 meters and 0.79 meters respectively. Meanwhile, the maximum error and the standard deviation in 2D and 3D cases are 1.44/0.22 meters

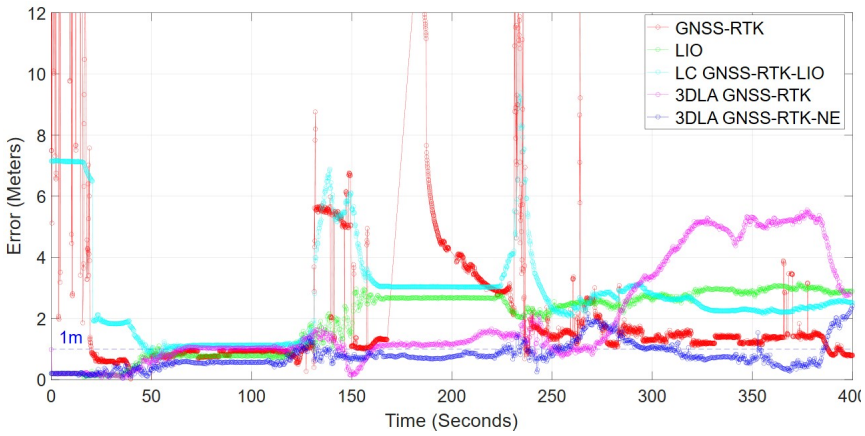

Figure 3.12: 3D positioning error in Urban Canyon 2. The red, green, cyan, magenta and blue curves denote GNSS-RTK, LIO, LC GNSS-RTK-LIO, 3DLA GNSS-RTK, and 3DLA GNSS-RTK-NE, respectively.

Table 3.3: Positioning performance in Urban Canyon 2. MEAN represents horizontal (2D) and overall (3D) positioning errors in meters. Max represents the maximum positioning errors in meters. STD represents the standard deviation of positioning errors in meters. The improvement (IMPR.) is calculated concerning the MEAN of GNSS-RTK. "Avail." denotes the availability.

ALL DATA	GNSS-RTK	LIO	LC GNSS-RTK-LIO	3DLA GNSS-RTK	3DLA GNSS-RTK-NE
2D MEAN	1.81	1.76	1.38	0.61	**0.49**
2D MAX	47.28	3.15	6.74	1.54	**1.44**
2D STD	2.20	0.95	1.21	0.36	**0.22**
2D IMPR.	-	2.76%	23.75%	68.72%	**74.87%**
3D MEAN	3.65	1.97	2.77	2.02	**0.79**
3D MAX	55.59	3.15	9.39	5.55	**2.16**
3D STD	5.27	0.97	1.58	1.70	**0.42**
3D IMPR.	-	46.02%	24.11%	44.65%	**78.36%**
Ambiguity Fixing Rate	2.86%	-	-	5.64%	**7.43%**
Avail.	94.7%	100%	100%	100%	**100%**

and 2.16/0.42 meters. The ambiguity fixing rate of the 3DLA-NE reaches the highest level of all five methods at 7.43%. The evaluation of Urban Canyon 2 further proves the effectiveness of the proposed method of two key contributions as LiDAR-aided NLOS exclusion and geometry improvement.

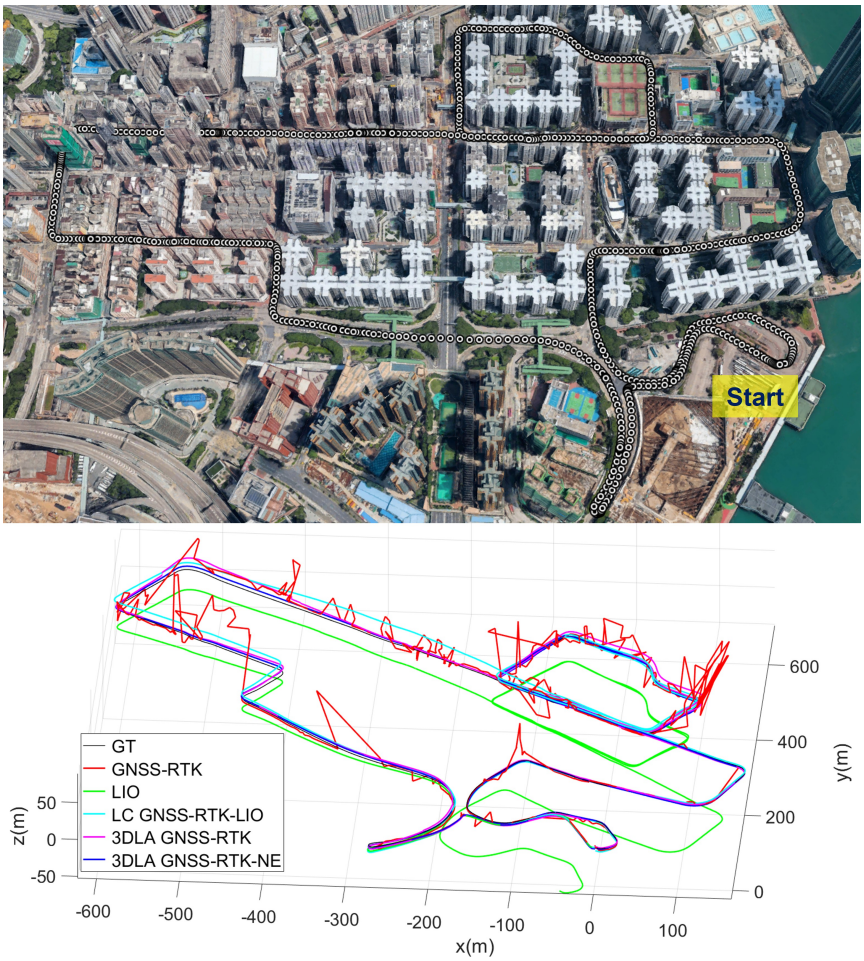

Figure 3.13: The trajectory in Urban Canyon 3. The upper panel shows the projected trajectories on Google Earth. The lower panel shows the 3D trajectories of different methods. The red, green, cyan, magenta and blue curves denote GNSS-RTK, LIO, LC GNSS-RTK-LIO, 3DLA GNSS-RTK, and 3DLA GNSS-RTK-NE, respectively. The black curve denotes the ground truth (GT) trajectory.

Evaluation of Urban Canyon 3

We conducted a further evaluation of the proposed system in Urban Canyon 3, representing a highly urbanized area. Table. 3.4 presents the results of the compared methods, while Fig. 3.13 and Fig. 3.14illustrate the 3D trajectory and 3D positioning error. The GNSS-RTK method achieves a 2D mean error of 5.11 meters and a 3D mean error of 9.90 meters. The maximum 3D error reaches nearly 100 meters, with a standard deviation of 15.67 meters. The overall ambiguity fixing rate is 1.22%.

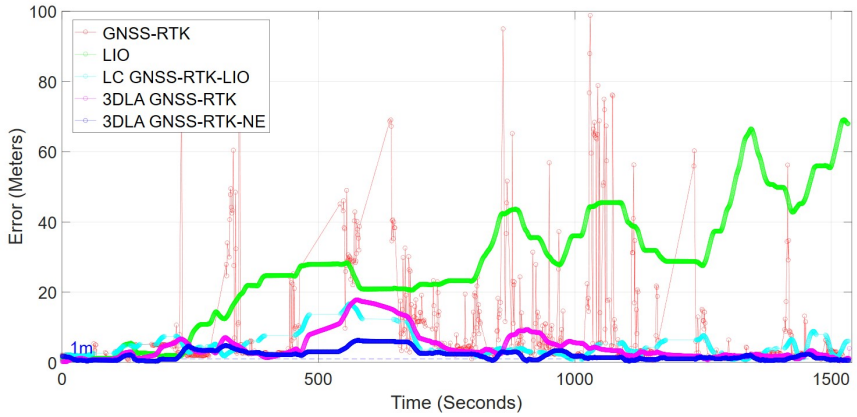

Figure 3.14: 3D positioning error in Urban Canyon 3. The red, green, cyan, magenta and blue curves denote GNSS-RTK, LIO, LC GNSS-RTK-LIO, 3DLA GNSS-RTK, and 3DLA GNSS-RTK-NE, respectively.

Table 3.4: Positioning performance in Urban Canyon 3. MEAN represents horizontal (2D) and overall (3D) positioning errors in meters. Max represents the maximum positioning errors in meters. STD represents the standard deviation of positioning errors in meters. The improvement (IMPR.) is calculated concerning the MEAN of GNSS-RTK. "Avail." denotes the availability.

ALL DATA	GNSS-RTK	LIO	LC GNSS-RTK-LIO	3DLA GNSS-RTK	3DLA GNSS-RTK-NE
2D MEAN	5.11	12.63	2.67	2.08	**1.02**
2D MAX	45.38	45.51	7.89	6.70	**2.57**
2D STD	7.75	12.56	1.80	1.54	**0.52**
2D IMPR.	-	-	47.75%	59.29%	**80.04%**
3D MEAN	9.90	28.37	4.41	4.54	**2.13**
3D MAX	98.85	69.07	16.68	17.77	**6.27**
3D STD	15.67	16.94	3.34	4.09	**1.50**
3D IMPR.	-	-	55.44%	54.14%	**78.48%**
Ambiguity Fixing Rate	1.22%	-	-	1.26%	**8.72%**
Avail.	60.11%	100%	100%	100%	**100%**

The LIO method shows a 2D error of 12.63 meters and a 3D error of 28.37 meters due to significant trajectory drift. The LC GNSS-RTK-LIO method achieves a mean error of 2.67 meters in the 2D case and 4.41 meters in the 3D case, and the maximum 3D positioning error reaches 16.68 meters, which is better than the GNSS-RTK or LIO methods, however, the margin of the error is still relatively large. When tightly-coupled integration is adopted, only limited improvement in 2D positioning accuracy is obtained. The improvement in the ambiguity fixing rate is also minimal reaching 1.26%. A large 3D positioning error is observed around 570s and 890s

in Fig. 3.14, where the presence of double-decker buses and dense buildings in the surrounding area results in a significant amount of reflected signal receptions. Finally, the 3DLA GNSS-RTK-NE method is performed with NLOS exclusion, achieving the best accuracy with a 2D mean error of 1.02 meters and a 3D mean error of 2.13 meters. The maximum error and standard deviation in the 2D and 3D cases are 2.57/0.52 meters and 6.27/1.50 meters, respectively. The ambiguity fixing rate of the 3DLA-NE method reaches the highest level at 8.72%. The evaluation of Urban Canyon 3 highlights the significance of accurate and reliable NLOS mitigation for long-term system stability, particularly in densely populated urban areas. LiDAR observations often face degradation when encountering a large number of dynamic objects or traversing featureless regions (such as the 250s and 900s intervals). If both the geometry distribution of LiDAR observations and GNSS observations are poor, the estimation accuracy of the system will inevitably degrade.

3.3.5 Running efficiency of the proposed method

Computational efficiency is crucial for real-time positioning systems. The time performance of the proposed system is now analyzed. The testing device is equipped with an i9-12900K CPU and 32 GB of memory, and the proposed system is operated based on a single-core, single-thread execution. It is worth mentioning that we also provide the runtime of the system based on different numbers of LiDAR observations. Fig. 3.15 illustrates the computational consumption, where we divide the total runtime into three parts: preprocessing, optimization, and AR. The preprocessing stage includes sensor data processing, NLOS detection, and constructing the factor graph. For different numbers of LiDAR observations, this step takes a relatively similar amount of time. It can be further observed that the optimization process consistently consumes the most time, followed by AR. Additionally, as the number of LiDAR observations increases, the time required for optimization rapidly

extends. This is because multi-sensor tightly-coupled optimization is a non-convex optimization problem, and the solving efficiency is influenced by the consistency of sensor observations and the system complexity. Increasing the number of observations raises the system complexity, thereby reducing the efficiency of solving this optimization problem. The time usage of AR demonstrates a slower upward trend with more LiDAR observations, where the most time-consuming part is the estimation of the variance-covariance matrix. Different from optimization, the estimation efficiency of the variance-covariance matrix is primarily related to the state size, as the proposed system calculates it by taking the inverse of the Hessian matrix approximated by the Jacobian matrix. Computing the inverse of larger matrices requires more time. In our implementation, the sliding-window size is consistently set to 5 to ensure the efficiency of AR. Overall, using 1200 or more observations would result in a runtime exceeding 500 ms, which is not applicable for real-time positioning. However, with an average runtime of around 70 ms using 200 observations, it meets real-time requirements and is conducive to practical applications that require integration with other systems.

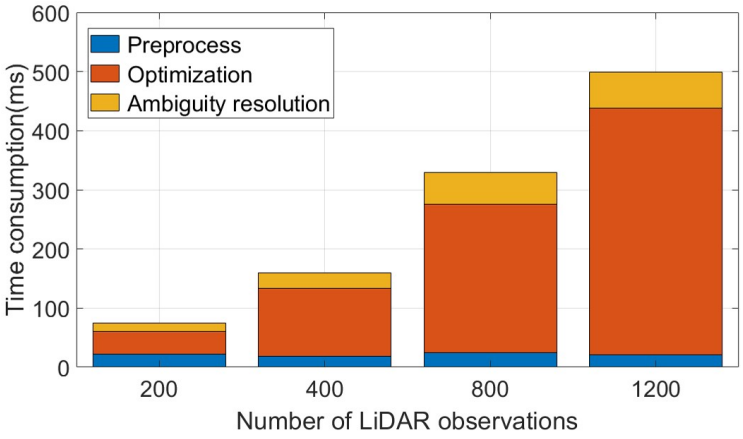

Figure 3.15: Illustration of time consumption of the proposed system with different numbers of LiDAR observations. The total runtime is divided into three parts, namely preprocessing, optimization, and ambiguity resolution.

3.4 Conclusion

GNSS-RTK can provide reliable accurate positioning results in the opening areas, yet will suffer from NLOS receptions and poor satellite distribution in urban canyons. This chapter presents 3D LiDAR-aided GNSS-RTK positioning that: (1) performs NLOS detection and exclusion based on the drift-free 3D PCM to eliminate the impact of unhealthy GNSS measurements, and (2) improves the satellite geometry distribution with great efficiency through selected low-lying VS provided by LiDAR landmarks. We evaluate the proposed system in three challenging sequences in Hong Kong. The result shows that the proposed system can achieve real-time positioning capability with higher accuracy and robustness in a highly urbanized area using commercial-level GNSS receivers and LiDAR/IMU sensor kit.

Chapter 4

Tightly-Coupled GNSS/LiDAR/IMU Integration with Global Optimization Consistency

4.1 Introduction

As we discussed in Chapter 2, optimization-based tightly coupled integration of GNSS, LiDAR, and IMU offers a powerful framework for fusing raw measurements while accounting for their temporal and spatial correlations, thereby enabling high-precision and robust state estimation in challenging urban environments. However, existing solutions have yet to fully realize this potential. In particular, current state-of-the-art methods rarely incorporate both pseudorange and Doppler GNSS measurements into a joint FGO framework alongside LIO. Moreover, many existing GNSS/LiDAR/IMU fusion systems rely on scan-to-map registration schemes for LiDAR constraints [26; 31; 91], which act as absolute pose priors. Such methods are inherently susceptible to drift: when accumulated LiDAR drift is present, the LiDAR constraints themselves become inconsistent, and this inconsistency propagates to the fused solution, degrading global accuracy. Consequently, the fusion often fails to produce globally consistent and drift-free state estimates across sensors. These limi-

tations point to a critical need for a tightly-coupled GNSS/LiDAR/IMU framework that not only leverages raw multi-sensor data, but also maintains internal consistency through globally optimized estimation. To relax the listed two limitations above, this chapter introduces GLIO—a globally consistent, tightly-coupled GNSS/LiDAR/imu integration framework designed to provide continuous and drift-free state estimation for intelligent vehicles operating in urban areas. Specifically, the contributions are listed as:

(1) Raw measurements level GNSS/LiDAR/IMU tightly-coupled integration with FGO: A tightly-coupled integration scheme fusing GNSS pseudorange, Doppler measurements, LiDAR measurements, and IMU measurements through factor graph optimization.

(2) Robust and globally consistent state estimation: A two-stage optimization-based estimator is proposed to improve robustness to unhealthy GNSS measurements and maintain the global consistency of the estimation.

(3) Open-sourced code and extensive experimentation in challenging scenarios: The proposed method has been demonstrated through experimentation in various challenging urban scenarios in Hong Kong. To contribute to the community, the implementation of the proposed method is also open-sourced by https://github.com/XikunLiu-huskit/GLIO.

To the best of our knowledge, this is the first attempt to integrate GNSS, LiDAR, and IMU all at raw measurement levels based on factor graph optimization together with open-sourced implementation.

4.2 Methodology

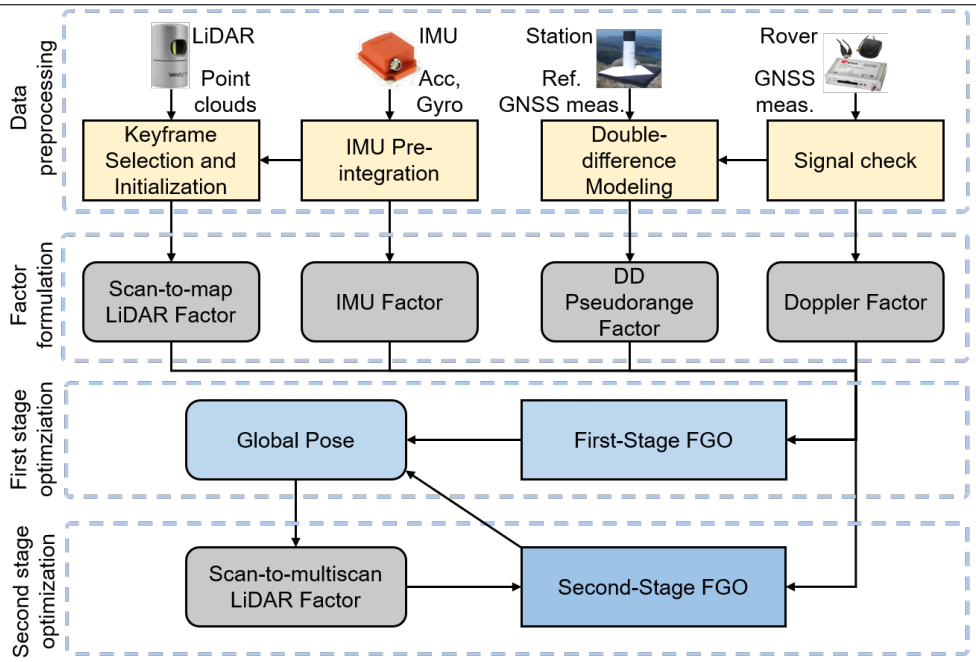

Figure 4.1: The overview of the system pipeline.

4.2.1 System Overview

The workflow of the proposed system is illustrated in Fig. 4.1, It comprises four main steps, which are the data preprocessing, the factor formulation, the sliding-window-based first stage optimization, and the batch-optimization-based second stage fusion. The system's inputs consist of GNSS measurements (including raw pseudorange and Doppler measurements), LiDAR measurements, and IMU measurements. To manage computational load, the proposed system utilizes a keyframe mode for processing measurements. The pre-integration method [96] is implemented to convert raw IMU measurements into relative constraints and propagate the initial pose of keyframes.

Subsequently, a first stage sliding-window-based factor graph is formulated, which includes a double-differenced (DD) pseudorange factor, Doppler factor, scan-to-map LiDAR factor, and IMU pre-integration factor. Once the preprocessing is completed, the states are optimized using factor graph optimization (FGO) in a joint manner. Moreover, the second stage batch optimization is performed at a certain time interval.

For batch fusion, a large factor graph is maintained with similar GNSS and IMU constraints. Notably, the LiDAR factor is formulated as a scan-to-multi-scan scheme to avoid local minimum and maintain global consistency.

The states are maintained as IMU-centric body frame in the ENU coordinate. The following are the states in detail:

(a) The k^{th} keyframe's pose states, including the position $\mathbf{p}_{b,k}^{EN}$ and orientation $\mathbf{q}_{b,k}^{EN}$.

(b) The k^{th} keyframe's velocity $\mathbf{v}_{b,k}^{EN}$. Additionally, $\mathbf{b}_a$ denotes the bias of the accelerometer and $\mathbf{b}_w$ represents the bias of the gyroscope.

(c) The receiver clock drift $\delta_{r,t}^{r}$.

The states can be further expressed as:

$$\mathcal{X} = \left[\mathbf{x}_0, \cdots, \mathbf{x}_k, \delta_{t_0}^{r}, \cdots, \delta_{t_{n-1}}^{r}\right] \tag{4.1}$$

$$\mathbf{x}_k = \left[\mathbf{p}_{b,k}^{EN}, \mathbf{q}_{b,k}^{EN}, \mathbf{v}_{b,k}^{EN}, \mathbf{b}_a, \mathbf{b}_w\right]$$

where $t \in [t_0, \cdots, t_{n-1}]$ denotes the GNSS epoch, while n denotes the received GNSS total epochs within the sliding window.

The optimal state estimation is determined by maximizing the posterior probability of the given measurements. Assuming that the measurements are uncorrelated and the corresponding noise follows a zero-mean Gaussian distribution, the problem can be transferred to:

$$\begin{aligned}\mathcal{X}^* = \arg\min_{\mathcal{X}} \sum_{S,r,k,t} \Big(&\|\mathbf{r}_p - \mathbf{H}_p\mathcal{X}\| + \|\mathbf{r}_{L,k}\|_{\Sigma_L}^2 + \|\mathbf{r}_{B,k}\|_{\Sigma_B}^2 \\ &+ \|\mathbf{r}_{DD,\rho,r,t}^{S}\|_{\sigma_\rho}^2 + \|\mathbf{r}_{d,r,t}^{S}\|_{\sigma_d}^2 \Big)\end{aligned} \tag{4.2}$$

where the marginalized term as prior constraints is denoted by $\{\mathbf{r}_p, \mathbf{H}_p\}$. The IMU factor is represented by $\mathbf{r}_{B,k}$, with a weighting scheme according to the covariance matrix $\mathbf{\Sigma}_B$. Similarly, the LiDAR factor is represented by $\mathbf{r}_{L,k}$ and is accordingly weighted by its relative covariance matrix $\mathbf{\Sigma}_L$. The GNSS pseudorange and Doppler factors are denoted by $\mathbf{r}^S_{DD,\rho,r,t}$ and $\mathbf{r}^S_{d,r,t}$, respectively. The corresponding uncertainty of Doppler measurements is specifically set for ten times smaller than pseudorange measurements as $10 \cdot \sigma_d = \sigma_\rho$, where the initial calculation of σ_ρ is based on the SNR and elevation angle from [99].

4.2.2 Factor Formulation

In this section, the modeling and the factor formulation of the sensors are introduced, including DD pseudorange factor, the Doppler factor, the LiDAR factor, and the IMU pre-integration factor.

GNSS DD Pseudorange Factor

The pseudorange observation function is given by [108]:

$$\rho^s_{r,t} = r^s_{r,t} + c\left(\delta_{r,t} - \delta_{s,t}\right) + I^s_{r,t} + T^s_{r,t} + \varepsilon^s_{\rho,r,t} \tag{4.3}$$

where $\rho^s_{r,t}$ denotes the received pseudorange measurement by receiver r from satellite s at epoch t. The real geometric range is given by $r^s_{r,t}$. The ionospheric delay and the tropospheric delay are represented by $I^s_{r,t}$ and $T^s_{r,t}$, respectively. The rest errors, including the error arising from NLOS or multipath receptions, receiver, and antenna-related noise errors are represented by $\varepsilon^s_{\rho,r,t}$.

To prevent the system from introducing gross errors caused by clock synchronization problems or the atmosphere delay, we adopt the DD technique [108] by performing single-difference twice between receivers (user receiver r and reference station e) and between satellites (satellite s and master satellite w). The satellite

with the highest elevation angle in the corresponding epoch is selected as the master satellite, which is less prone to multipath and NLOS receptions. The DD pseudorange measurement is given by [108]:

$$\rho^s_{\mathrm{DD},r,t} = (\rho^s_{r,t} - \rho^s_{e,t}) - (\rho^w_{r,t} - \rho^w_{e,t}) \tag{4.4}$$

With other error sources being eliminated, the DD pseudorange prediction model can be further derived as:

$$\rho^s_{\mathrm{DD},r,t} = (r^s_{r,t} - r^s_{e,t}) - (r^w_{r,t} - r^w_{e,t}) + \varepsilon^s_{\mathrm{DD},\rho,r,t} \tag{4.5}$$

where $\varepsilon^s_{\mathrm{DD},\rho,r,t}$ represents the noise error term and the residual is given as:

$$r^s_{\mathrm{DD},\rho,r,t} = \rho^s_{\mathrm{DD},r,t} - (r^s_{r,t} - r^s_{e,t}) - (r^w_{r,t} - r^w_{e,t}) \tag{4.6}$$

where the range distances $r^s_{r,t}$, $r^s_{e,t}$, $r^w_{r,t}$ and $r^w_{e,t}$ are the distance from receiver r and base station e to satellite s and w at epoch t, which are calculated based on their ECEF positions. As the states are maintained in the ENU frame, to calculate the residual, we convert the receiver position at epoch t in the ENU frame $\mathbf{p}^{EN}_{r,t}$ to ECEF frame $\mathbf{p}^{EC}_{r,t}$ through the following equations:

$$\mathbf{p}^{EC}_{r,t} = \mathbf{R}^{EC}_{EN}\mathbf{p}^{EN}_{r,t} + \mathbf{p}^{EC}_0 \tag{4.7}$$

$$\mathbf{R}^{EC}_{EN} = \begin{bmatrix} -\sin\lambda_0 & -\sin\phi_0\cos\lambda_0 & \cos\phi_0\cos\lambda_0 \\ \cos\lambda_0 & -\sin\phi_0\sin\lambda_0 & \cos\phi_0\sin\lambda_0 \\ 0 & \cos\phi_0 & \sin\phi_0 \end{bmatrix} \tag{4.8}$$

where the ECEF origin point is denoted as $\mathbf{p}^{EC}_0$, which can be obtained through various initialization methods, such as trajectory alignment between locally generated trajectory (e.g., by LIO) and globally generated trajectory (e.g., by GNSS). The geographic longitude ϕ_0 and geographic latitude λ_0 are directly calculated from the ECEF origin point $\mathbf{p}^{EC}_0$.

The lever-arm transformation from an IMU-centered position $\mathbf{p}_{b,t}^{EN}$ to receiver position $\mathbf{p}_{r,t}^{EN}$ is obtained through extrinsic parameters:

$$\mathbf{p}_{r,t}^{EN} = \mathbf{p}_{b,t}^{EN} + \mathbf{R}_{r,t}^{EN}\mathbf{p}_{r}^{b} \tag{4.9}$$

where $\mathbf{p}_{r}^{b}$ is lever-arm translation.

Notably, the timestamp of the LiDAR keyframe t_k is different from GNSS epoch time t. We use the interpolation method to align GNSS measurements to LiDAR timestamps. Given the LiDAR keyframe-related states $\mathbf{p}_{b,k}^{EN}$ and $\mathbf{p}_{b,k+1}^{EN}$ in the adjacent moment t_k and t_{k+1} with $t \in [t_k, t_{k+1}]$, the GNSS epoch-related state $\mathbf{p}_{b,t}^{EN}$ can be calculated as:

$$\mathbf{p}_{b,t}^{EN} = \left\{ \frac{t - t_k}{t_{k+1} - t_k}\mathbf{p}_{b,k}^{EN} + \frac{t_{k+1} - t}{t_{k+1} - t_k}\mathbf{p}_{b,k+1}^{EN} \right\} \tag{4.10}$$

GNSS Doppler Factor

The Doppler observation function is given by [108]:

$$\lambda d_{r,t}^{s} = \mathbf{e}_{r,t}^{s,\mathrm{LOS}} \left(\mathbf{v}_{s,t}^{EC} - \mathbf{v}_{r,t}^{EC} \right) + c \left(\delta_{r,t}^{i} - \delta_{s,t}^{i} \right) + \zeta_{r,t}^{s} \tag{4.11}$$

where $\zeta_{r,t}^{s}$ denotes the noisy error term, c represents the speed of light, while λ is the carrier wavelength of the signal. The receiver velocity in the ECEF frame is obtained from the states in the ENU frame by:

$$\mathbf{v}_{r,t}^{EC} = \mathbf{R}_{EN}^{EC}\mathbf{v}_{r,t}^{EN}.$$

$\mathbf{e}_{r,t}^{s,\mathrm{LOS}}$ is the line-of-sight unit vector, which points the satellite from the receiver. It is calculated by:

$$\mathbf{e}_{r,t}^{s,\mathrm{LOS}} = \left(\frac{\mathbf{p}_{s,t}^{EC} - \mathbf{p}_{r,t}^{EC}}{\| \mathbf{p}_{s,t}^{EC} - \mathbf{p}_{r,t}^{EC} \|} \right)^{\top} \tag{4.12}$$

Therefore, the residual of Doppler measurement is given by:

$$r_{d,r,t}^{s} = d_{r,t}^{s} - \frac{1}{\lambda_i} \left(\mathbf{e}_{r,t}^{s,\mathrm{LOS}} \left(\mathbf{v}_{s,t}^{EC} - \mathbf{v}_{r,t}^{EC} \right) + c(\delta_{r,t}^{i} - \delta_{s,t}^{i}) \right) \tag{4.13}$$

Inertial Factor

The inertial sensor provides acceleration and angular velocity observations, which are affected by bias and additive noises. In comparison to other perception and positioning sensors like LiDAR and GNSS, its higher measurement frequency leads to the development of pre-integration method and wide utilization of the corresponding method for efficient sensor fusion [96]. The method pre-integrates multiple raw measurements to establish a relative pose constraint from keyframe k to its next adjacent keyframe $k+1$. The implementation of IMU pre-integration follows [10], the relevant theories are omitted here and interested readers can refer to [96; 10] for more information in detail.

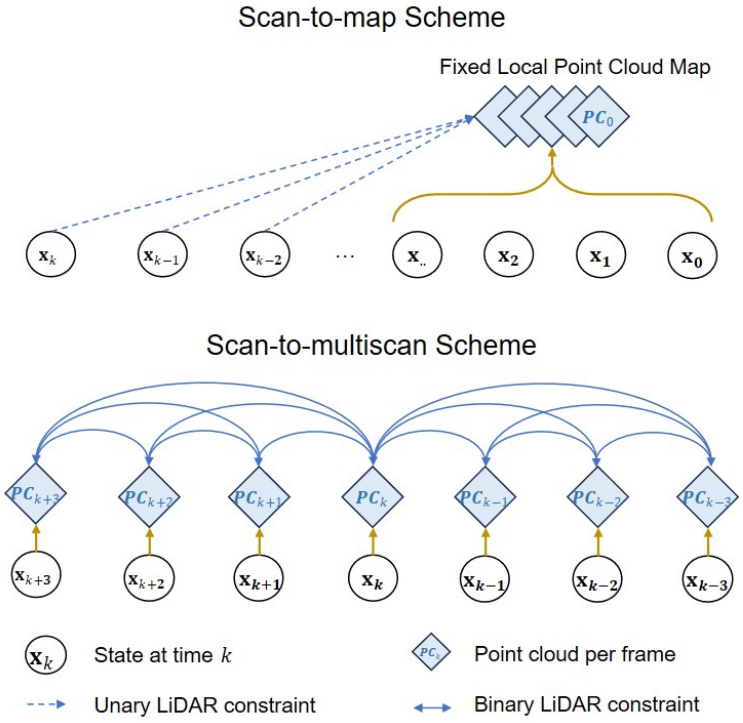

Figure 4.2: The illustration of the scan-to-map vs scan-to-multi-scan association for LiDAR factor formulation.

LiDAR Factor of Scan-to-map Model

In this work, LiDAR measurements are utilized in a manner similar to that of popular feature-based LiDAR SLAM methods [11]. The so-called scan-to-map scheme data association for the LiDAR factor is depicted in Fig. 4.2. By evaluating the performance using edge-feature and plane-feature for LiDAR odometry, it is observed that the planar features provide better performance for better robustness and higher accuracy. Therefore, planar points are utilized in the implementation and the edge points are not involved. To select planar feature points, we extract local patches to evaluate their local distribution, the points satisfying the planar distribution are selected. Then, to identify plane correspondences, the nearest-neighbor search method is adopted between the source point clouds and the target point cloud, which are from keyframes and local map. Additionally, we analyze the eigenvalue of each feature patch to verify the plane correspondences.

Finally, the point-to-plane scan-to-map residual is computed based on the feature point $\mathbf{p}_{p,k}^{EN}$ in keyframe k, and the corresponding feature points $\mathbf{p}_{p,k,a}^{EN,M}$, $\mathbf{p}_{p,k,b}^{EN,M}$, and $\mathbf{p}_{p,k,c}^{EN,M}$, which represent the planar patch in the local point cloud map M [11]:

$$r_{l,s,k}^{s\text{-}mp} = \frac{\left\| \left(\mathbf{p}_{p,k}^{EN} - \mathbf{p}_{p,k,a}^{EN,M} \right) \cdot \left(\left(\mathbf{p}_{p,k,a}^{EN,M} - \mathbf{p}_{p,k,b}^{EN,M} \right) \times \left(\mathbf{p}_{p,k,a}^{EN,M} - \mathbf{p}_{p,k,c}^{EN,M} \right) \right) \right\|}{\left\| \left(\mathbf{p}_{p,k,a}^{EN,M} - \mathbf{p}_{p,k,b}^{EN,M} \right) \times \left(\mathbf{p}_{p,k,a}^{EN,M} - \mathbf{p}_{p,k,c}^{EN,M} \right) \right\|} \tag{4.14}$$

$$\mathbf{p}_{p,k}^{EN} = \mathbf{R}_{b,k}^{EN} \left(\mathbf{R}_{l}^{b} \mathbf{p}_{p,k}^{l} + \mathbf{p}_{l}^{b} \right) + \mathbf{p}_{b,k}^{EN} \tag{4.15}$$

where the planar point in the local sensor frame is represented by $\mathbf{p}_{p,k}^{l}$. It is transformed from the LiDAR frame to the IMU frame through $\mathbf{T}_{l}^{b} = \begin{bmatrix} \mathbf{R}_{l}^{b} & \mathbf{p}_{l}^{b} \end{bmatrix}$. Then the feature point is further transformed from the body frame to the ENU frame by $\mathbf{T}_{b,k}^{EN} = \left[\mathbf{R}_{b,k}^{EN}, \mathbf{p}_{b,k}^{EN} \right]$.

LiDAR Factor of Scan-to-multi-scan Model

As we have discussed above, since the local point cloud map is fixed, the scan-to-map-based LiDAR constraint essentially can be regarded as an absolute constraint without global positioning information. This approach is problematic for large-scale integration as drift-free alignment between local coordinate and global coordinate cannot be guaranteed. Therefore, we proposed to use scan-to-multi-scan LiDAR factor for tight integration with global constraints, which is illustrated in Fig. 4.2. For each keyframe k, the adjacent m keyframes are associated to provide only on relative pose but correct constraints, where the same plane residual formulation model is adopted and the pose states of both corresponding target and source keyframes are involved. In detail, the residual is formed as:

$$r_{l,s,k}^{s\text{-}ms} = \frac{\left\| \left(\mathbf{p}_{p,k}^{EN} - \mathbf{p}_{p,k+i,a}^{EN}\right) \cdot \left[\left(\mathbf{p}_{p,k+i,a}^{EN} - \mathbf{p}_{p,k+i,b}^{EN}\right) \times \left(\mathbf{p}_{p,k+i,a}^{EN} - \mathbf{p}_{p,k+i,c}^{EN}\right) \right] \right\|}{\left\| \left(\mathbf{p}_{p,k+i,a}^{EN} - \mathbf{p}_{p,k+i,b}^{EN}\right) \times \left(\mathbf{p}_{p,k+i,a}^{EN} - \mathbf{p}_{p,k+i,c}^{EN}\right) \right\|} \tag{4.16}$$

$$\mathbf{p}_{p,k}^{EN} = \mathbf{R}_{b,k}^{EN} \left(\mathbf{R}_{l}^{b} \mathbf{p}_{p,k}^{l} + \mathbf{p}_{l}^{b}\right) + \mathbf{p}_{b,k}^{EN} \tag{4.17}$$

$$\mathbf{p}_{p,k+i,abc}^{EN} = \mathbf{R}_{b,k+i}^{EN} \left(\mathbf{R}_{l}^{b} \mathbf{p}_{p,k+i,abc}^{l} + \mathbf{p}_{l}^{b}\right) + \mathbf{p}_{b,k+i,abc}^{EN} \tag{4.18}$$

where $i \in [-m, m]$.

The proposed scan-to-multi-scan LiDAR factor brings two advantages. On the one hand, it provides relative constraints only, which enables consistent integration between global GNSS and local LiDAR. On the other hand, the scan-to-multi-scan association between multiple keyframes enhances the relative pose information and thus increases the weight during optimization, which contributes to a smoother local trajectory and better robustness to outliers from other sensors.

Marginalization Factor

To reduce computational complexity while retaining the impact of previous information constraints, we adopt marginalization in the sliding-window-based optimization process in the first stage fusion. This involves gradually marginalizing constraints from previous keyframes using the Schur complement method [102]. After marginalizing the constraints from older keyframes, a new prior factor is added to the updated window.

4.2.3 Factor Graph Construction on the First Stage and the Second Stage Fusion

The factor graph of two stages optimization is shown in Fig. 4.3. We design sliding-window-based first stage fusion and batch-optimization-based second stage fusion separately. The main difference between the first and the second stage lies in the formulation of the LiDAR factor. For the first stage, the factor graph is formulated in a short sliding window to provide an efficient estimation. Within the short time window, the GNSS measurements are limited and prone to outliers. Differently, the LiDAR measurements can maintain high accuracy over a short period. Therefore, the LiDAR factor is employed based on a scan-to-map scheme, where the local map is built through previous keyframe states as high-quality prior information. In this way, the GNSS measurements can assist LIO for reliable position and velocity estimation in highly dynamic environments. To ensure a balanced impact of GNSS, LiDAR, and IMU during optimization, we limit the number of LiDAR features to 100 for each keyframe by random selection, and the LiDAR residuals are dynamically weighted based on the number ratio between LiDAR and GNSS measurements [33].

On the other side, we follow our previous work in [33] and proposed to fuse the GNSS factor, IMU factor, with the scan-to-multi-scan LiDAR factor for the second stage optimization. Notably, the second stage batch optimization uses a

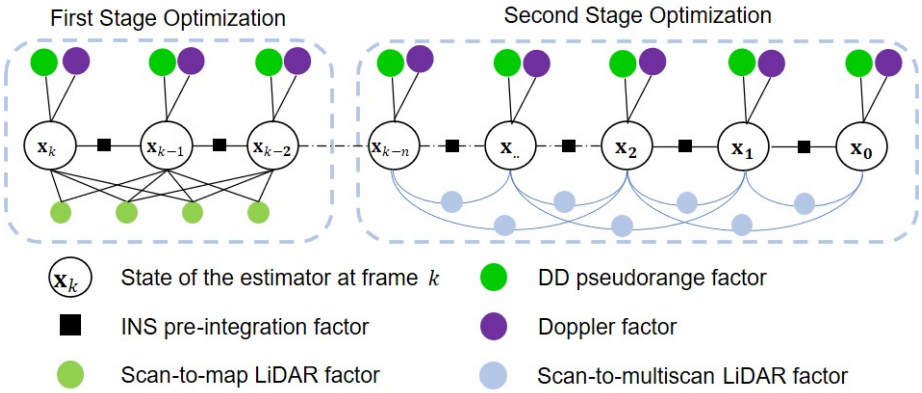

Figure 4.3: The illustration of the factor graph structure of the proposed first stage fusion and second stage optimization.

sufficient number of GNSS measurements over a long period, and together with the strong relative pose constraints from LiDAR and IMU, the globally consistent and locally robust optimization is achieved. Specifically, each LiDAR keyframe is associated with 12 adjacent keyframes, for each frame pair, only 25 planar features are randomly selected to decrease the computational load and balance the weight between different factors. Moreover, the second stage batch optimization is iterated 3 times for residual-based outlier detection and exclusion [3]. The second stage fusion is performed in another thread and updates the global states once finishing the optimization.

4.3 Experimental Results

In this work, we implement the proposed system through C++ on Robot Operation System (ROS) [103]. Ceres Solver [104] is utilized to solve the nonlinear optimization problem. To evaluate the performance, we conduct experiments on challenging sequences from the *UrbanNav* dataset [106]. The sequences can represent typical urban canyons, which pose significant challenges to GNSS receptions due to densely distributed tall blockages.

In the first evaluated sequence, denoted as *TST*, the vehicle started underneath

an overpass and passed through a commercial area densely occupied by tall office buildings, and the road was always accompanied by heavy traffic. The overall narrowness of the roadway makes the sky visibility area limited at most times. A small portion of the trajectory has a one-sided distribution of tall buildings, which will help to mitigate the consistently unhealthy GNSS signal. For the second sequence, named *Whampoa*, the data lasts for more than 25 min and 4.5 km. Vehicle departed from the open sky area and passed through dense urban areas in Hong Kong, involving dense buildings, small tunnels, and busy traffic-related environments. The tunnel environments and the narrow residential road environments make it difficult for GNSS to provide healthy measurements. In addition, the vehicle is often surrounded by multiple double-deckers, which severely affects both GNSS and LiDAR observations. This poses a serious challenge to the positioning capability of the system.

4.3.1 Experiment Platform

The *UrbanNav* experimental platform includes multiple sensors. In this work, the u-blox F9P as a low-cost GNSS receiver is used to collect raw single-frequency GPS/BeiDou/Galileo/GLONASS signals at a rate of 10 Hz. Inertial measurements are collected at 100 Hz using the Xsens Ti-10 IMU, and HDL-32E is obtained point cloud at 10 Hz. To provide ground truth, we utilize the NovAtel SPAN-CPT, which performs multiple frequencies and constellations GNSS Real-time kinematic (RTK) with a tactical IMU. The trajectory is further post-processed to ensure the centimeter-level accuracy. Besides, the extrinsic parameters are priorly calibrated for use.

4.3.2 Evaluation Comparison

The proposed method is evaluated by conducting a qualitative and quantitative comparison with several other representative methods based on multiple aspects. To

evaluate the positioning accuracy of different methods, three aspects of error in terms of mean, maximum, and standard deviation in 2D and 3D cases are compared. The methods we evaluate are listed as:

1. **RTK:** RTKLIB [108] is first evaluated to demonstrate the performance of the conventional GNSS-RTK method. All GNSS measurements are involved, including pseudorange, carrier phase, and Doppler measurements. In detail, forward and backward filtering is set with fix and hold function.

2. **LIO:** As one of the representative LIO systems as well as part of the basis for the proposed system, LILI-OM [30] is evaluated for comparison. The alignment of the local frame to the world frame is given by the ground truth.

3. **LIO-GNSS:** As the state-of-the-art GNSS/LiDAR/IMU fusion method, LIO-SAM [28] is evaluated with differential GNSS (DGNSS) result from RTKLIB [108].

4. **GLIO-SS:** The proposed tightly-coupled GNSS/LiDAR/IMU integrated system with only the single stage optimization implemented. This is to show the effectiveness of the fusion of GNSS, IMU, and scan-to-map LiDAR factors.

5. **GLIO-DS:** The proposed tightly-coupled GNSS/LiDAR/IMU integrated system with both first and second stages optimization. This is to show the effectiveness of the integration of GNSS, IMU, and scan-to-multi-scan LiDAR factors and the final performance of the proposed method.

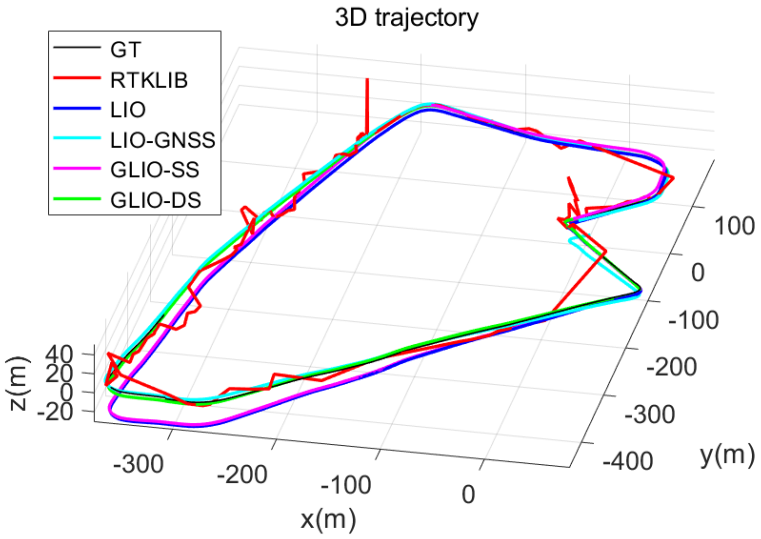

Figure 4.4: 3D trajectory in TST. The black, red, blue, cyan, magenta, and green curves denote the trajectory of ground truth, RTKLIB, LIO, LIO-GNSS, GLIO-SS, and GLIO-DS, respectively.

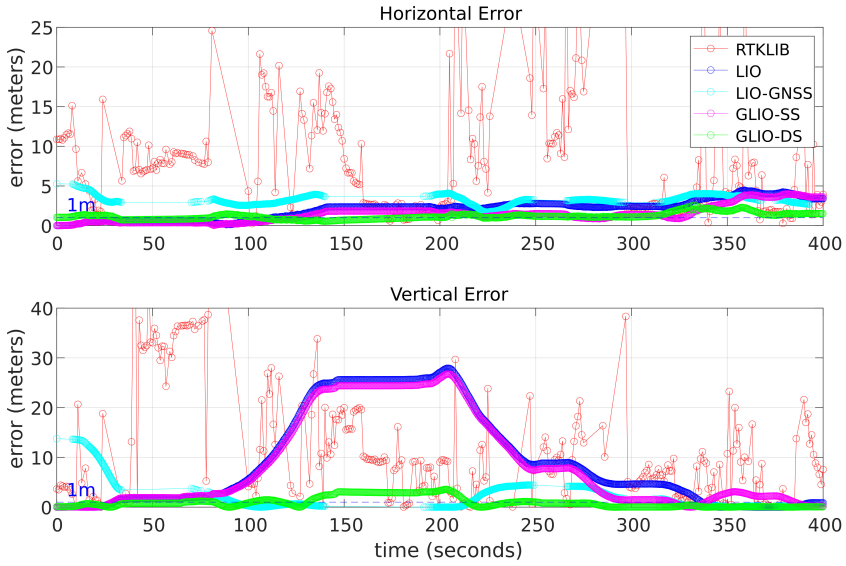

Figure 4.5: Positioning error in TST. The red, blue, cyan, magenta, and green curves denote the error of RTKLIB, LIO, LIO-GNSS, GLIO-SS, and GLIO-DS, respectively.

Evaluation of Data TST

The first experiment is conducted in the medium urban environment of Hong Kong. Table. 4.1 shows the evaluation results of each method, where **MEAN** denotes the positioning error in meters, **MAX** denotes the maximum error in the trajectory, and **STD** denotes the standard deviation. **FIX** represents the fix rate of GNSS-RTK provided by RTKLIB. Fig. 4.4 and Fig. 4.5 depict the trajectory and the positioning errors. Notably, the initial state is provided by ground truth for LIO and GNSS-SS method for coordinate alignment. There are tens of meters of jumps in the error of the RTKLIB throughout the traveling interval. They are due to uninterrupted tall buildings, frequent overpasses, and billboards, as well as interference from surrounding dynamic objects. It is observed that the RTKLIB only achieves a 7.1% fix rate, which indicates the degree of deterioration of the quality of GNSS signal in urban areas. The RTKLIB only resulted in a 2D mean error of 7.53 meters with a maximum error of 46.27 meters, and a 3D mean error of 18.02 meters with a maximum error of 93.69 meters. The LIO method achieved a 2D mean error of 2.21 meters. Due to the short length of the trajectory, the overall 2D accuracy of LIO is less affected by drift. However, the tendency of the trajectory to drift is still clearly evident.

The LIO-GNSS achieves a 2D mean error of 3.24 meters and a 3D mean error of 5.28 meters. Compared with LIO, the LIO-GNSS significantly reduced the 3D mean error through loosely-coupled pose graph optimization (PGO). However, the LIO-GNSS fails to achieve consistent result in the TST sequence. The maximum error reaches 5.26 meters in 2D and 19.01 meters in 3D. Fig. 4.5 shows that there is a large error margin within the first 50 seconds. The reasons are for two aspects: (1) The TST sequence starts from a highly urbanized area, where the filter-based DGNSS by RTKLIB fails to obtain reliable accuracy and covariance of the estimated

Table 4.1: The evaluated positioning error of the four methods in TST. MEAN represents the mean positioning errors in meters. Max represents the maximum positioning errors in meters. STD represents the standard deviation of positioning errors in meters. FIX denotes the GNSS-RTK fix rate.

ALL DATA	RTKLIB	LIO	LIO-GNSS	GLIO-SS	GLIO-DS
2D MEAN	7.53	2.21	3.24	1.53	**1.21**
2D MAX	46.27	4.47	5.26	4.00	**2.57**
2D STD	7.76	1.19	0.61	1.11	**0.39**
3D MEAN	18.02	10.33	5.28	9.64	**2.07**
3D MAX	93.69	30.15	19.01	28.38	**4.69**
3D STD	14.70	9.35	3.01	9.10	**0.88**
FIX	7.1%	–	–	–	–

position, which introduces large bias to the pose graph. (2) Severe satellite occlusion over long periods prevents the correction of the current epoch by neighboring epochs. This illustrates that, for loosely-coupled systems, a long period of continuous harsh environment can seriously deteriorate the final performance.

On the other side, The GLIO-SS method, which tightly fuses the raw GNSS measurements with scan-to-map LiDAR and IMU measurements, demonstrates substantial improvement over RTKLIB and standalone LIO methods. Specifically, it reduces the 2D error to 1.53 meters, while the standard deviation and maximum error are 1.11 and 4.00 meters. As mentioned above, the LIO can maintain accuracy at a pretty high level in such a short trajectory. Therefore, when the LiDAR is assigned with higher weight, the adopted scan-to-map LiDAR factor is effective in mitigating the impact of unhealthy GNSS observations for integrated system and helping to achieve better results. However, GNSS-SS fails to mitigate the vertical drift from LIO.

It can be concluded that there are two drawbacks to GLIO-SS. Firstly, the weighting of the residuals from different sensors is not well balanced. During the epochs with few satellite observations, reducing the weight of the GNSS residuals prevents

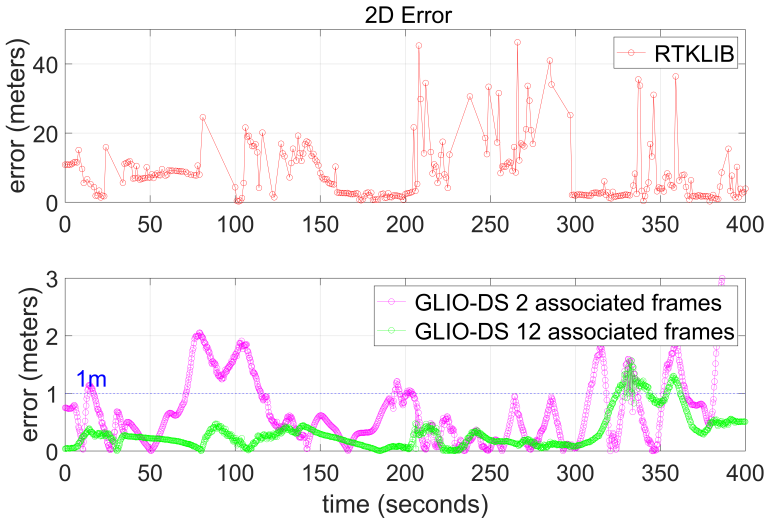

Figure 4.6: 2D positioning error through RTKLIB and GLIO-DS with different multi-scan pairs. The red, blue, and green curves denote the error of RTKLIB, GLIO-DS with 2 adjacent frame pairs as well as with 12 adjacent frame pairs, respectively. Notably, the error from lever arm is compensated by subtracting 1meter and then taking the absolute value.

the system from using the GNSS information effectively, and enlarging the GNSS residuals makes the system less robust to outliers. Secondly, the lack of consistency in the construction of the optimization problem makes the system always biased when estimating the state. These two drawbacks limit the performance of a tightly-coupled integration system.

Eventually, GLIO-DS is performed to further demonstrate the effectiveness of the proposed two stages of optimization. GLIO-DS demonstrates superior performance with 2D errors of 1.21 meters, with standard deviation and maximum error of 0.39 meters and 2.57 meters, respectively. More importantly, the vertical drift is corrected substantially. It should be noted that there is no prior information for GNSS-DS, therefore, it proved that the second stage optimization effectively mitigates the impact of unhealthy GNSS observations through the construction of consistent optimization problems and batched utilization of long periods of data to achieve the ideal performance.

To further demonstrate the effectiveness of the scan-to-multi-scan LiDAR factor in the integration optimization problem, we further compared the GLIO-DS with different associated frame numbers, namely with 2 adjacent frames and 12 adjacent frames. The latter frame number is selected considering both accuracy and computational efficiency. As shown in Fig. 4.6, GLIO-DS with more associated frames achieves significant local smoothness and global accuracy. GLIO-DS with only 2 associated frames suffered from geometrical and quantitative limitations on relative pose information. The comparison results proved that the scan-to-multi-scan LiDAR factor can provide high-quality relative constraint information, which is highly complementary to other absolute positioning information, enabling lossless and consistent global estimation.

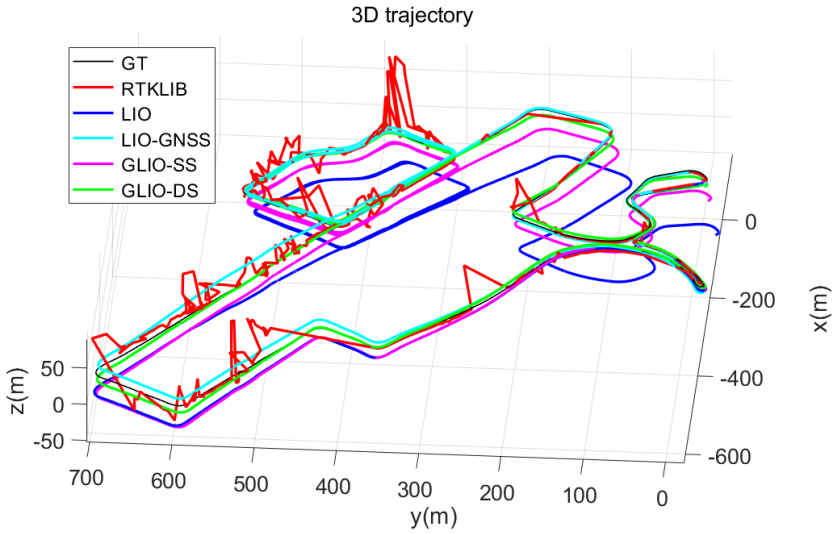

Figure 4.7: 3D trajectory in Whampoa. The black, red, blue, cyan, magenta, and green curves denote the trajectory of ground truth, RTKLIB, LIO, LIO-GNSS, GLIO-SS, and GLIO-DS, respectively.

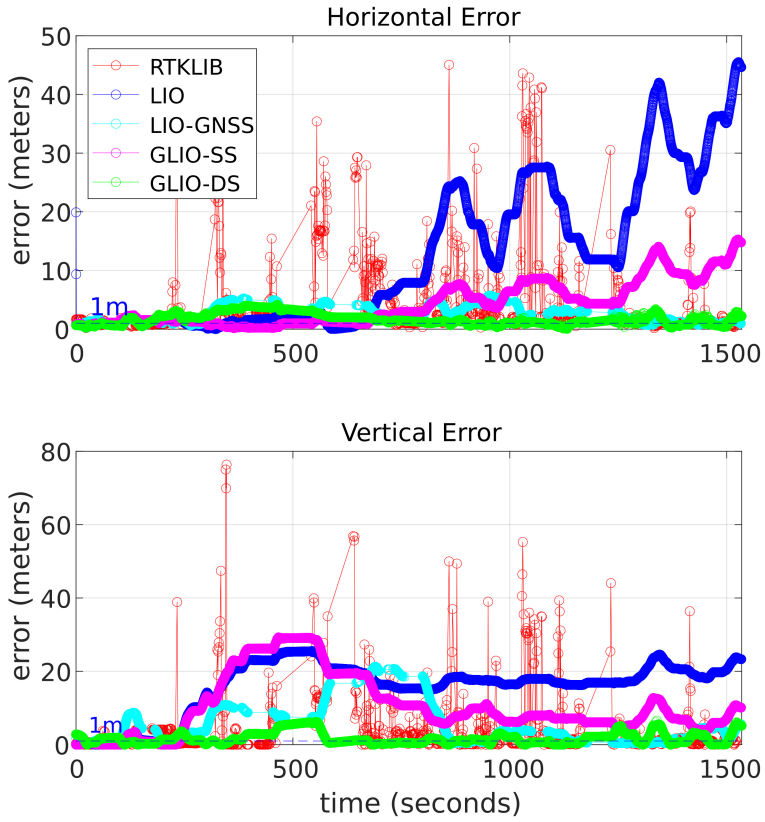

Figure 4.8: Positioning error in Whampoa. The red, blue, cyan, magenta, and green curves denote the error of RTKLIB, LIO, LIO-GNSS, GLIO-SS, and GLIO-DS, respectively.

Evaluation of Data Whampoa

The second experiment is conducted in the complex urban environment of Hong Kong, including a large number of high-rising buildings and dynamic objects, which are challenging for both GNSS and LiDAR measurements. The evaluated positioning error of the four methods in Whampoa is shown in Table. 4.2. MEAN denotes the positioning error in meters. MAX denotes the maximum error in the trajectory. STD denotes the standard deviation. FIX represents the fix rate of GNSS-RTK provided by RTKLIB. First, the LIO method shows significant drift with increasing driving distance, resulting in a maximum 2D error of 45.51 meters at the end of the

trajectory. Second, the quality of GNSS measurements is also clearly shown by the low fix rate in Table. 4.2. The vehicle starts the trajectory at open sky areas, where the positioning result of RTKLIB is maintained within two meters. However, based on Fig. 4.7 and Fi. 4.8, in the intervals from 300s to 350s, from 400s to 600s, and around 1000s, when the vehicle travels through sparse high-rise buildings, dense and narrow residential paths, and medium-height building environments, respectively, the GNSS positioning accuracy is severely affected by up to several tens of meters. As a result, the RTKLIB method resulted in a 2D mean error of 7.74 meters with a maximum error of 49.37 meters and a 3D mean error of 9.90 meters with a maximum error of 98.85 meters.

With huge biases in both GNSS and LiDAR measurements, the first stage fusion only accomplishes a fixed weighted estimation based on each sensor's measurements separately and is unable to find the global optimal by exploiting the consistency of the correlation between the sensors. Table. 4.2 shows the evaluation results of the GLIO-SS method by suppressing the system errors to some extent but failing to maintain local smoothness and therefore resulting in relatively high positioning error. Specifically, it achieves a 2D error of 4.40 meters, while the standard deviation and maximum error are 3.80 and 15.27 meters. LIO-GNSS achieves reliable accuracy and robustness with a 2D mean error of 2.68 meters and a 3D mean error of 7.44 meters. However, the loosely-coupled method strongly relies on the quality of the position estimation for accuracy and uncertainty. As a result, the accuracy of LIO-GNSS fluctuates considerably in several challenging areas, especially for the vertical axis. Ultimately, GLIO-DS achieves the best performance among all the compared methods with 2D errors of 1.68 meters and standard deviation and maximum error of 0.96 meters and 4.17 meters, respectively. Specifically, the GLIO-DS also achieves much better performance on vertical accuracy and obtains a 3D mean error of 3.34 with 9.15 meters as a maximum, despite the challenging environments.

Table 4.2: Evaluated positioning error of the four methods in Whampoa. MEAN represents the mean positioning errors in meters. Max represents the maximum positioning errors in meters. STD represents the standard deviation of positioning errors in meters. FIX denotes the GNSS-RTK fix rate.

ALL DATA	RTKLIB	LIO	LIO-GNSS	GLIO-SS	GLIO-DS
2D MEAN	7.74	12.63	2.68	4.40	**1.68**
2D MAX	49.37	45.51	5.73	15.27	**4.17**
2D STD	10.11	12.55	1.44	3.80	**0.96**
3D MEAN	9.90	28.36	7.44	14.72	**3.34**
3D MAX	98.85	69.06	23.91	30.09	**9.15**
3D STD	15.67	16.94	5.84	7.76	**2.21**
FIX	17.3%	–	–	–	–

In conclusion, the proposed tightly-coupled GNSS/LiDAR/IMU integrated positioning method firstly tightly fused the GNSS pseudorange measurements, Doppler measurements, LiDAR measurements, and IMU measurements through a common factor graph optimization. Secondly, it effectively mitigates the effects of GNSS outliers through globally consistent large-scale FGO at the second stage fusion, which effectively improves positioning accuracy and robustness.

Analysis of Computational Efficiency

Regarding computational efficiency, data preprocessing, the first stage fusion and the second stage optimization are the main parts for time-consuming. We adopt the open-sourced LILI-OM as the LIO basis for the proposed system, therefore, the data preprocessing and frontend optimization share a similar cost of time. The preprocessing of GNSS, IMU measurements, and scan-to-map LiDAR features for the first stage and the scan-to-multi-scan LiDAR features for the second stage fusion together cost less than 40ms per frame. The first stage fusion takes around 30ms, which is less than baseline backend fusion as fewer LiDAR constraints are selected for the optimization problem. Moreover, we set the maximum iteration number as 50 and the maximum optimization time as 3s for the second stage optimization on a

separate thread. The local pose re-initialization takes less than 10ms. Therefore, the total time consumption for the system is less than 100ms per frame, which enables real-time operation on 10Hz LiDAR sensors.

4.4 Conclusion

Modern intelligent vehicles demand higher continuous positioning accuracy due to their diverse outdoor application scenarios. This chapter presents GNSS/LiDAR/IMU tightly-coupled odometry that: (1) tightly fuses the GNSS, LiDAR, and IMU all at raw measurement level through FGO, and (2) employs two stages optimization including sliding-window based frontend and batched backend fusion to achieve efficient, consistent and robust positioning solutions. Within the proposed two stages of optimization, different LiDAR factors such as the scan-to-map scheme in the frontend and the scan-to-multi-scan scheme in the backend are employed. Experimental results on several challenging sequences collected in Hong Kong have demonstrated the effectiveness of the proposed method. The system has exhibited reliable accuracy and robustness in challenging urban environments by utilizing commercial-level GNSS receivers and a LiDAR/IMU sensor kit.

Chapter 5

3DLA GNSS NLOS Correction by DOA Estimation Using Doppler Measurements in Urban Canyons

5.1 Introduction

While existing 3D LiDAR-aided GNSS NLOS correction methods have significantly improved urban positioning performance, they still largely rely on the shortest-path assumption to identify the most likely reflection route among multiple candidates. This assumption, however, neglects the underlying physical propagation characteristics, especially in complex urban environments where longer paths may yield stronger reflections due to surface materials such as glass. To move beyond this limitation, recent research has highlighted the potential of Doppler measurements—traditionally used for velocity estimation—as an alternative information source. In particular, Doppler shifts under NLOS conditions implicitly encode the Direction-of-Arrival (DOA) of the reflected signal, offering a new perspective for path discrimination. However, practical DOA estimation from Doppler remains underexplored, especially in systems with a single antenna and no access to ground-truth velocity. Existing approaches, such as [35], have demonstrated the feasibility of DOA-based reflection path identification using Doppler observations and ray-tracing simulations, but

their reliance on exhaustive search and ground-truth motion limits their real-world applicability. To address these challenges, the following chapter introduces a 3D LiDAR-aided GNSS NLOS correction framework that leverages Doppler-based DOA estimation, supported by LiDAR-derived velocity information. This method enables accurate identification of the true reflection path without the shortest-path assumption, the contributions of this work can be concluded as follows:

(1) We propose a 3D LiDAR-aided GNSS signal DOA estimation method using the Doppler measurement, together with a thorough accuracy analysis of DOA estimation based on LiDAR-derived prior velocity.

(2) We propose a 3D LiDAR-aided GNSS NLOS correction framework leveraging signal DOA and LiDAR PCM, which includes multi-ray reflection point tracking and residual-based reflection point determination, addressing challenges such as signal penetration, modeling inaccuracies, and DOA biases.

(3) Extensive experimentation in challenging scenarios: The proposed method has been demonstrated through experimentation in various challenging urban scenarios in Hong Kong.

To the best of our knowledge, this work represents the first attempt to accurately track NLOS signal paths for urban GNSS applications by integrating 3D LiDAR and GNSS Doppler measurements.

5.2 Methods

5.2.1 System Overview

The proposed method is illustrated in Fig. 5.1 and comprises three main stages. First, the system initializes using GNSS/LiDAR/IMU integrated odometry to deter-

mine the initial position, velocity, and PCM. For this stage, we adopt an open-sourced tightly-coupled GNSS/LiDAR/IMU integrated odometry (GLIO) [1]. In the second stage, receiver clock bias drift estimation in snapshot mode is performed alongside GNSS signal DOA estimation. The third stage involves candidate reflection path restoration, pseudorange correction evaluation, and positioning with final pseudorange correction. For simplicity, all the states and the positions are transformed in an earth-centered, earth-fixed (ECEF) frame in this chapter.

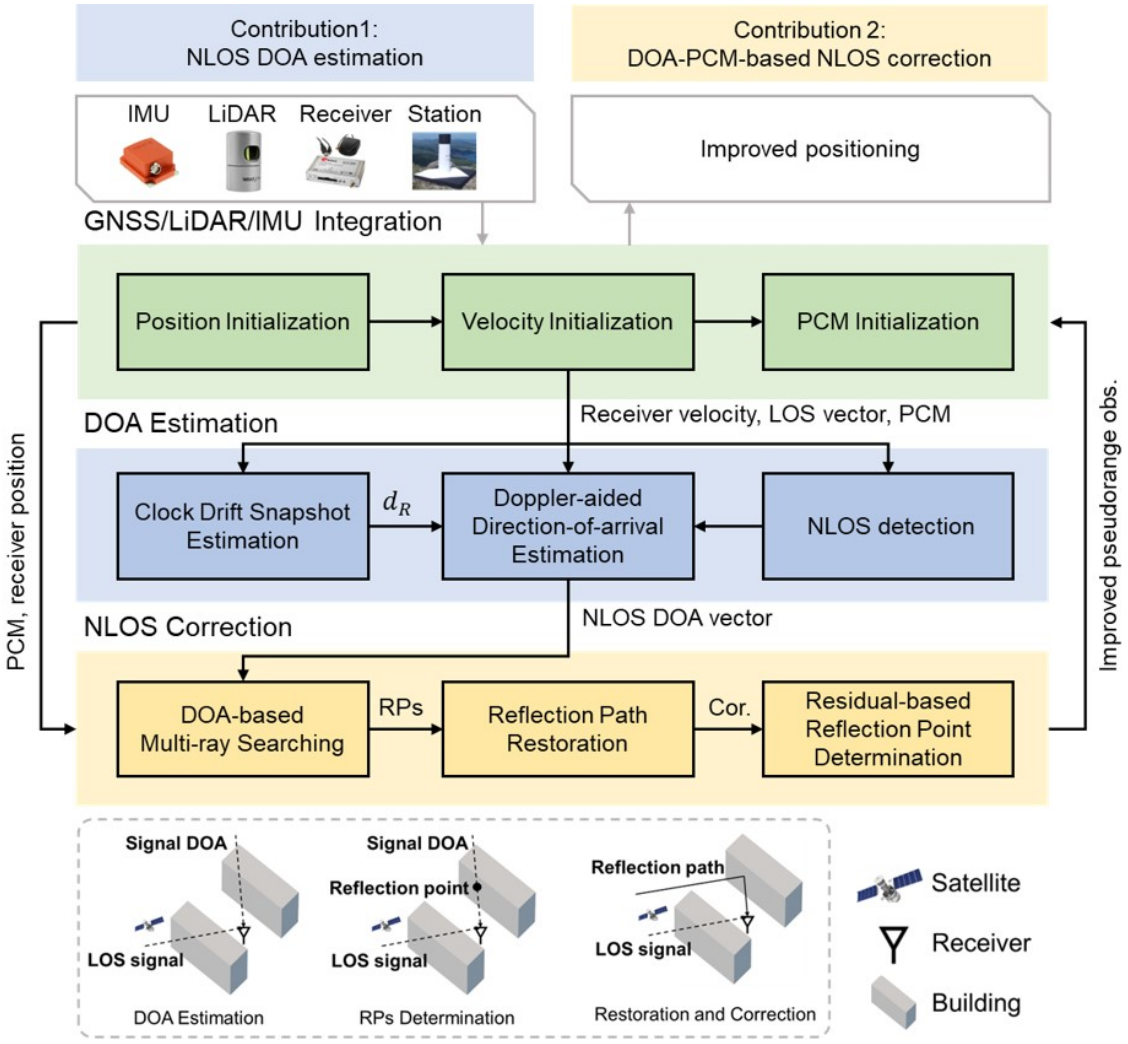

Figure 5.1: The overview of the system pipeline.

5.2.2 3D LiDAR aided GNSS Signal Direction-of-Arrival Estimation using Doppler Measurement

This section introduces the 3D LiDAR-aided DOA estimation method based on Doppler observations, encompassing the first two stages outlined in the system overview. The following discussion will cover the Doppler observation model for NLOS signals, system initialization, and optimization-based Doppler DOA estimation. The first part establishes the theoretical foundation, while the latter two demonstrate the implementation of the proposed method.

Doppler Observation Modeling for NLOS Signal

We first analyze the effect of signal reflection on Doppler observations based on the Doppler observation function. The Doppler observation function is described as [109]:

$$\lambda d^s_{r,t} = \mathbf{e}^{s,\text{SatLOS}}_{r,t}\mathbf{v}_{s,t} - \mathbf{e}^{s,\text{SourceLOS}}_{r,t}\mathbf{v}_{r,t} + c\left(\dot{\delta}^i_{r,t} - \dot{\delta}_{s,t}\right) + \zeta^s_{r,t} \tag{5.1}$$

where λ represents the signal wavelength of the individual satellite, $d^s_{r,t}$ is the Doppler measurement from the receiver. The satellite velocity and the receiver velocity are given by $\mathbf{v}_{s,t}$ and $\mathbf{v}_{r,t}$, respectively. $\zeta^s_{r,t}$ denotes the Doppler observation noise. $c\left(\dot{\delta}^i_{r,t} - \dot{\delta}_{s,t}\right)$ represents the observation bias by the clock drift with c as the speed of light, while the satellite clock bias drift $\dot{\delta}_{s,t}$ can be priorly calibrated, the receiver clock drift $\dot{\delta}^i_{r,t}$ is an unknown and needs to be estimated. $\mathbf{e}^{s,SatLOS}_{r,t}$ represents the direction between the receiver and the satellite while $\mathbf{e}^{s,SourceLOS}_{r,t}$ represents the LOS vector from the receiver to the signal source, which can be regarded as signal DOA.

Generally, $\mathbf{e}^{s,SourceLOS}_{r,t}$ is the same as $\mathbf{e}^{s,SatLOS}_{r,t}$ when the signal is directly received from the satellite. However, for NLOS receptions, as depicted in Fig. 5.2, the receiver can only receive the reflected signal, where $\mathbf{e}^{s,SourceLOS}_{r,t}$ represents the LOS vector between the receiver and the reflection point rather than the satellite. With the

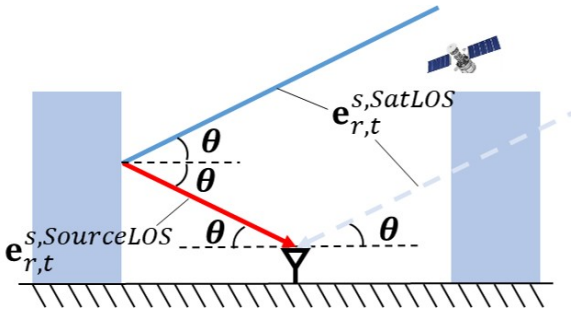

Figure 5.2: Demonstration of directional vector for NLOS reception. The blue boxes are buildings, the blue line and dash line represent the LOS transmission direction, the red line represents the NLOS reflection transmission direction, θ represents the elevation angle.

receiver velocity and receiver clock drift, the Doppler observation provides the angle between the receiver velocity and $\mathbf{e}_{r,t}^{s,SourceLOS}$ according to (1). This relationship serves as a constraint for estimating the DOA. Furthermore, assuming that most reflecting planes are perpendicular to the ground, the elevation angle θ of the reflected signal's DOA is equivalent to that of the LOS signal, offering an additional constraint for DOA estimation. These constraints collectively establish the theoretical basis for estimating the signal DOA ($\mathbf{e}_{r,t}^{s,SourceLOS}$).

System Initialization and Receiver Clock Bias Drift Estimation

Based on the Doppler observation function, the initialization of receiver velocity, and the clock bias drift is required for DOA estimation. We adopt GLIO [1] as a tightly coupled integration system for velocity initialization, which fuses Differential GNSS (DGNSS) [16] (raw pseudorange measurements and Doppler measurements), LiDAR, and IMU measurements. The factor graph design in GLIO ensures global consistency between GNSS and LiDAR measurements, enabling reliable velocity estimation even in highly urbanized areas.

After velocity initialization, we perform snapshot clock bias drift estimation using Doppler observations from all satellites in an epoch. Assuming no NLOS reception, the receiver clock bias drift can be calculated using a single Doppler observation with

the equation:

$$\dot{\delta}_{r,t} = \left(\lambda d^s_{r,t} - \mathbf{e}^{s,SatLOS}_{r,t}\mathbf{v}_{s,t} + \mathbf{e}^{s,SatLOS}_{r,t}\mathbf{v}_{r,t} + \dot{\delta}_{s,t}\right)/c \tag{5.2}$$

By averaging Doppler observations across all visible satellites, random measurement noise is reduced, allowing for a reliable estimation of the receiver clock bias drift [35].

Optimization-based DOA Estimation

Essentially, estimating the signal DOA involves determining a two-degree-of-freedom (DoF) rotation, namely the elevation angle and the azimuth angle. The elevation angle can be determined by following the elevation angle assumption, which assumes the elevation angle of the reflected signal is equivalent to the LOS signal. Therefore, the DOA estimation is simplified to a one DoF estimation, which estimates the azimuth angle with a given elevation. We translate the above problem into estimating a rotation angle α of the LOS vector about a vertical axis perpendicular to the ground. This rotation inherently incorporates the elevation angle constraint. The observation equation for this rotation angle can be derived from the Doppler observation equation. Specifically, we take the ground normal vector $\hat{\mathbf{p}}_{r,t}$ as the vertical axis, which is calculated from the unitization of the receiver ECEF coordinate $\mathbf{p}_{r,t}$. Then the DOA vector $\mathbf{e}^{s,SourceLOS}_{r,t}$ can be represented as a rotated LOS vector $\mathbf{e}^{s,SatLOS}_{r,t}$ around the ground normal vector $\hat{\mathbf{p}}_{r,t}$ by the rotation angle α. Mathematically, $\mathbf{e}^{s,SourceLOS}_{r,t}$ can be expressed by:

$$\mathbf{e}^{s,SourceLOS}_{r,t} = \cos\alpha\,\mathbf{e}^{s,SatLOS}_{r,t} + (1-\cos\alpha)(\hat{\mathbf{p}}_{r,t}\cdot\mathbf{e}^{s,SatLOS}_{r,t})\hat{\mathbf{p}}_{r,t} + \sin\alpha\left(\hat{\mathbf{p}}_{r,t}\times\mathbf{e}^{s,SatLOS}_{r,t}\right) \tag{5.3}$$

With the initial velocity and the estimated receiver clock bias drift, a Doppler observation function in terms of α by combining (5.1) and (5.3) can be constructed.

Therefore, the constraint from Doppler measurements for α estimation is carried out with the residual formulated as:

$$res_{r,t}^{s,DoppDOA} = \lambda d_{r,t}^{s} - \lambda d_{r,t}^{s,predict} \tag{5.4}$$

where $d_{r,t}^{s,predict}$ is the predicted Doppler measurement with a certain α. In conclusion, the optimization problem for DOA estimation for satellites in a single epoch t can be formulated as:

$$\chi^* = \arg\min_{\chi} \sum_{S} \left\| res_{r,t}^{s,DoppDOA} \right\|^2 \tag{5.5}$$

with states being expressed as:

$$\boldsymbol{\chi} = [a_r^0, \cdots, a_r^s]$$

For each satellite s, we optimize α to reduce the Doppler residual $res_{r,t}^{s,DoppDOA}$ towards zero and obtain the estimated DOA with (5.3). To be noted, solving such a problem involves solving a cosine function, which yields two results. The selection and validation of the final DOA of the signal are performed together with the following NLOS correction process.

5.2.3 DOA-based NLOS Correction with 3D PCM

In this section, we introduce the signal reflection path restoration using signal DOA and NLOS correction. This work adopts the single reflection assumption. The NLOS detection is performed based on a combination of our previous 3DLA NLOS detection method [22] and residual check using the initialized receiver positions. Considering that the reflected signals experience a longer transmission path, the satellites with PCM occlusion and double-difference (DD) pseudorange residual larger than a certain threshold will be classified as NLOS receptions. In our implementation, the threshold is experimentally determined as 5 meters. Notably, this approach can still involve part of multipath receptions as NLOS receptions.

Intersection point searching for Reflection Point Determination

The determination of the reflection point involves identifying the intersection point between the ray emitted from the receiver along the signal's DOA and the 3D PCM. The search strategy is first developed in our previous 3DLA NLOS detection and correction methods [22]. It uses a nearest-point search within a moving spherical region, as depicted in Fig. 5.3. The search begins with the receiver's position as the initial center and progressively shifts the search center along the specified direction in increments of step size d. Centered at each search point, the nearest neighbor search with a radius r is performed within the 3D PCM. At the beginning, the search space does not overlap with the reflection region and therefore does not return the nearest point. When the radius search successfully returns the nearest point, it is identified as a potential reflection point, and the searching process is terminated. The maximum searching range is 100 meters. The selection of step size d and radius r depends on the resolution of 3D PCM. In this work, d is set to 0.5 meters and the r is 0.8 meters.

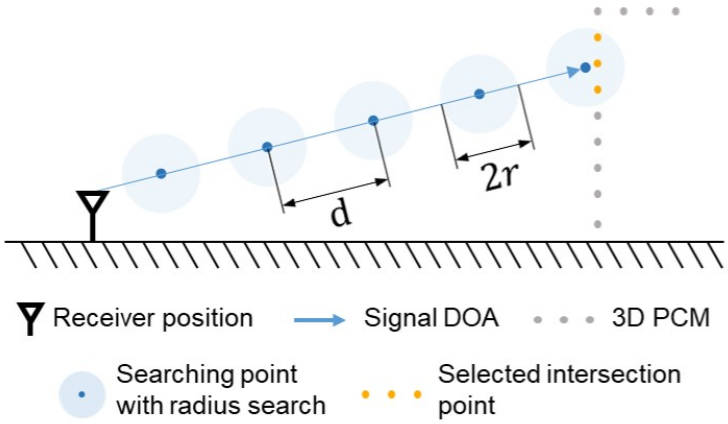

Figure 5.3: Demonstration of intersection point searching.

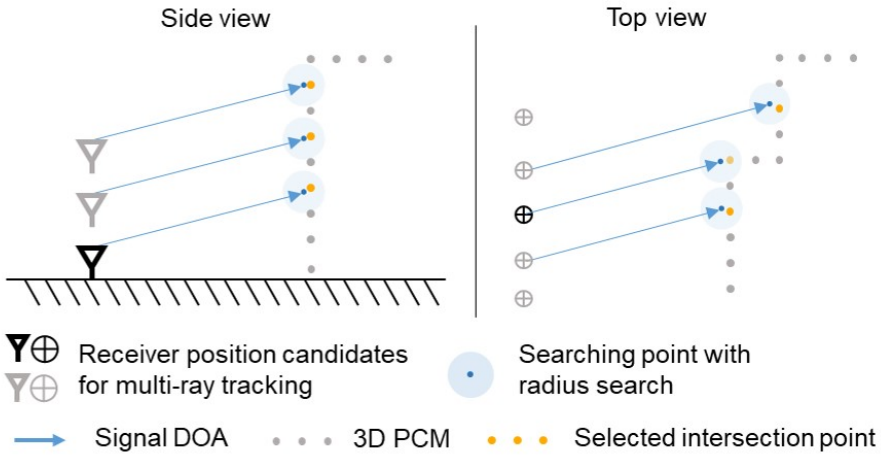

Figure 5.4: Demonstration of multi-ray tracking with given receiver position and signal DOA.

Multi-Ray Tracking

The estimation of NLOS DOA may be influenced by initial velocity error, Doppler observation noise, or the inaccurate receiver clock bias drift, all of which can affect the determination of the reflection point. More importantly, factors such as vegetation, dynamic object artifacts, and smooth surfaces like glass curtain walls can significantly affect the reliability of reflection point determination. Reflection point identification relies on occlusion detection, and sparse vegetation presents challenges in handling signal penetration. Meanwhile, point cloud reconstruction with dynamic objects and smooth surfaces cannot accurately represent the true reflective environment. To address these challenges, we leverage the similarity of environmental structures within a small region and propose to adopt the multi-ray searching strategy, which is inspired by conventional 3DMA GNSS position candidate sampling, as illustrated in Fig. 5.4. Given the antenna position and the signal DOA, we sample multiple antenna position candidates and perform intersection point searching for all candidates, generating a set of reflection points and corresponding signal path candidates. Antenna position sampling is conducted in two directions: the first is

along the vehicle's driving direction, and the second is vertically upward. This choice ensures that changing the antenna position does not alter its relative distance to the buildings. Since the street direction is not explicitly estimated, the vehicle's driving direction is used as an approximation. To balance computational efficiency and the accuracy gains from a larger sampling range, the sampling range in the driving direction is set to ±7 meters, while the vertical sampling range is set to 0 to 3 meters. Additionally, the sampling resolution is set to 1 meter. By doing so, the searching range of the reflection point can be effectively expanded by leveraging environmental similarity within a small spatial area without significantly modifying the DOA of the signal. For each NLOS reception, the search of reflection point candidates is performed twice due to two DOA solutions.

NLOS Correction Formulation and Validation

For each NLOS reception, two sets of reflection point candidates are identified due to two DOA solutions. The reflection path for each candidate is reconstructed by sequentially connecting the receiver position, the reflection point, and the satellite. NLOS correction is then performed by calculating the additional travel distance of the reflected signal, determined by subtracting the direct LOS path from the reflection path. There are two models for correction calculation categorized by different angle β between the reflected signal and the LOS signal, which is shown in Fig. 5.5. For reflected signals with β larger than 90 degrees, the correction of the pseudorange observation can be calculated by:

$$\nabla\rho = \left\|\mathbf{L}^{Refl}\right\| + \left\|\mathbf{L}^{Proj}\right\| \tag{5.6}$$

$$\left\|\mathbf{L}^{Proj}\right\| = \left\|\mathbf{L}^{Refl} * \mathbf{e}^{SatLOS}\right\| = -\left\|\mathbf{L}^{Refl}\right\| \cos\beta \tag{5.7}$$

where $\mathbf{L}^{Refl}$ represents the vector from the receiver position to the reflection point.

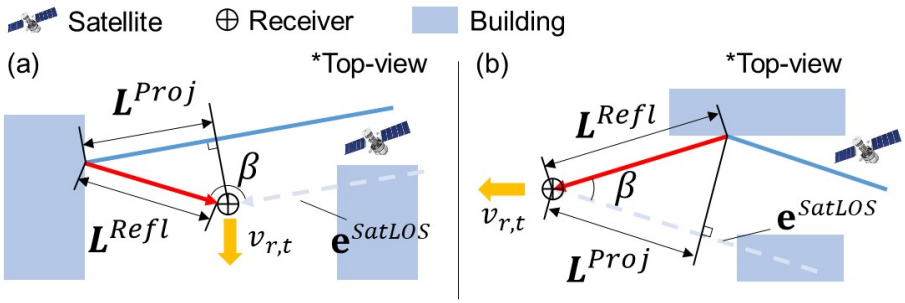

Figure 5.5: Two cases of NLOS correction.

$\mathbf{L}^{Proj}$ denotes the projected vector of $\mathbf{L}^{Refl}$ on the LOS vector $\mathbf{e}^{SatLOS}$. $\|\cdot\|$ represents vector modulus.

For reflected signals with β smaller than 90 degrees, the correction can be expressed by:

$$\nabla\rho = \left\|\mathbf{L}^{Refl}\right\| - \left\|\mathbf{L}^{Proj}\right\| \tag{5.8}$$

$$\left\|\mathbf{L}^{Proj}\right\| = \left\|\mathbf{L}^{Refl} * \mathbf{e}^{SatLOS}\right\| = \left\|\mathbf{L}^{Refl}\right\| \cos\beta \tag{5.9}$$

Combining 5.6, 5.7, 5.8, 5.9, the correction formulation is summarized as:

$$\nabla\rho = \left\|\mathbf{L}^{Refl}\right\| * (1 - \cos\beta), \quad \beta \in (0, \pi) \tag{5.10}$$

To determine the final reflection point for each NLOS reception, the residual check is applied for the selection and validation among the reflection point candidates. In this work, we perform residual-check based on DD pseudorange residual calculated by initial position, which is given by:

$$\rho^s_{DD,r,t} = (\rho^s_{r,t} - \rho^s_{e,t}) - (\rho^w_{r,t} - \rho^w_{e,t}) \tag{5.11}$$

$$r^s_{DD,\rho,r,t} = \rho^s_{DD,r,t} - (rang^s_{r,t} - rang^s_{e,t}) - (rang^w_{r,t} - rang^w_{e,t}) \tag{5.12}$$

where the range distances $rang^s_{r,t}$, $rang^s_{e,t}$, $rang^w_{r,t}$ and $rang^w_{e,t}$ are calculated based on the initial position of the receiver $\mathbf{p}_{r,t}$:

$$rang^{s}_{r,t} = \|\mathbf{p}_{r,t} - \mathbf{p}_{s,t}\|, \quad rang^{s}_{e,t} = \|\mathbf{p}_{e} - \mathbf{p}_{s,t}\| \tag{5.13}$$

$$rang^{w}_{r,t} = \|\mathbf{p}_{r,t} - \mathbf{p}_{w,t}\|, \quad rang^{w}_{e,t} = \|\mathbf{p}_{e} - \mathbf{p}_{w,t}\| \tag{5.14}$$

where $\mathbf{p}_{s,t}$ and $\mathbf{p}_{w,t}$ are satellite positions, $\mathbf{p}_e$ is the position of the reference station. The final correction candidate is selected with minimum difference between $r^{s}_{DD,\rho,r,t}$ and $\nabla\rho$.

5.3 Experimental Evaluation

The proposed method is evaluated on two challenging sequences collected in Hong Kong from an open-source dataset, *UrbanNav* [106]. Fig. 5.6 shows the experimental trajectories and the environment, characterized by densely distributed buildings and tall trees. These features result in considerable GNSS NLOS and multipath receptions. To demonstrate the effectiveness of the proposed method, we conduct analyses and evaluations in the following aspects, namely (1) the impact of velocity bias on DOA estimation, (2) the accuracy of NLOS correction results, (3) positioning performance comparison with and without the proposed NLOS correction, and (4) the computational efficiency of the proposed method. Notably, only driving periods are evaluated. The proposed method is implemented in a post-processing manner using C++ and ROS [103], and the optimization is performed via Ceres Solver [104].

The data collection platform in this study is described in the UrbanNav dataset [106]. It includes a u-blox F9P GNSS receiver for collecting raw single-frequency GPS/BeiDou signals at 1 Hz, an Xsens Ti-10 IMU for inertial measurements at 100 Hz, and a Velodyne HDL-32E LiDAR for point cloud observations at 10 Hz. The ground truth is provided by the NovAtel SPAN-CPT system, which integrates a high-precision multi-frequency, multi-constellation GNSS receiver with a tactical-grade inertial sensor to ensure absolute accuracy. All data sources are well-synchronized,

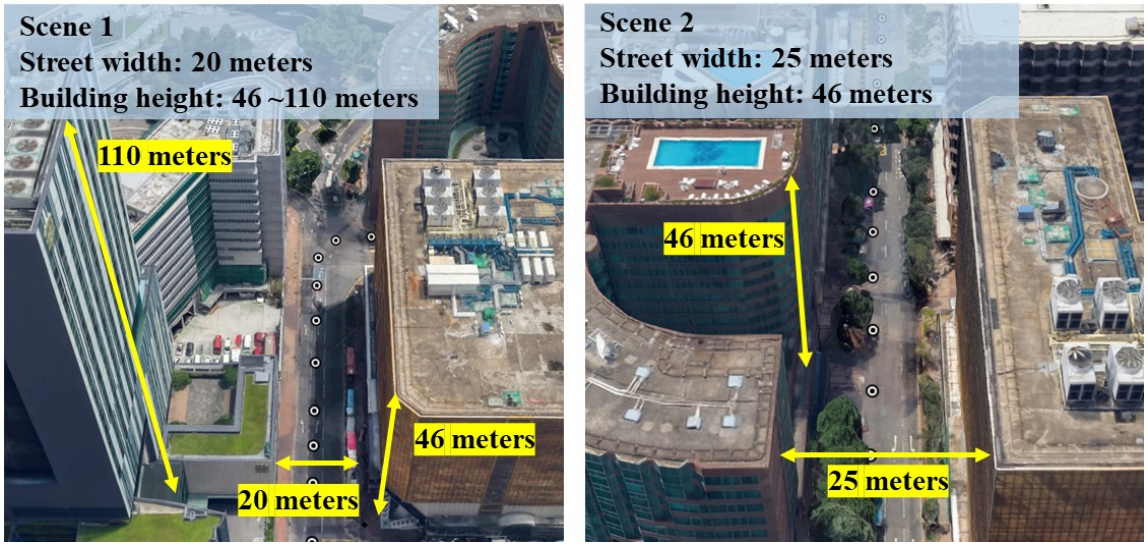

Figure 5.6: The trajectory of the vehicle in the evaluation, together with demonstrations of data collection scenes.

with time synchronization and extrinsic parameters calibration. To eliminate the impact of the single LiDAR's limited FOV in the evaluation, a public 3D city dataset in Hong Kong [110] is used to enhance the actual point cloud observations. The large-scale PCM from the dataset is segmented into local subdivisions with a specification of 100100 meters, whose resolution is set to 1 meter. For each epoch, the related subdivision is transformed according to the initialized position by GLIO to simulate the actual sensor-centric 3D point cloud observation, as shown in Fig. 5.7.

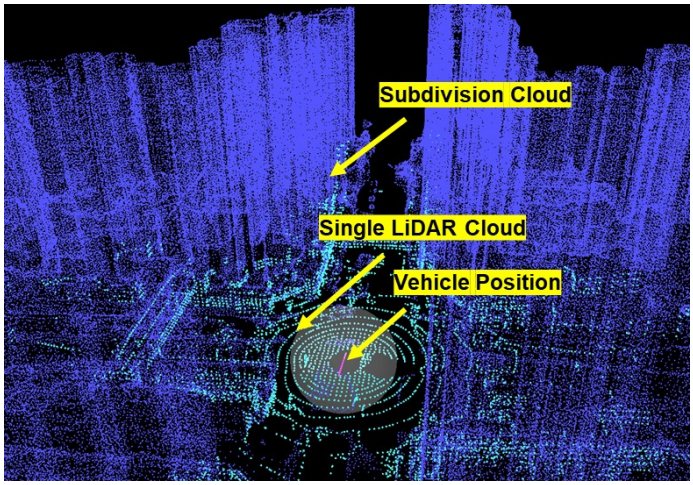

Figure 5.7: The demonstration of subdivision cloud and single LiDAR frame cloud.

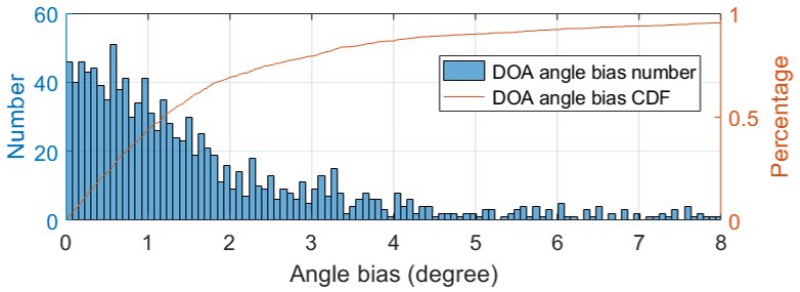

Figure 5.8: The distribution and the cumulative distribution function (CDF) of the angle bias between the estimated DOA and the satellite LOS in the open-sky area.

5.3.1 Evaluation of Velocity Bias on DOA Estimation

To demonstrate the accuracy of the proposed DOA estimation method, we provide the DOA estimation results using the satellite observations collected in less urbanized areas, which are believed to be healthy observations with DOA closely aligning the LOS vectors. Using the proposed method, the DOA is estimated based on Doppler measurements and the vehicle velocity ground truth. The estimated DOA is then compared with the original LOS direction. Fig. 5.8 presents the distribution of the angle between the estimated DOA and the LOS direction, referred to as the DOA angle bias. The results indicate that the estimated DOA aligns well with the LOS direction for the majority of satellites, accounting for observation noise. Specifically, the Cumulative Distribution Function (CDF) of the DOA angle bias reveals that over 80% of the cases exhibit deviations within 4 degrees. A small subset of satellites displays larger discrepancies between the estimated DOA and the LOS direction, likely due to environmental interference.

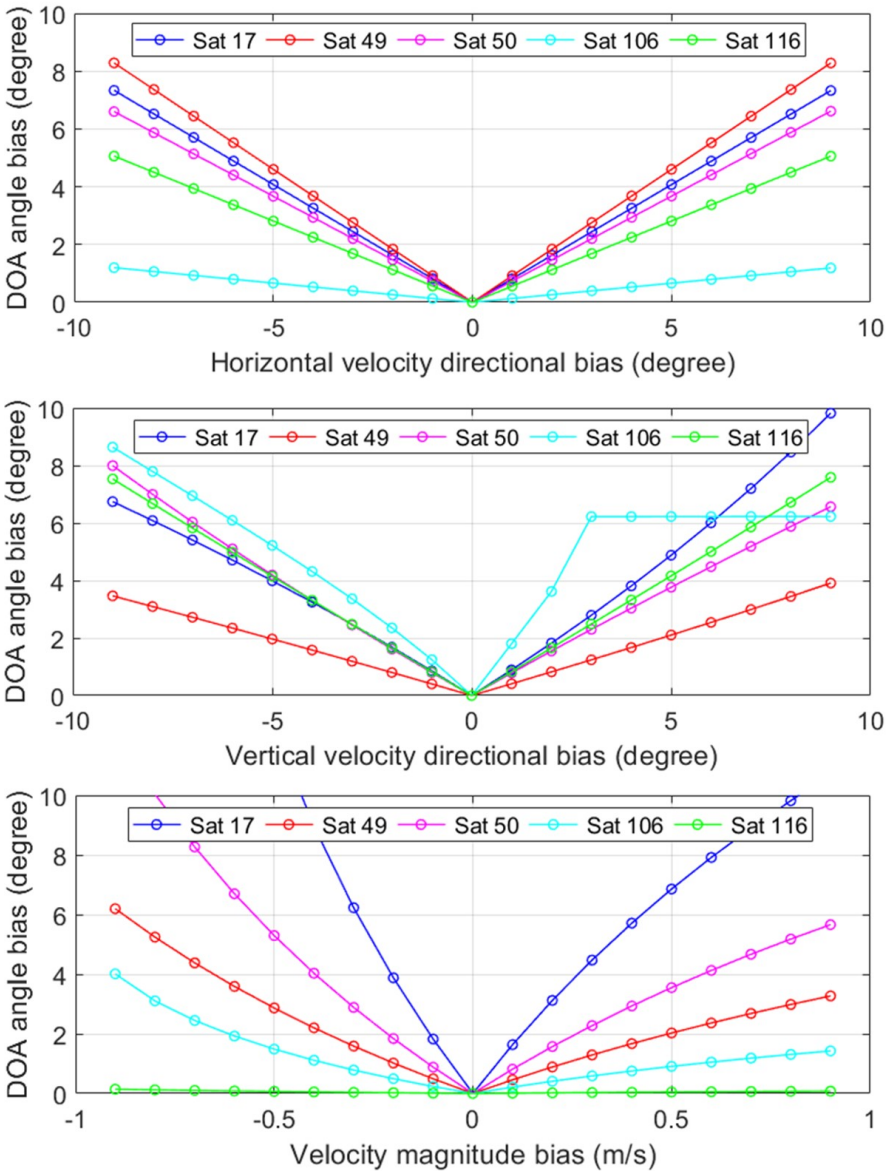

Figure 5.9: The distribution of DOA estimation error (angle bias) for different velocity biases.

Table 5.1: Satellite Information (PRN: Pseudorandom Noise Code, Ele.: Elevation Angle, IA: Included Angle Between the Direction of Receiver Velocity and Satellite LOS Vector)

PRN	17	**49**	**50**	**106**	**116**
Ele. (degree)	35	22	42	82	55
IA (degree)	130 (-50)	107 (-73)	62	96 (-84)	90

To illustrate how velocity bias affects the proposed DOA estimation, we introduce velocity offsets in three separate aspects to the healthy satellite observations, namely (1) horizontal directional bias (yaw error) with a range of ±10 degrees, (2) vertical directional bias (pitch error) with a range of ±10 degrees, and (3) magnitude bias with a range of ±1 meters/second. Fig. 5.9 depicts how the estimated DOAs of different satellites vary under different velocity biases, while Table. 5.1 provides details about the selected healthy satellites involved in the evaluation. From the figure we can observe that the DOA angle bias increases with a larger velocity bias. With horizontal directional velocity bias, satellites with higher elevation angles are less affected by DOA estimation. The DOA angle bias is always smaller than the horizontal directional bias of velocity as elevation is always larger than 0 degrees. As an example, satellite 106 has a 1.2 degrees DOA angle bias when the horizontal directional bias of velocity is 9 degrees, while satellite 49 has an 8.2 degrees DOA angle bias in the same case.

The DOA angle bias exhibits a similar upward trend when subjected to vertical directional velocity bias. However, satellites with larger elevation angles experience larger DOA angle bias. Notably, satellite 116, which has an included angle (IA) of 90 degrees between the receiver's velocity vector and the LOS vector, demonstrates a symmetric trend in DOA bias as the vertical velocity directional bias varies between -9 degrees and 9 degrees, while the variation in DOA angle bias of other satellites is asymmetric. The DOA angle bias grows faster with negative pitch error for satellites with IA less than 90 degrees, and it is reversed for satellites with IA larger than 90 degrees. This indicates that the DOA angle bias induced by vertical directional velocity bias is influenced by both the satellite's elevation angle and its IA with respect to the receiver velocity vector.

The variation in DOA angle bias due to velocity magnitude bias is exclusively dependent on the IA between the DOA and the velocity direction. More specifically,

it is related to the degree of collinearity between DOA and velocity direction. Satellite 17 with the smallest IA between DOA and velocity direction obtains the largest DOA angle bias under velocity magnitude bias while satellite 116 is unaffected with 90 degrees IA between DOA and velocity direction. For all the selected satellites, the DOA angle bias is larger when the velocity magnitude is underestimated compared with overestimated. This observation underscores the asymmetric impact of velocity magnitude bias on DOA estimation.

Overall, deviations in both the direction and magnitude of velocity have an impact on the accuracy of the proposed DOA estimation, which depends on the velocity deviation conditions, the satellite elevation, and the IA between DOA and velocity. Consequently, the proposed DOA estimation method relies on a reliable velocity prior to ensuring accurate performance.

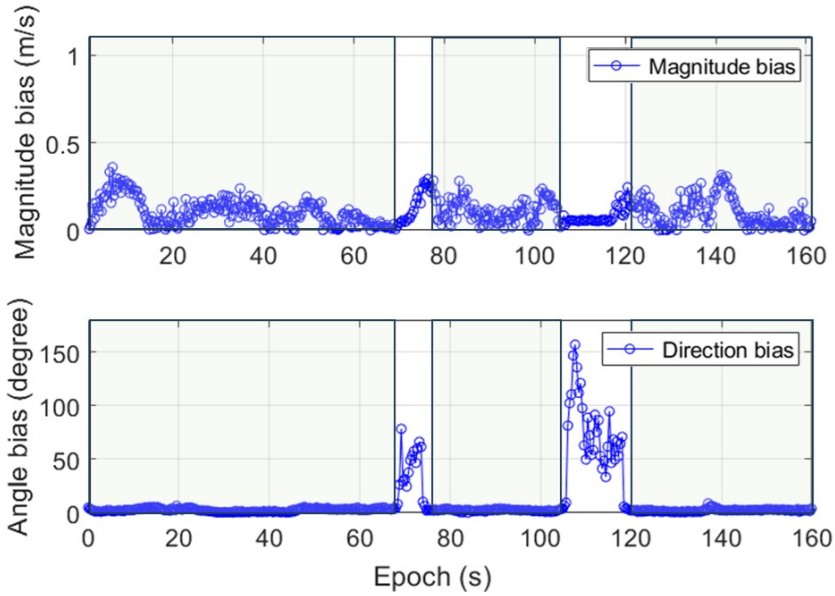

Figure 5.10: The illustration of velocity initialization bias with GLIO. The upper part shows the magnitude bias while the direction bias is depicted at the bottom. Green boxes denote the driving period.

Table 5.2: Velocity Estimation Results (Mag. MEAN: Mean Velocity Magnitude Bias, Mag. MAX: Maximum of Velocity Magnitude Bias, Ang. MEAN: Mean Velocity Directional Bias, Ang. MAX: Maximum of Velocity Directional Bias)

Mag. MEAN (m/s)	**Mag. MAX** (m/s)	**Ang. MEAN** (degree)	**Ang. MAX** (degree)
0.10	0.31	2.45	8.82

5.3.2 NLOS Correction Evaluation in Urban Canyon 1

In this section, the NLOS correction result of the proposed method is evaluated. The evaluation begins with an assessment of velocity initialization using GLIO. Fig. 5.10 illustrates the velocity initialization magnitude bias and direction bias, the driving period is marked by green boxes. The results demonstrate high accuracy in velocity estimation during the driving period. In contrast, a larger angle bias is observed during the parking period, which is attributed to small local drift. Table. 5.2 provides the statistical result in detail.

To evaluate the NLOS correction results, we compare the actual observation, the conventional 3DMA GNSS NLOS correction method [111; 79], and our proposed 3DLA NLOS correction method in terms of observation error. The ground truth position is used for calculating the actual observation error and initializing the position for the 3DMA method. Fig. 5.11 compares the CDF of DD pseudorange error before correction (actual observation error) and after correction using 3DMA and the proposed 3DLA NLOS correction methods. It shows that around 20% of the observations have more than 20 meters error. Beyond the display area, the maximum observation error can reach 100 meters, this can be caused by potential long-range reflection NLOS receptions or multi-reflection NLOS receptions. The conventional 3DMA GNSS NLOS correction method provides limited improvement and fails to correct the significant NLOS receptions. The proposed method shows a more effective performance for the NLOS correction. The percentage of observations with errors exceeding 20 meters is reduced from 20.8% to 9.6%.

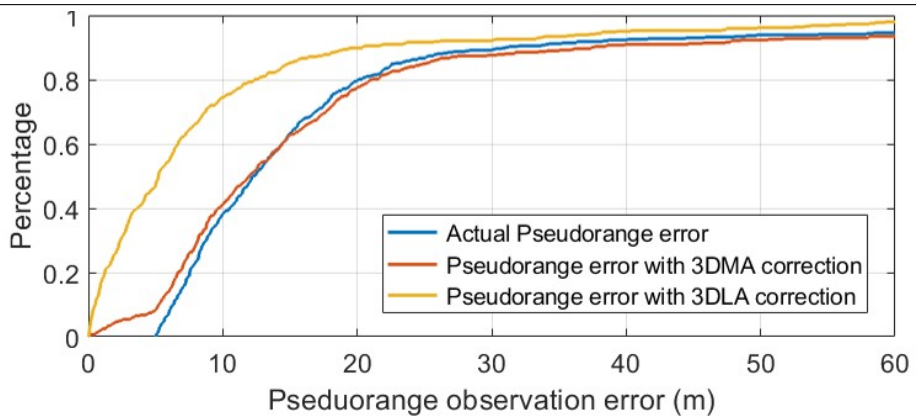

Figure 5.11: The CDF of the actual observation error (double-difference pseudorange error labeled by ground truth position) and observation error after NLOS correction, including 3DMA-based and the proposed 3DLA-based methods. The actual observation error is depicted by dark blue, the corrected CDF of 3DMA and the proposed 3DLA method are given as red and orange curves, respectively.

Table 5.3: Overview of the NLOS Correction Result for Selected Satellites (PRN: Pseudorandom Noise Code, Ele.: Elevation Angle of the Satellite, MCE: Mean Correction Error, STD.: Standard Deviation of MCE. Avail.: Availability of the NLOS Correction Result. 3DLA. and 3DMA.: Correction Result by the 3DMA Method and 3DLA Method, respectively)

PRN		**6**	**17**	**19**	**50**	**111**
Ele. (degree)		47	49	39	23	43
3DMA	MCE (m)	9.0	9.8	12.4	61.9	24.6
	STD (m)	11.9	10.1	11.0	80.7	20.2
	Avail.	32.9%	27.7%	56.0%	11.8%	20.0%
3DLA	MCE (m)	**4.9**	**2.9**	**5.7**	**7.9**	**2.8**
	STD (m)	8.0	3.4	11.4	8.2	3.3
	Avail.	**88.6%**	**95.7%**	**88.0%**	**97.1%**	**93.3%**

For detailed information on NLOS correction results, Fig. 5.12 compares the actual pseudorange observation error with the predicted error (correction) of the individual NLOS reception among epochs by 3DMA and 3DLA methods. The horizontal axis represents the epoch indices for individual satellites, the vertical axis represents the observation error in meters. For each epoch, three bars are depicted: the actual observation error in purple, the observation error predicted by the proposed 3DLA method in red, and the observation error predicted by the 3DMA method

in orange, respectively. A close alignment between the predicted observation error and the actual observation error can be regarded as a successful correction. Table. 5.3 summarizes the NLOS correction results for selected satellites, where the mean correction error is calculated by averaging the difference between the predicted observation error and the actual observation error. It is observed that the 3DMA NLOS correction obtains lower correction availability compared with the proposed method. This is primarily due to the limitations of 3D city models, which use planar representations to describe environmental reflectance. The resolution and reconstruction accuracy of these planar models are insufficient to reliably determine reflection points on actual building facades. Regarding the available 3DMA correction results, there exists a considerable discrepancy between the predicted observation error and the actual observation error, indicating that the NLOS reflection paths are not restored correctly. For example, the 3DMA predicted errors for satellite 19 are smaller than actual errors in most epochs. This discrepancy arises not only from the limitations of the models but also from the shortest path assumption employed by 3DMA, which often selects shorter but incorrect reflection paths. Excitingly, the proposed 3DLA NLOS correction method achieves a much more reliable performance. As shown in Table. 5.3, the 3DLA method achieves high correction availability and strong consistency between predicted and actual observation errors across numerous epochs. For satellite 17, the availability of 3DMA GNSS NLOS correction stands at 27.7%, and the mean correction error is 9.8 meters, with a standard deviation of 10.1 meters, while the 3DLA achieves an availability of 95.7% with a mean correction error of 2.9 meters and a standard deviation of 3.4 meters.

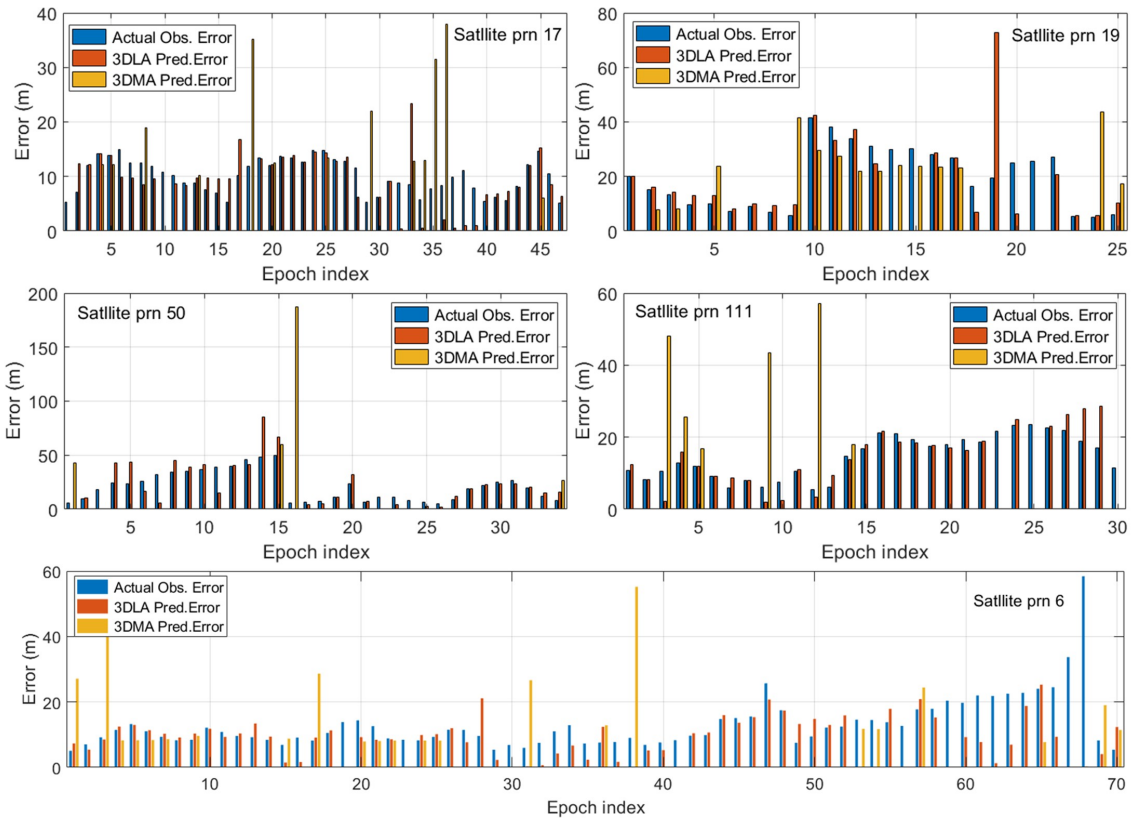

Figure 5.12: Individual demonstration of the observation error and correction of selected satellites in Urban Canyon 1. The actual observation error (Actual Obs. Error) and the predicted error for correction among epochs by 3DMA (3DMA Pred. Error) and the proposed 3DLA (3DLA Pred. Error) methods are presented.

To better visualize and analyze the correction result for individual receptions, we illustrate the restored signal transmission paths of selected satellites within the 3D PCM in Fig. 5.13. For Satellite 19 at epoch 10, the reception is identified as NLOS with an observation error of 41.6 meters and an elevation angle of 39.5 degrees, while the proposed 3DLA method successfully corrects the error, reducing the final error to 0.8 meters. The predicted reflection path by the 3DLA method is depicted in Fig. 5.13(a). The white line represents the blocked LOS transmission path (denoted as the LOS signal), and the green and blue lines depict the estimated DOA directions. Based on the DOA directions, the reflection path (denoted as the NLOS signal) and the reflection point (red line and dot, respectively) are reconstructed. The figure

clearly shows that the LOS transmission path is obstructed by a building. It is noticed that both estimated DOAs form large included angles with the LOS direction. This indicates the building facade is not parallel to the direction of receiver velocity, which is proved by the PCM data. Fig. 5.13(b) shows another correction for satellite 6 with a 47-degree elevation angle, where the building facade is approximately parallel to the driving direction and the LOS is collinear to one of the estimated DOAs.

In Fig. 5.12, we can also observe instances where the predicted observation error obtained by the proposed method deviates from the actual ones. Most of the unsuccessful correction cases are due to multipath reception. Notably, Doppler observations are reliable only in specific multipath scenarios, such as when there is one direct signal and one reflected signal, and the vehicle's velocity direction is parallel to the building facades [109]. In other cases, Doppler observations are greatly biased and DOA estimation is no longer valid. Therefore, the proposed method cannot accurately predict the multipath error or even the correction result is not available. An example is shown in Fig. 5.13(c), where satellite 6 experiences multipath reception consisting of a direct signal and a reflected signal while the vehicle is driving along the street. Considering that the velocity of the vehicle is parallel to the facade of the building, we can see the collineation of the red and green lines in the figure (with the angle difference between the original LOS and the estimated DOA being 1.2 degrees). The error prediction of the reflected signal by the proposed method is 12.3 meters while the true observation error is 5.3 meters. This indicates that, although we cannot accurately predict the observation error, the signal transmission paths of a multipath reception with a direct signal and a reflected signal can be reliably restored when the moving direction of the receiver is parallel to the street by the proposed method.

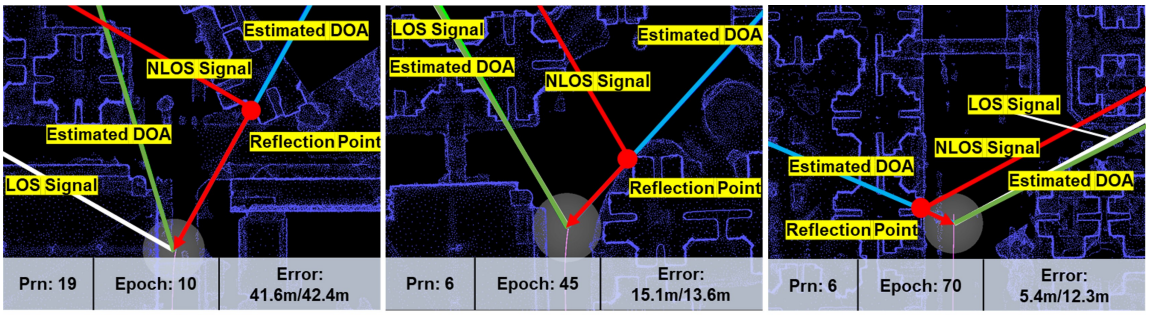

Figure 5.13: The demonstration of the reflection restoration by the proposed method with the 3D PCM in Urban Canyon 1 in top view. The white line denotes the LOS path, the green and blue lines are predicted signal DOA by the proposed method. The red line represents the predicted signal transmission path by the proposed method. The error compares the actual observation error with predicted error by the proposed method.

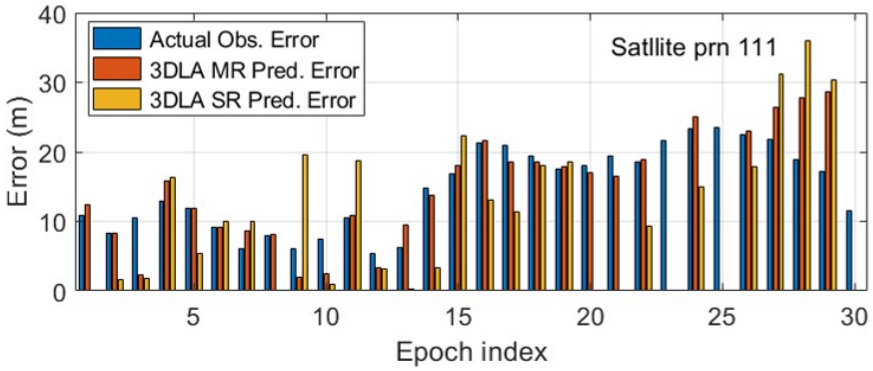

Figure 5.14: Demonstration of the observation error and correction of satellite 111 with and without the multi-ray tracking strategy.

Evaluation for Multi-ray Searching

In this section, we provide the experimental evaluation of the multi-ray search for reflection point determination. We take satellite 111 as an example, Fig. 15 demonstrates the comparison of NLOS correction results using the proposed method with multi-ray tracking (3DLA MR) and with only single-ray tracking (3DLA SR). Compared with 3DLA MR, the 3DLA SR shows both lower availability and larger inconsistency between actual observation error and prediction. For example, in epochs

1, 8, 20, and 21, 3DLA SR fails to provide valid correction solutions. In epochs 2, 5, 9, 11, 14, 16, 17, 22, and 24, the observation error predicted by 3DLA SR shows larger differences compared with the actual observation error. This is due to artifacts by dynamic objects, incorrect handling of signal penetration, inaccurate model, and DOA estimation bias. On the one hand, searching along a single line can fail to determine the reflection point due to artifacts and signal penetration, in turn, the NLOS correction cannot be obtained. On the other hand, when the building facade is irregular, a small DOA estimation bias or model reconstruction inaccuracy can affect the determination of the reflection point, causing errors in NLOS correction. The proposed multi-ray searching strategy leverages the environmental similarities within a small region to generate additional reflection point candidates and employs residual checks to select the most probable reflection point for NLOS correction. As demonstrated in Fig. 5.14, the 3DLA MR method outperforms 3DLA SR, achieving better availability and accuracy for NLOS correction.

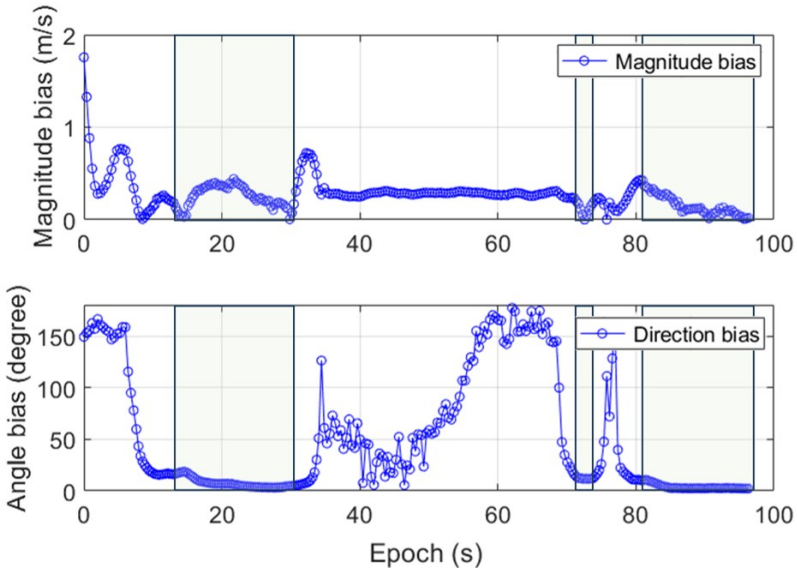

Figure 5.15: The illustration of velocity initialization bias with GLIO. The upper part shows the magnitude bias while the direction bias is depicted at the bottom. Green boxes denote the driving period.

5.3.3 NLOS Correction Evaluation in Urban Canyon 2

We further evaluate the NLOS correction performance of the proposed method in Urban Canyon 2, an area characterized by narrower streets and much taller buildings, as depicted in Fig. 5.6. Fig. 5.15 and Tab. 5.4 V provide the accuracy of velocity initialization and how it varies during the experiment. Fig. 5.16 compares the CDF of actual observation error and the predicted observation error using 3DMA and the proposed 3DLA methods. The initialization of the 3DMA method is based on the ground truth position. The results show that approximately 66% of the NLOS observations exhibit errors exceeding 20 meters. In this scenario, the conventional 3DMA GNSS NLOS correction method produces limited NLOS correction results. In contrast, the proposed method provides reliable correction performance, the percentage of observations with errors exceeding 20 meters decreasing from 66% to 30%.

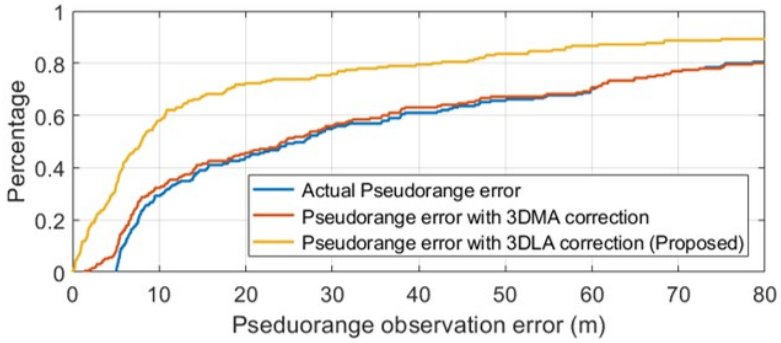

Figure 5.16: The CDF of the actual observation error (double-difference pseudorange error labeled by ground truth position) and observation error after NLOS correction, including 3DMA-based and the proposed 3DLA-based methods. The actual observation error is depicted by dark blue, the corrected CDF of 3DMA and the proposed 3DLA method are given as red and orange curves, respectively.

Table 5.4: Velocity Estimation Results (Mag. MEAN: Mean Velocity Magnitude Bias, Mag. MAX: Maximum of Velocity Magnitude Bias, Ang. MEAN: Mean Velocity Directional Bias, Ang. MAX: Maximum of Velocity Directional Bias)

Mag. MEAN (m/s)	**Mag. MAX** (m/s)	**Ang. MEAN** (degree)	**Ang. MAX** (degree)
0.16	0.44	3.54	7.02

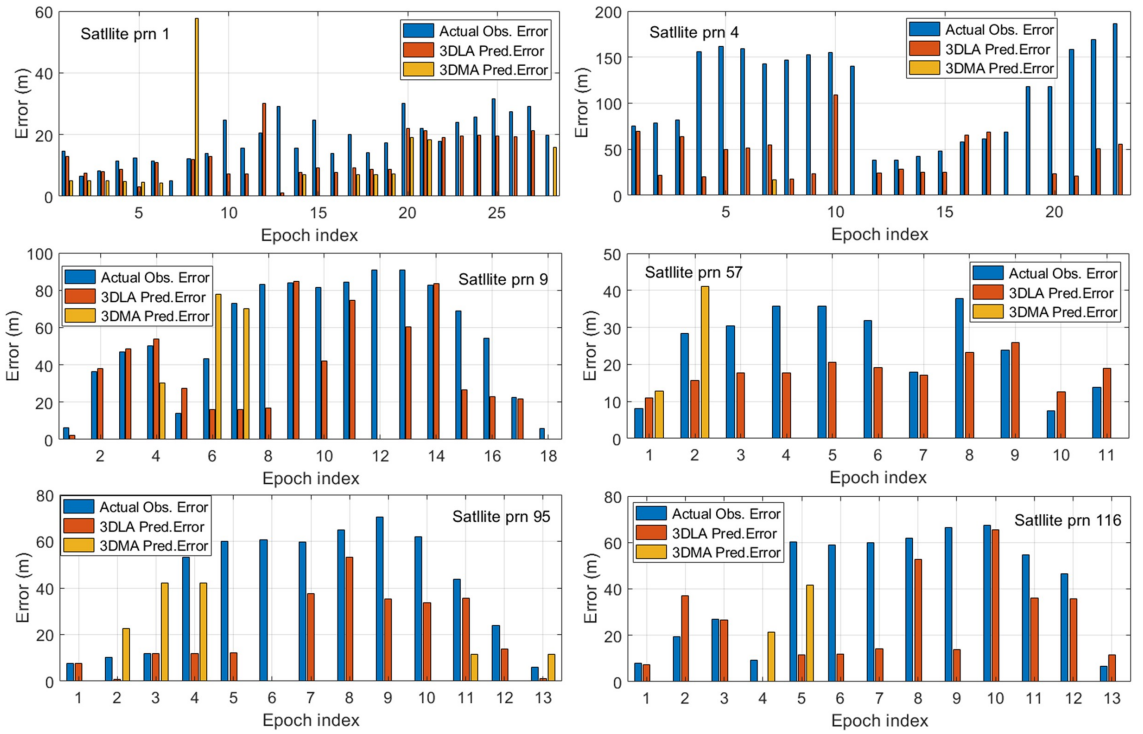

Figure 5.17: Individual demonstration of the observation error and correction of selected satellites in Urban Canyon 2. The actual observation error (Actual Obs. Error) and the predicted error for correction among epochs by 3DMA (3DMA Pred. Error) and the proposed 3DLA (3DLA Pred. Error) methods are presented.

Fig. 5.17 presents the predicted observation error of 3DMA and 3DLA methods with a comparison to the actual observation error for selected satellites. A statistical comparison is provided in Table. 5.5. The results indicate a notable decrease in correction availability for the conventional 3DMA method in Urban Canyon 2 compared to Urban Canyon 1. Furthermore, the 3DMA method demonstrates low correction accuracy, as evidenced by the significant deviations between its predicted error and the actual observation error. In contrast, the proposed 3DLA NLOS correction method achieves more reliable performance with higher availability and accuracy. Notably, accurate corrections are observed for NLOS receptions with significant errors, such as satellite 9 in epochs 2, 3, 4, 9, and 14, and satellite 116 in epochs 3 and 10. Fig. 5.18 provides a visualization of these correction results.

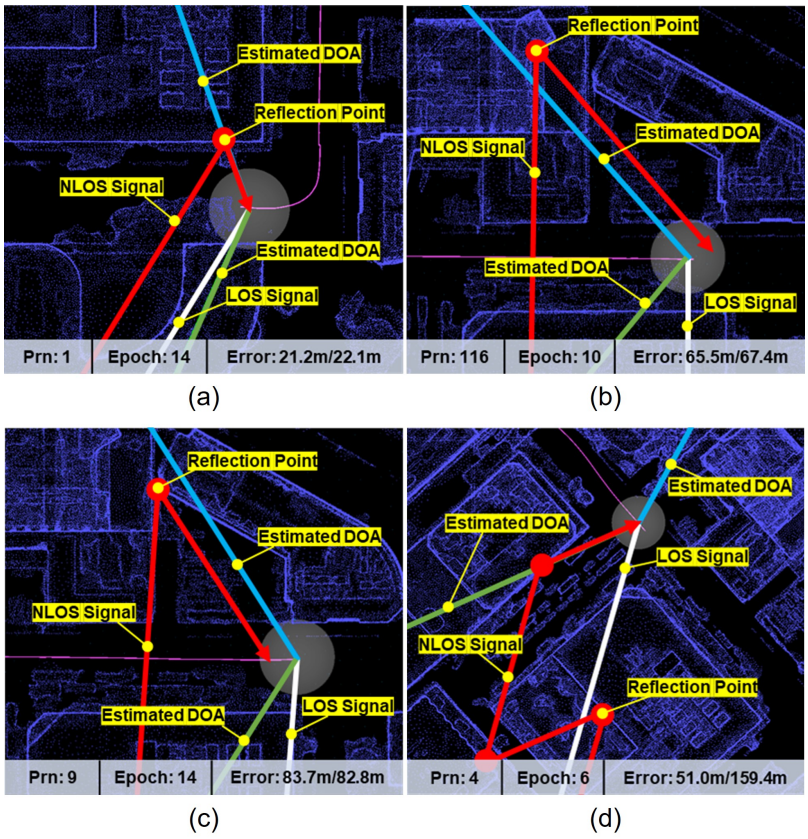

Figure 5.18: The demonstration of the reflection restoration by the proposed method with the 3D PCM in Urban Canyon 2 in top view. The white line denotes the LOS path, the green and blue lines are predicted signal DOA by the proposed method. The red line represents the predicted signal transmission path by the proposed method. The error compares the actual observation error with predicted error by the proposed method.

Many NLOS receptions with large observation errors remain uncorrected. For instance, satellite 4 exhibits severe NLOS receptions during the experiment, with the maximum error reaching up to 180 meters. The proposed 3DLA method fails to identify reflection paths matching the actual observed error in most epochs. In these cases, the identified reflection points are still occluded by the point cloud of buildings along the signal transmission path toward the satellite, suggesting the presence of multi-reflection. We trace the signal from the obtained reflection point with a 3D building model using reflection law to explore the potential subsequent reflection

Table 5.5: Overview of the NLOS Correction Result for Selected Satellites (PRN: Pseudorandom Noise Code, Ele.: Elevation Angle of the Satellite, MCE: Mean Correction Error, STD.: Standard Deviation of MCE. Avail.: Availability of the NLOS Correction Result. 3DLA. and 3DMA.: Correction Result by the 3DMA Method and 3DLA Method, respectively)

PRN		**1**	**4**	**9**	**57**	**95**	**116**
Ele. (degree)		42	20	28	41	49	51
3DMA	MCE (m)	15.8	110.3	50.6	22.9	38.5	39.0
	STD (m)	10.8	49.4	33.1	12.1	24.9	23.9
	Avail.	50.0%	4.3%	16.6%	18.8%	38.4%	20.0%
3DLA	MCE (m)	7.4	74.5	**23.8**	9.2	**21.5**	**20.5**
	STD (m)	6.6	**52.0**	**26.6**	**6.1**	**19.5**	**20.2**
	Avail.	**92.8%**	**86.9%**	**94.4%**	**100.0%**	**92.3%**	**93.3%**

points for multiple reflections, as depicted in Fig. 5.18(d). The analysis reveals a triple reflection, with a predicted observation error exceeding 160 meters, which closely matches the actual observation error. This further validates the effectiveness of DOA estimation in the proposed method.

5.3.4 Positioning Performance Evaluation Using the Proposed 3DLA NLOS Correction

To demonstrate how the proposed method can help with positioning performance with NLOS correction, the following methods are evaluated and compared qualitatively and quantitatively in multiple aspects in Urban Canyon 1 and Urban Canyon 2. The mean error, maximum error, and standard deviation in both 2D and 3D cases are compared. The evaluated methods are listed as follows:

(a) **LC-GNSS-LIO:** A loosely-coupled GNSS/LIO integration system (LIO-SAM) [28] fusing position-level GNSS solutions and LIO solutions. RTKLIB [108] is used to obtain DGNSS solutions with filter type settings to "combined" and RAIM FDE enabled.

(b) **GLIO:** A tightly-coupled GNSS/LiDAR/INS integration system [1] using original GNSS raw measurements.

(c) **GLIO-COR:** GLIO with corrected GNSS raw measurements, which can demonstrate the effectiveness of the proposed NLOS correction method.

Table. 5.6 provides the evaluation results. The first epoch of the trajectory is fixed for all three methods. The trajectory and positioning errors in 2D and 3D for the evaluation in Urban Canyon 1 are given in Fig. 5.19. The 2D positioning performance of the LC-GNSS-LIO demonstrated a mean error of 4.2 meters, with a maximum error of 6.6 meters, and a standard deviation of 1.5 meters, while the 3D positioning results show a mean error of 7.0 meters, a maximum error of 12.5 meters, and a standard deviation of 3.8 meters. At the start and end points of the trajectory, the vehicle traverses through open intersections where the GNSS observation quality is significantly higher compared to other segments. This is reflected in the relatively lower errors of the trajectory in these regions. In contrast, the middle portion of the trajectory features a more complex environment, where GNSS observations become unreliable. With the application of a filter-based GNSS positioning method [108] with Fault Detection and Exclusion (FDE) and forward-backward filtering, the resulting GNSS positioning solutions still exhibit substantial errors.

Table 5.6: Positioning Performance of the Evaluated Methods in Urban Canyon 1 (2D MEAN and 3D MEAN: 2D and 3D Positioning Errors in Meters. IMPR.: Improvement Calculated based on GLIO Results. STD: Standard Deviation. MAX: Maximum Error)

ALL DATA	**Urban Canyon 1**			**Urban Canyon 2**		
	LC-GNSS-LIO	GLIO	GLIO-COR	LC-GNSS-LIO	GLIO	GLIO-COR
2D MEAN (m)	4.2	2.8	**2.6**	9.0	**1.5**	1.6
2D MAX (m)	6.6	4.1	**3.9**	16.5	**4.3**	4.7
2D STD (m)	1.5	0.9	**0.7**	4.5	**0.7**	0.9
3D MEAN (m)	7.0	9.8	**4.3**	9.2	5.1	**3.2**
3D MAX (m)	12.5	15.9	**8.0**	17.0	8.2	**5.8**
3D STD (m)	3.8	3.9	**1.6**	4.7	2.1	**1.3**

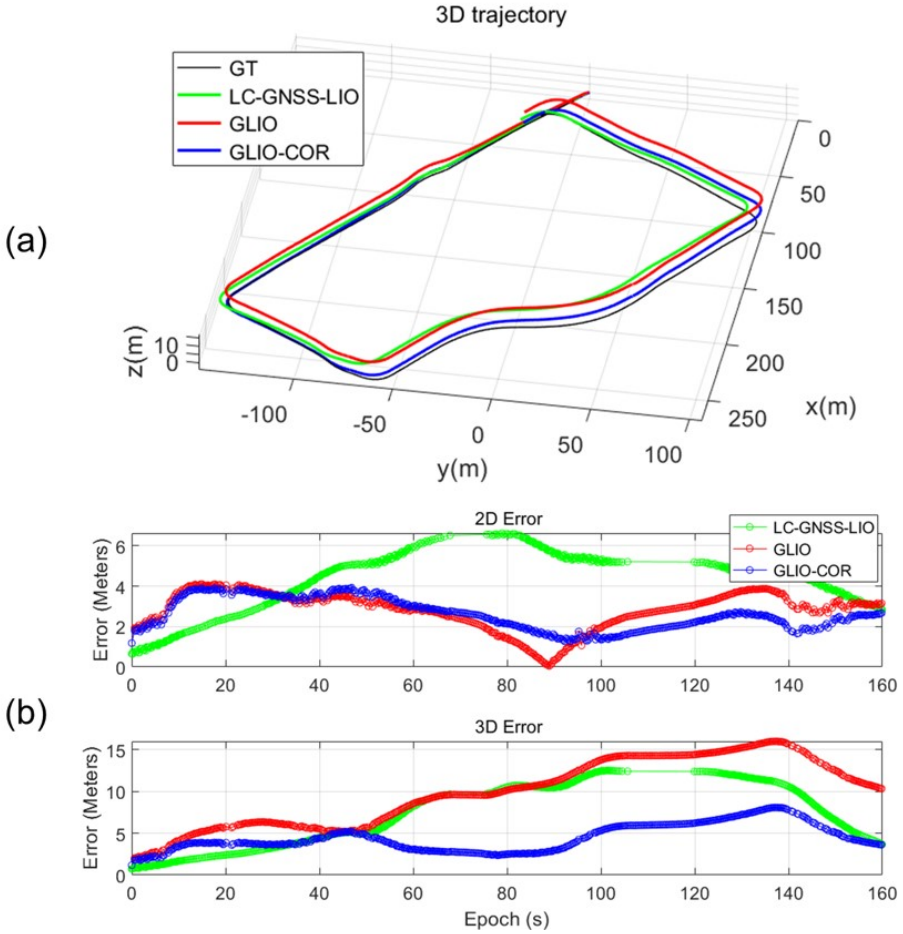

Figure 5.19: The comparison of the trajectory and positioning error in Urban Canyon 1.

The loosely coupled system also demonstrates relatively large errors in this segment. Using raw GNSS measurement, GLIO achieves 2.8 meters horizontal positioning accuracy with maximum positioning error reaching 4 meters, which is greatly improved compared with the loosely coupled method. However, the 3D positioning accuracy only achieves 9.8 meters with a maximum error reaching 15.9 meters. We can observe that the GLIO trajectory shows an obvious drift at the Z axis due to severe NLOS receptions. By utilizing the proposed 3DLA NLOS correction method to improve the quality of the original GNSS observations, the GLIO-COR finally improves the 2D positioning accuracy to 2.6 meters, and more importantly, the 3D

positioning accuracy reaches 4.3 meters, with a maximum error of 8.0 meters. The trajectory of GLIO-COR illustrates that the drift in the vertical direction is effectively reduced, which means the proposed method accurately corrected a considerable part of the polluted GNSS receptions.

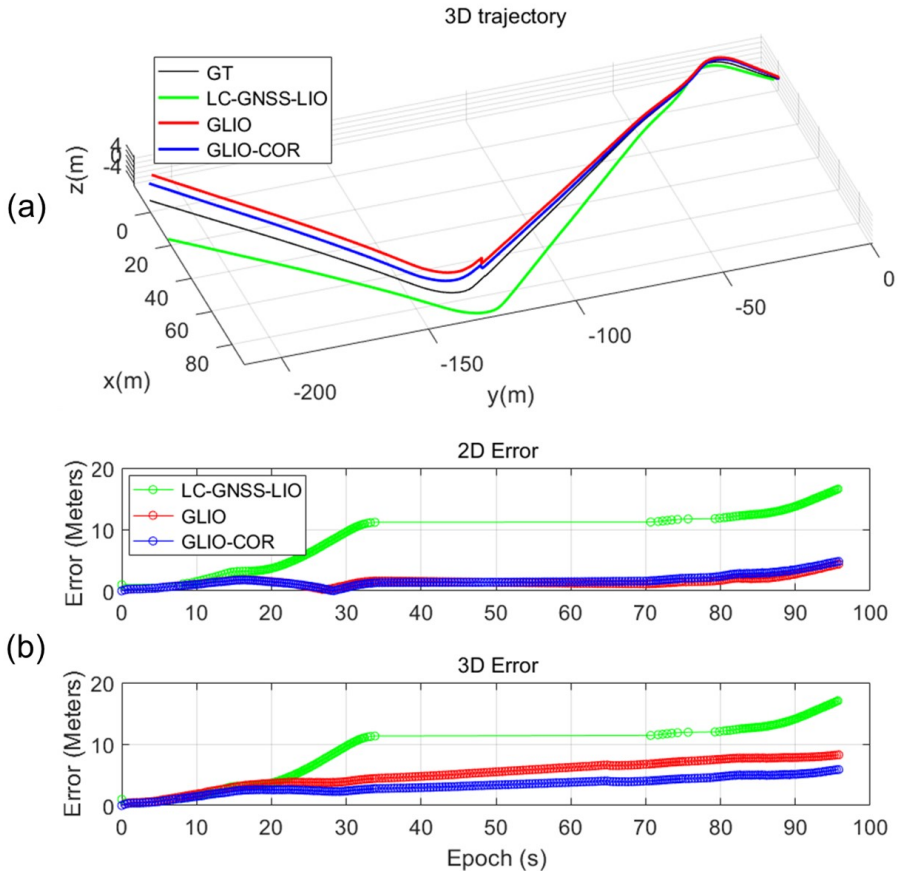

Figure 5.20: The comparison of the trajectory and positioning error in Urban Canyon 2.

Fig. 5.20 shows the 3D trajectory and error curves of the three methods in Urban Canyon 2. Due to a further reduction in the availability of healthy GNSS observations, the standalone GNSS positioning solution shows a significant decline in availability. Moreover, the errors associated with the available GNSS solutions remain substantial. As a result, large trajectory errors of the loosely coupled method can be observed. GLIO obtains a 1.5 meters 2D mean error and a 5.1 meters 3D

mean error. It should be noted that the corner in both trajectories is due to large observation errors during the parking period. After the NLOS correction by the proposed method, the 3D positioning accuracy of GLIO-COR shows improvement from 5.1 meters to 3.2 meters. However, the 2D positioning accuracy decreases and the 2D positioning error increases from 1.5 meters to 1.6 meters. It is observed that the GLIO-COR shows an obvious upward trend after 60 seconds, which is because multipath and multi-reflection receptions dominate the raw measurements. They are not effectively corrected by the proposed method.

5.3.5 Running Efficiency Analysis

In this section, we provide the processing time of the proposed method to illustrate its computational efficiency for real-time application. The evaluation is performed on a device with an i9-12900k CPU under single-thread operation. During the experimentation, the algorithm runtime mainly consists of two aspects: DOA estimation and NLOS correction formulation. In our evaluation, we set around 20 satellites for DOA estimation, it takes 0.8-1.1 ms for each epoch. Such efficiency is attributed to the proposed optimization-based estimator. The NLOS correction formulation includes multi-ray searching and reflection point determination, where multi-ray searching takes the most time consumption. For individual satellites where a reflection point cannot be identified, the computational overhead for multi-ray tracking is the highest, as finding the reflection point allows for the early termination of the process. Based on the experimental settings in this work, the maximum computational time for multi-ray tracking per satellite, in the absence of a reflection point, is approximately 12 ms. For cases where a reflection point is identified, the computational time ranges from 1 to 12 ms, with the majority being less than 5 ms. Considering that the number of satellites for which a reflection point cannot be determined is minimal, the average processing time per satellite is less than 10 ms. The improvement

of the running efficiency can be eplored by utilizing smaller or more sparse point cloud, which is a trade-off between the performance and the efficiency. Therefore, the proposed method achieves real-time performance and has the potential beneficial for real ITS applications in challenging environments.

5.4 Conclusion

GNSS positioning has long suffered from NLOS receptions in urbanized areas. The conventional NLOS correction methods utilize a 3D model or 3D LiDAR to predict the signal transmission. However, their reliance on the shortest path assumption places difficulty in the accurate restoration of the true reflection, let alone precisely correct the NLOS observation. In this chapter, a 3D LiDAR-aided GNSS NLOS correction method is proposed, which: (1) develops a 3D LiDAR-aided GNSS DOA estimator using Doppler measurement together with the evaluation of the impact of velocity bias on DOA estimation, (2) proposes a NLOS correction method using the estimated DOA and the surrounding PCM, which includes multi-ray tracking and residual-based evaluation to effectively improve the robustness of reflection point determination, and thus improve the NLOS correction performance. The experiment evaluates the effectiveness of the proposed method in two challenging sequences in Hong Kong, which shows a much more reliable NLOS correction performance compared with the representative 3DMA method. Overall, more than 90% correction availability is achieved, and the observation accuracy of NLOS receptions improves significantly as the reflection transmission path is reliably restored. With the reception corrections by the proposed method, the 3D positioning errors of the GNSS/LiDAR/INS integrated positioning decrease from 9.8 meters to 4.3 meters in Urban Canyon 1, and from 5.1 meters to 3.7 meters in Urban Canyon 2.

Chapter 6

Conclusions and Future Work

This dissertation investigates the integration of LiDAR with GNSS to improve positioning accuracy and robustness in urban environments, where signal blockage and multipath effects often degrade GNSS performance. Specifically, three key studies are conducted: (1) 3D LiDAR aided NLOS detection and a computationally efficient tightly-coupled GNSS/LiDAR integration framework; (2) a globally consistent factor graph-based method for tightly-coupled GNSS/LiDAR/IMU fusion; and (3) a novel approach that incorporates LiDAR-derived motion and Doppler measurements for signal DOA-aided NLOS correction. Together, these contributions enhances the positioning performance of autonomous systems in urban areas. Moreover, extension works and potential future research directions will be discussed afterwards.

6.1 Conclusion of this Research

In Chapter 3, we presented a LiDAR-aided GNSS positioning framework that integrates NLOS exclusion and VS-aided geometry improvement within a FGO pipeline. The system leverages local PCM to represent the environments and predict the satellite visibility with intersection detection. To improve the robustness of NLOS detection, PGO is introduced to correct the historical states and local PCM is constantly updated. Another key contribution includes using selected dlow-lying LiDAR fea-

tures as virtual-satellites to improve the poor satellite geometry in the tightly-coupled integration framework. The feature selection contributes the computational efficiency of the estimator while maintain a similar positioning accuracy. This chapter demonstrates a complete pipeline from 3D LiDAR-aided GNSS raw data preprocessing to tightly-coupled GNSS-RTK/LiDAR integration with ambiguity resolution. Experimental results on three challenging urban sequences in Hong Kong demonstrate that the system achieves real-time performance and delivers enhanced positioning accuracy and robustness using commercial-grade GNSS and LiDAR/IMU sensors.

In chapter 4, we addressed a key limitation in existing multi-sensor fusion methods—the lack of consistency across different sensing modalities—by proposing a tightly-coupled GNSS/LiDAR/IMU odometry framework. The system performs tight integration of raw GNSS, LiDAR, and IMU measurements through a two-stage FGO architecture, comprising a sliding-window-based frontend and a batched backend. Within this architecture, different LiDAR constraints are employed: a scan-to-map approach in the frontend ensures local accuracy during GNSS degradation, while a scan-to-multi-scan scheme in the backend promotes global consistency between LiDAR and GNSS constraints. The proposed method enables the system to generate efficient, robust, and consistent state estimates across all sensor sources. Experimental results on multiple challenging urban sequences in Hong Kong demonstrate that the proposed method achieves high-accuracy, real-time positioning using only commercial-grade GNSS receivers and LiDAR/IMU sensors, even under severe urban signal degradation. Moreover, the full algorithm has been open-sourced and released on GitHub, where it has been widely recognized and adopted by researchers and developers in different communities.

In chapter 5, we tackled a core limitation in existing GNSS NLOS correction methods—their reliance on the shortest-path assumption, which often leads to incorrect identification of reflection points and inaccurate correction of NLOS obser-

vations in urban environments. To overcome this, we proposed a 3D LiDAR-aided GNSS NLOS correction framework that leverages Doppler-based DOA estimation. First, we introduce a DOA estimator using Doppler measurements with LiDAR-derived motion information, and assess the influence of velocity bias on DOA accuracy. Secondly, we develop a correction pipeline based on estimated DOA and the surrounding 3D PCM, employing multi-ray tracking and residual-based validation to robustly identify true reflection points. Evaluations on two urban canyon sequences in Hong Kong demonstrate that the proposed approach achieves over 90% correction availability and significantly enhances the quality of NLOS observations. With more accurate reception corrections, the integrated GNSS/LiDAR/IMU positioning error is reduced from 9.8m to 4.3m in Urban Canyon 1, and from 5.1m to 3.7m in Urban Canyon 2, highlighting the method's practical effectiveness in addressing signal degradation in dense urban areas.

6.2 Future Directions

While this dissertation presents a comprehensive framework for 3D LiDAR-aided GNSS positioning in urban environments, several challenges remain unresolved, offering promising directions for future research. These challenges span from raw data quality and signal modeling to optimization strategies and system scalability. Specifically, future work can focus on the following aspects:

1. Multipath reception detection and correction. Although the proposed framework effectively detects and corrects NLOS signals, multipath receptions—especially those resulting from short-delay single or multiple reflections—remain a dominant source of residual error. Unlike NLOS signals, multipath is more subtle and difficult to detect through LiDAR occlusion checks or signal geometry alone. A promising approach involves leveraging optimization residuals to identify multipath-

affected observations after NLOS signals have been processed. Developing principled models for multipath reflections and integrating them into the factor graph could further improve system robustness and accuracy.

2. Multi-reflection modeling using point cloud semantics The current framework assumes at most one dominant reflection per signal path, which may not hold in dense urban environments where multi-reflection paths (e.g., glass–concrete–glass) are common. Future research can explore planar extraction from point cloud maps and implement a "shoot-and-bounce" strategy to simulate signal propagation across multiple surfaces. This would enable multi-reflection path reconstruction, improving correction accuracy and reducing residual error in severe multipath scenarios.

3. Generalization to PPP and GNSS signal recovery. While RTK enables high-precision positioning with relative corrections, it requires local base stations and may not generalize to large-scale deployments. Future work can investigate the integration of the proposed 3D LiDAR-aided signal processing techniques with Precise Point Positioning (PPP) to enable infrastructure-independent high-accuracy GNSS positioning. In addition, point cloud information can be leveraged not just for pseudorange observations, but for reconstructing corrupted or ambiguous raw GNSS carrier observations, thereby improving the quality of the input data itself. This direction opens the possibility for GNSS signal restoration using spatial priors, fundamentally enhancing measurement reliability in urban canyons.

Bibliography

[1] X. Liu, W. Wen, and L.-T. Hsu, "GLIO: Tightly-coupled GNSS/LiDAR/IMU integration for continuous and drift-free state estimation of intelligent vehicles in urban areas," *IEEE Transactions on Intelligent Vehicles*, vol. 9, no. 1, pp. 1412–1422, 2023.

[2] J. Zhang, X. Liu, W. Wen, and L.-T. Hsu, "Safety-Quantifiable Planar-Feature-based LiDAR Localization with a Prior Map for Intelligent Vehicles in Urban Scenarios," *IEEE Transactions on Intelligent Vehicles*, 2024.

[3] X. Liu, W. Wen, and L.-T. Hsu, "3d LiDAR aided GNSS real-time kinematic positioning via coarse-to-fine batch optimization for high accuracy mapping in dense urban canyons," in *Proceedings of the 35th International Technical Meeting of the Satellite Division of The Institute of Navigation (ION GNSS+ 2022)*, 2022, pp. 1954–1965.

[4] Liu, Xikun and Wen, Weisong and Hsu, Li-Ta, "3d LiDAR Aided GNSS NLOS Correction with Direction of Arrival Estimation Using Doppler Measurements," in *Proceedings of the 36th International Technical Meeting of the Satellite Division of The Institute of Navigation (ION GNSS+ 2023)*, 2023, pp. 2206–2216.

[5] D. C. Tsouros, S. Bibi, and P. G. Sarigiannidis, "A review on UAV-based applications for precision agriculture," *Information*, vol. 10, no. 11, p. 349, 2019.

[6] L. Chen, Y. Li, C. Huang, B. Li, Y. Xing, D. Tian, L. Li, Z. Hu, X. Na, Z. Li *et al.*, "Milestones in autonomous driving and intelligent vehicles: Survey of surveys," *IEEE Transactions on Intelligent Vehicles*, vol. 8, no. 2, pp. 1046–1056, 2022.

[7] M. B. Alatise and G. P. Hancke, "A review on challenges of autonomous mobile robot and sensor fusion methods," *IEEE access*, vol. 8, pp. 39 830–39 846, 2020.

[8] A. Couturier and M. A. Akhloufi, "A review on absolute visual localization for UAV," *Robotics and Autonomous Systems*, vol. 135, p. 103666, 2021.

[9] S. Kuutti, S. Fallah, K. Katsaros, M. Dianati, F. Mccullough, and A. Mouzakitis, "A survey of the state-of-the-art localization techniques and their potentials for autonomous vehicle applications," *IEEE Internet of Things Journal*, vol. 5, no. 2, pp. 829–846, 2018.

[10] T. Qin, P. Li, and S. Shen, "Vins-mono: A robust and versatile monocular visual-inertial state estimator," *IEEE transactions on robotics*, vol. 34, no. 4, pp. 1004–1020, 2018.

[11] J. Zhang, S. Singh *et al.*, "LOAM: Lidar odometry and mapping in real-time." in *Robotics: Science and systems*, vol. 2, no. 9. Berkeley, CA, 2014, pp. 1–9.

[12] F. Huang, W. Wen, J. Zhang, and L.-T. Hsu, "Point wise or feature wise? a benchmark comparison of publicly available LiDAR odometry algorithms in urban canyons," *IEEE Intelligent Transportation Systems Magazine*, vol. 14, no. 6, pp. 155–173, 2022.

[13] J. A. del Peral-Rosado, R. Raulefs, J. A. López-Salcedo, and G. Seco-Granados, "Survey of cellular mobile radio localization methods: From 1g to 5g," *IEEE Communications Surveys & Tutorials*, vol. 20, no. 2, pp. 1124–1148, 2017.

[14] E. D. Kaplan and C. Hegarty, *Understanding GPS/GNSS: principles and applications*. Artech house, 2017.

[15] C. C. Counselman and S. A. Gourevitch, "Miniature interferometer terminals for earth surveying: ambiguity and multipath with Global Positioning System," *IEEE Transactions on Geoscience and Remote Sensing*, no. 4, pp. 244–252, 1981.

[16] P. K. Enge, "The global positioning system: Signals, measurements, and performance," *International Journal of Wireless Information Networks*, vol. 1, pp. 83–105, 1994.

[17] P. J. Teunissen, "Least-squares estimation of the integer GPS ambiguities," in *Invited lecture, section IV theory and methodology, IAG general meeting, Beijing, China*, 1993, pp. 1–16.

[18] X.-W. Chang, X. Yang, and T. Zhou, "MLAMBDA: A modified LAMBDA method for integer least-squares estimation," *Journal of geodesy*, vol. 79, no. 9, pp. 552–565, 2005.

[19] P. Groves, "Multipath vs. NLOS signals," *Inside GNSS*, vol. 8, no. 6, pp. 40–42, 2013.

[20] W. Wen, G. Zhang, and L.-T. Hsu, "Correcting NLOS by 3d LiDAR and building height to improve GNSS single point positioning," *Navigation*, vol. 66, no. 4, pp. 705–718, 2019.

[21] W. W. Wen, G. Zhang, and L.-T. Hsu, "GNSS NLOS exclusion based on dynamic object detection using LiDAR point cloud," *IEEE transactions on intelligent transportation systems*, vol. 22, no. 2, pp. 853–862, 2019.

[22] W. W. Wen and L.-T. Hsu, "3d LiDAR aided GNSS NLOS mitigation in urban canyons," *IEEE Transactions on Intelligent Transportation Systems*, vol. 23, no. 10, pp. 18 224–18 236, 2022.

[23] W. Wen and L.-T. Hsu, "3d LiDAR aided GNSS real-time kinematic positioning," in *Proceedings of the 34th International Technical Meeting of the Satellite Division of The Institute of Navigation (ION GNSS+ 2021)*, 2021, pp. 2212–2220.

[24] W. Wen, G. Zhang, and L.-T. Hsu, "Exclusion of GNSS NLOS receptions caused by dynamic objects in heavy traffic urban scenarios using real-time 3d point cloud: An approach without 3d maps," in *2018 IEEE/ION Position, Location and Navigation Symposium (PLANS)*. IEEE, 2018, pp. 158–165.

[25] W. Wen, "3d LiDAR aided GNSS and its tightly coupled integration with INS via factor graph optimization," in *Proceedings of the 33rd International Technical Meeting of the Satellite Division of The Institute of Navigation (ION GNSS+ 2020)*, 2020, pp. 1649–1672.

[26] X. Li, H. Yu, X. Wang, S. Li, Y. Zhou, and H. Chang, "FGO-GIL: Factor graph optimization-based GNSS RTK/INS/LiDAR tightly coupled integration for precise and continuous navigation," *IEEE Sensors Journal*, vol. 23, no. 13, pp. 14 534–14 548, 2023.

[27] D. He, H. Li, and J. Yin, "LIGO: A Tightly Coupled LiDAR-Inertial-GNSS Odometry Based on a Hierarchy Fusion Framework for Global Localization With Real-Time Mapping," *IEEE Transactions on Robotics*, 2025.

[28] T. Shan, B. Englot, D. Meyers, W. Wang, C. Ratti, and D. Rus, "Lio-sam: Tightly-coupled lidar inertial odometry via smoothing and mapping," in *2020 IEEE/RSJ international conference on intelligent robots and systems (IROS)*. IEEE, 2020, pp. 5135–5142.

[29] W. Xu, Y. Cai, D. He, J. Lin, and F. Zhang, "Fast-lio2: Fast direct lidar-inertial odometry," *IEEE Transactions on Robotics*, vol. 38, no. 4, pp. 2053–2073, 2022.

[30] K. Li, M. Li, and U. D. Hanebeck, "Towards high-performance solid-state-lidar-inertial odometry and mapping," *IEEE Robotics and Automation Letters*, vol. 6, no. 3, pp. 5167–5174, 2021.

[31] C. Xia, X. Li, F. He, S. Li, and Y. Zhou, "Accurate and Rapidly-Convergent GNSS/INS/LiDAR Tightly-Coupled Integration via Invariant EKF Based on

Two-Frame Group," *IEEE Transactions on Automation Science and Engineering*, 2024.

[32] T. Li, L. Pei, Y. Xiang, X. Zuo, W. Yu, and T.-K. Truong, "P 3-LINS: Tightly coupled PPP-GNSS/INS/LiDAR navigation system with effective initialization," *IEEE Transactions on Instrumentation and Measurement*, vol. 72, pp. 1–13, 2023.

[33] X. Liu, W. Wen, F. Huang, H. Gao, Y. Wang, and L.-T. Hsu, "3d LiDAR aided GNSS NLOS mitigation for reliable GNSS-RTK positioning in urban canyons," *arXiv preprint arXiv:2212.05477*, 2022.

[34] A. Vu, A. Ramanandan, A. Chen, J. A. Farrell, and M. Barth, "Real-time computer vision/DGPS-aided inertial navigation system for lane-level vehicle navigation," *IEEE Transactions on Intelligent Transportation Systems*, vol. 13, no. 2, pp. 899–913, 2012.

[35] L. Zhang, H.-F. Ng, G. Zhang, and L.-T. Hsu, "Ray-tracing correction for gnss velocity estimation using doppler frequency: A feasibility analysis," *IEEE Transactions on Instrumentation and Measurement*, 2024.

[36] J. Blanch, T. Walter, and P. Enge, "Fast multiple fault exclusion with a large number of measurements," in *Proceedings of the 2015 International Technical Meeting of the Institute of Navigation*, 2015, pp. 696–701.

[37] L.-T. Hsu, H. Tokura, N. Kubo, Y. Gu, and S. Kamijo, "Multiple faulty GNSS measurement exclusion based on consistency check in urban canyons," *IEEE Sensors Journal*, vol. 17, no. 6, pp. 1909–1917, 2017.

[38] R. G. Brown, "A baseline GPS RAIM scheme and a note on the equivalence of three RAIM methods," *Navigation*, vol. 39, no. 3, pp. 301–316, 1992.

[39] Y. Liu, S. Li, Q. Fu, Z. Liu, and Q. Zhou, "Analysis of Kalman filter innovation-based GNSS spoofing detection method for INS/GNSS integrated navigation system," *IEEE Sensors Journal*, vol. 19, no. 13, pp. 5167–5178, 2019.

[40] Y. Yang and J. Xu, "GNSS receiver autonomous integrity monitoring (RAIM) algorithm based on robust estimation," *Geodesy and geodynamics*, vol. 7, no. 2, pp. 117–123, 2016.

[41] S. Hewitson and J. Wang, "Extended receiver autonomous integrity monitoring (e raim) for gnss/ins integration," *Journal of Surveying Engineering*, vol. 136, no. 1, pp. 13–22, 2010.

[42] Hewitson, Steve and Wang, Jinling, "GNSS receiver autonomous integrity monitoring (RAIM) performance analysis," *Gps Solutions*, vol. 10, pp. 155–170, 2006.

[43] T. Walter, J. Blanch, M. J. Choi, T. Reid, and P. Enge, "Incorporating GLONASS into aviation RAIM receivers," in *Proceedings of the 2013 international technical meeting of the institute of navigation*, 2013, pp. 239–249.

[44] T. Walter, J. Blanch, P. Enge, B. Pervan, and L. Gratton, "Future architectures to provide aviation integrity," in *Proceedings of the 2008 National technical Meeting of the Institute of Navigation*, 2008, pp. 394–401.

[45] A. Martineau, C. Macabiau, and M. Mabilleau, "GNSS RAIM assumptions for vertically guided approaches," in *Proceedings of the 22nd International Technical Meeting of the Satellite Division of The Institute of Navigation (ION GNSS 2009)*, 2009, pp. 2791–2803.

[46] S. Bhattacharyya and D. Gebre-Egziabher, "Kalman filter–based RAIM for GNSS receivers," *IEEE Transactions on Aerospace and Electronic Systems*, vol. 51, no. 3, pp. 2444–2459, 2015.

[47] A. Angrisano, S. Gaglione, and C. Gioia, "RAIM algorithms for aided GNSS in urban scenario," in *2012 Ubiquitous Positioning, Indoor Navigation, and Location Based Service (UPINLBS)*. IEEE, 2012, pp. 1–9.

[48] A. Angrisano and S. Gaglione, "Smartphone GNSS performance in an urban scenario with RAIM application," *Sensors*, vol. 22, no. 3, p. 786, 2022.

[49] L.-T. Hsu, Y. Gu, and S. Kamijo, "NLOS correction/exclusion for GNSS measurement using RAIM and city building models," *Sensors*, vol. 15, no. 7, pp. 17 329–17 349, 2015.

[50] X.-L. Su, X. Zhan, M. Niu, and Y. Zhang, "Receiver autonomous integrity monitoring (RAIM) performances of combined GPS/BeiDou/QZSS in urban canyon," *IEEJ Transactions on Electrical and Electronic Engineering*, vol. 9, no. 3, pp. 275–281, 2014.

[51] J. Blanch, A. Ene, T. Walter, and P. Enge, "An optimized multiple hypothesis RAIM algorithm for vertical guidance," in *Proceedings of the 20th International Technical Meeting of the Satellite Division of The Institute of Navigation (ION GNSS 2007)*, 2007, pp. 2924–2933.

[52] N. Zhu, J. Marais, D. Betaille, and M. Berbineau, "GNSS position integrity in urban environments: A review of literature," *IEEE Transactions on Intelligent Transportation Systems*, vol. 19, no. 9, pp. 2762–2778, 2018.

[53] D. Weng, Z. Hou, Y. Meng, M. Cai, and Y. Chan, "Characterization and mitigation of urban GNSS multipath effects on smartphones," *Measurement*, vol. 223, p. 113766, 2023.

[54] J. Blanch, T. Walter, P. Enge, S. Wallner, F. Amarillo Fernandez, R. Dellago, R. Ioannides, I. Fernandez Hernandez, B. Belabbas, A. Spletter *et al.*, "Critical Elements for a Multi-Constellation Advanced RAIM," *Navigation: Journal of The Institute of Navigation*, vol. 60, no. 1, pp. 53–69, 2013.

[55] J. Blanch, T. Walter, P. Enge, Y. Lee, B. Pervan, M. Rippl, and A. Spletter, "Advanced RAIM user algorithm description: Integrity support message processing, fault detection, exclusion, and protection level calculation," in *Proceedings of the 25th International Technical Meeting of The Satellite Division of the Institute of Navigation (ION GNSS 2012)*, 2012, pp. 2828–2849.

[56] T. Walter, J. Blanch, K. Gunning, M. Joerger, and B. Pervan, "Determination of fault probabilities for ARAIM," *IEEE transactions on aerospace and electronic systems*, vol. 55, no. 6, pp. 3505–3516, 2019.

[57] J. Blanch, T. Walker, P. Enge, Y. Lee, B. Pervan, M. Rippl, A. Spletter, and V. Kropp, "Baseline advanced RAIM user algorithm and possible improvements," *IEEE Transactions on Aerospace and Electronic Systems*, vol. 51, no. 1, pp. 713–732, 2015.

[58] H. Pesonen, "A framework for Bayesian receiver autonomous integrity monitoring in urban navigation," *Navigation*, vol. 58, no. 3, pp. 229–240, 2011.

[59] Q. Zhang and Q. Gui, "A new Bayesian RAIM for multiple faults detection and exclusion in GNSS," *The Journal of Navigation*, vol. 68, no. 3, pp. 465–479, 2015.

[60] J. Gabela, A. Kealy, M. Hedley, and B. Moran, "Case study of Bayesian RAIM algorithm integrated with Spatial Feature Constraint and Fault Detection and Exclusion algorithms for multi-sensor positioning," *Navigation*, vol. 68, no. 2, pp. 333–351, 2021.

[61] S. Wang, X. Zhan, Y. Zhai, and H. Wang, "Bayesian Upper Bound on GNSS Posterior Integrity Risk," *IEEE Transactions on Aerospace and Electronic Systems*, 2024.

[62] L. Li, R. Li, L. Wang, R. Wang, M. Li, and M. Li, "GNSS integrity risk evaluation in the position domain based on the generalized Pareto distribution," *Measurement Science and Technology*, vol. 34, no. 9, p. 095010, 2023.

[63] J. Liu, B. Cai, D. Lu, and J. Wang, "Integrity of GNSS-based train positioning: From GNSS to sensor integration," in *2017 European Navigation Conference (ENC)*. IEEE, 2017, pp. 48–56.

[64] K. A. B. Ahmad, M. Sahmoudi, and C. Macabiau, "Characterization of GNSS receiver position errors for user integrity monitoring in urban environments," in *ENC-GNSS 2014, European Navigation Conference*, 2014.

[65] H. Jiang, D. Yan, J. Wang, and J. Yin, "Innovation-based Kalman filter fault detection and exclusion method against all-source faults for tightly coupled GNSS/INS/Vision integration," *GPS solutions*, vol. 28, no. 3, p. 108, 2024.

[66] O. G. Crespillo, A. Grosch, J. Skaloud, and M. Meurer, "Innovation vs residual KF based GNSS/INS autonomous integrity monitoring in single fault scenario," in *Proceedings of the 30th International Technical Meeting of the Satellite Division of the Institute of Navigation (ION GNSS+ 2017)*, 2017, pp. 2126–2136.

[67] G. Welch, G. Bishop *et al.*, "An introduction to the Kalman filter," 1995.

[68] T. M. Franke, T. Ho, and C. A. Christie, "The chi-square test: Often used and more often misinterpreted," *American journal of evaluation*, vol. 33, no. 3, pp. 448–458, 2012.

[69] P. Zabalegui, G. De Miguel, J. Mendizabal, and I. Adin, "Innovation-based fault detection and exclusion applied to ultra-wideband augmented urban gnss navigation," *Remote Sensing*, vol. 15, no. 1, p. 99, 2022.

[70] W. Wang, W. Shangguan, J. Liu, and J. Chen, "Enhanced fault detection for GNSS/INS integration using maximum correntropy filter and local outlier factor," *IEEE Transactions on Intelligent Vehicles*, vol. 9, no. 1, pp. 2077–2093, 2023.

[71] H. Zhao and Z. Yang, "A Novel Fault Detection and Exclusion Method for Applying Low-Cost INS/GNSS Integrated Navigation System in Urban Environments," *IEEE Transactions on Intelligent Transportation Systems*, 2024.

[72] R. Sun, J. Wang, Q. Cheng, Y. Mao, and W. Y. Ochieng, "A new IMU-aided multiple GNSS fault detection and exclusion algorithm for integrated navigation in urban environments," *GPS Solutions*, vol. 25, pp. 1–17, 2021.

[73] W. Jiang, D. Liu, B. Cai, C. Rizos, J. Wang, and W. Shangguan, "A fault-tolerant tightly coupled GNSS/INS/OVS integration vehicle navigation system based on an FDP algorithm," *IEEE Transactions on Vehicular Technology*, vol. 68, no. 7, pp. 6365–6378, 2019.

[74] L. Lau and P. Cross, "Development and testing of a new ray-tracing approach to GNSS carrier-phase multipath modelling," *Journal of Geodesy*, vol. 81, no. 11, pp. 713–732, 2007.

[75] A. Bourdeau, M. Sahmoudi, and J. Tourneret, "Tight integration of GNSS and a 3d city model for robust positioning in urban canyons," in *Proceedings of the 25th International Technical Meeting of the Satellite Division of The Institute of Navigation (ION GNSS 2012)*, 2012, pp. 1263–1269.

[76] T. Suzuki and N. Kubo, "GNSS positioning with multipath simulation using 3d surface model in urban canyon," in *Proceedings of the 25th International Technical Meeting of the Satellite Division of The Institute of Navigation (ION GNSS 2012)*, 2012, pp. 438–447.

[77] S. Miura, L.-T. Hsu, F. Chen, and S. Kamijo, "GPS error correction with pseudorange evaluation using three-dimensional maps," *IEEE Transactions on Intelligent Transportation Systems*, vol. 16, no. 6, pp. 3104–3115, 2015.

[78] L.-T. Hsu, Y. Gu, and S. Kamijo, "3d building model-based pedestrian positioning method using GPS/GLONASS/QZSS and its reliability calculation," *GPS solutions*, vol. 20, pp. 413–428, 2016.

[79] G. Zhang, H.-F. Ng, W. Wen, and L.-T. Hsu, "3d mapping database aided GNSS based collaborative positioning using factor graph optimization," *IEEE Transactions on Intelligent Transportation Systems*, vol. 22, no. 10, pp. 6175–6187, 2020.

[80] R. Furukawa, N. Kubo, and A. El-Mowafy, "Prediction of RTK-GNSS performance in urban environments using a 3d model and continuous LoS method," in *Proceedings of the 2020 International Technical Meeting of The Institute of Navigation*, 2020, pp. 763–771.

[81] W. Wen, G. Zhang, and L.-T. Hsu, "Correcting GNSS NLOS by 3d LiDAR and building height," in *Proceedings of the 31st International Technical Meeting of the Satellite Division of The Institute of Navigation (ION GNSS+ 2018)*, 2018, pp. 3156–3168.

[82] X. Bai, W. Wen, and L.-t. Hsu, "Using Sky-pointing fish-eye camera and LiDAR to aid GNSS single-point positioning in urban canyons," *IET Intelligent Transport Systems*, vol. 14, no. 8, pp. 908–914, 2020.

[83] G. He, X. Yuan, Y. Zhuang, and H. Hu, "An integrated GNSS/LiDAR-SLAM pose estimation framework for large-scale map building in partially GNSS-denied environments," *IEEE Transactions on Instrumentation and Measurement*, vol. 70, pp. 1–9, 2020.

[84] L. Chang, X. Niu, T. Liu, J. Tang, and C. Qian, "GNSS/INS/LiDAR-SLAM integrated navigation system based on graph optimization," *Remote Sensing*, vol. 11, no. 9, p. 1009, 2019.

[85] H. Chen, W. Wu, S. Zhang, C. Wu, and R. Zhong, "A GNSS/LiDAR/IMU pose estimation system based on collaborative fusion of factor map and filtering," *Remote Sensing*, vol. 15, no. 3, p. 790, 2023.

[86] X. Meng, H. Wang, and B. Liu, "A robust vehicle localization approach based on gnss/imu/dmi/lidar sensor fusion for autonomous vehicles," *Sensors*, vol. 17, no. 9, p. 2140, 2017.

[87] W. Wu, X. Zhong, D. Wu, B. Chen, X. Zhong, and Q. Liu, "LIO-fusion: Reinforced LiDAR inertial odometry by effective fusion with GNSS/relocalization and wheel odometry," *IEEE Robotics and Automation Letters*, vol. 8, no. 3, pp. 1571–1578, 2023.

[88] J. Zhang, W. Wen, F. Huang, X. Chen, and L.-T. Hsu, "Continuous GNSS-RTK aided by LiDAR/inertial odometry with intelligent GNSS selection in urban canyons," in *Proceedings of the 34th International Technical Meeting of the Satellite Division of The Institute of Navigation (ION GNSS+ 2021)*, 2021, pp. 4198–4207.

[89] L. Li, M. Yang, L. Guo, C. Wang, and B. Wang, "Hierarchical neighborhood based precise localization for intelligent vehicles in urban environments," *IEEE Transactions on Intelligent Vehicles*, vol. 1, no. 3, pp. 220–229, 2016.

[90] S. Li, S. Wang, Y. Zhou, Z. Shen, and X. Li, "Tightly coupled integration of GNSS, INS, and LiDAR for vehicle navigation in urban environments," *IEEE Internet of Things Journal*, vol. 9, no. 24, pp. 24 721–24 735, 2022.

[91] X. Li, H. Wang, S. Li, S. Feng, X. Wang, and J. Liao, "GIL: A tightly coupled GNSS PPP/INS/LiDAR method for precise vehicle navigation," *Satellite navigation*, vol. 2, pp. 1–17, 2021.

[92] W. Wen, T. Pfeifer, X. Bai, and L.-T. Hsu, "Factor graph optimization for GNSS/INS integration: A comparison with the extended Kalman filter," *NAVIGATION: Journal of the Institute of Navigation*, vol. 68, no. 2, pp. 315–331, 2021.

[93] N. Sünderhauf, M. Obst, S. Lange, G. Wanielik, and P. Protzel, "Switchable constraints and incremental smoothing for online mitigation of non-line-of-sight and multipath effects," in *2013 IEEE Intelligent Vehicles Symposium (IV)*. IEEE, 2013, pp. 262–268.

[94] X. He, S. Pan, W. Gao, and X. Lu, "LiDAR-Inertial-GNSS fusion positioning system in urban environment: Local accurate registration and global drift-free," *Remote Sensing*, vol. 14, no. 9, p. 2104, 2022.

[95] J. Beuchert, M. Camurri, and M. Fallon, "Factor graph fusion of raw GNSS sensing with IMU and lidar for precise robot localization without a base station," in *2023 IEEE International Conference on Robotics and Automation (ICRA)*. IEEE, 2023, pp. 8415–8421.

[96] C. Forster, L. Carlone, F. Dellaert, and D. Scaramuzza, "On-manifold preintegration for real-time visual–inertial odometry," *IEEE Transactions on Robotics*, vol. 33, no. 1, pp. 1–21, 2016.

[97] F. Huang, W. Wen, H.-F. Ng, and L.-T. Hsu, "LiDAR aided cycle slip detection for GNSS real-time kinematic positioning in urban environments," in *2022 IEEE 25th International Conference on Intelligent Transportation Systems (ITSC)*. IEEE, 2022, pp. 1572–1578.

[98] J. Lv, J. Xu, K. Hu, Y. Liu, and X. Zuo, "Targetless calibration of lidar-imu system based on continuous-time batch estimation," in *2020 IEEE/RSJ International Conference on Intelligent Robots and Systems (IROS)*. IEEE, 2020, pp. 9968–9975.

[99] A. M. Herrera, H. F. Suhandri, E. Realini, M. Reguzzoni, and M. C. De Lacy, "gogps: open-source MATLAB software," *GPS solutions*, vol. 20, pp. 595–603, 2016.

[100] J. Jiao, Y. Zhu, H. Ye, H. Huang, P. Yun, L. Jiang, L. Wang, and M. Liu, "Greedy-based feature selection for efficient lidar slam," in *2021 IEEE international conference on robotics and automation (ICRA)*. IEEE, 2021, pp. 5222–5228.

[101] J. Zhang, M. Kaess, and S. Singh, "On degeneracy of optimization-based state estimation problems," in *2016 IEEE international conference on robotics and automation (ICRA)*. IEEE, 2016, pp. 809–816.

[102] G. Sibley, L. Matthies, and G. Sukhatme, "Sliding window filter with application to planetary landing," *Journal of field robotics*, vol. 27, no. 5, pp. 587–608, 2010.

[103] M. Quigley, K. Conley, B. Gerkey, J. Faust, T. Foote, J. Leibs, R. Wheeler, A. Y. Ng *et al.*, "ROS: an open-source Robot Operating System," in *ICRA workshop on open source software*, vol. 3, no. 3.2. Kobe, 2009, p. 5.

[104] S. Agarwal, K. Mierle *et al.*, "Ceres solver: Tutorial & reference," *Google Inc*, vol. 2, no. 72, p. 8, 2012.

[105] F. Dellaert, "Factor graphs and GTSAM: A hands-on introduction," *Georgia Institute of Technology, Tech. Rep*, vol. 2, no. 4, 2012.

[106] L.-T. Hsu, F. Huang, H.-F. Ng, G. Zhang, Y. Zhong, X. Bai, and W. Wen, "Hong Kong UrbanNav: An open-source multisensory dataset for benchmarking urban navigation algorithms," *NAVIGATION: Journal of the Institute of Navigation*, vol. 70, no. 4, 2023.

[107] H.-F. Ng and L.-T. Hsu, "3d mapping database-aided GNSS RTK and its assessments in urban canyons," *IEEE Transactions on Aerospace and Electronic Systems*, vol. 57, no. 5, pp. 3150–3166, 2021.

[108] T. Takasu and A. Yasuda, "Development of the low-cost RTK-GPS receiver with an open source program package RTKLIB," in *International symposium on GPS/GNSS*, vol. 1. International Convention Center Jeju Korea Seogwipo-si, Republic of Korea, 2009, pp. 1–6.

[109] P. Xie and M. G. Petovello, "Measuring GNSS multipath distributions in urban canyon environments," *IEEE Transactions on Instrumentation and Measurement*, vol. 64, no. 2, pp. 366–377, 2014.

[110] Hong Kong Lands Department, "Hong Kong 3D Digital Map, note = https://3d.map.gov.hk/."

[111] G. Zhang and L.-t. Hsu, "Performance assessment of GNSS diffraction models in urban areas," *Navigation*, vol. 68, no. 2, pp. 369–389, 2021.